Imaging and Reconstructions Associated with Emission Tomography

by

Cossack Rodrigues

A Thesis Presented in Partial Fulfillment
of the Requirements for the Degree
Master of Science

Approved November 2023 by the
Graduate Supervisory Committee:

Gokul Pathikonda, Chair
Samuel Grauer
Ronald Adrian
Mohamed Kasbaoui
Jeonglae Kim

ARIZONA STATE UNIVERSITY

December 2023

ABSTRACT

Four-Dimensional Emission Tomography (4DET) and Four-Dimensional Absorption Tomography (4DAT) are measurement techniques that utilize multiple 2D images (or projections) acquired via an optical device, such as a camera, to reconstruct scalar and velocity fields of a flow field being studied, using either emission- or absorption-based measurements, respectively. Turbulence is inherently three-dimensional, and thus research in the field benefits from a comprehensive understanding of coherent structures to fully explain the flow physics involved, for example, in the phenomena resulting from a turbulent jet. This thesis looks at the development, application and validity/practicality of emission tomography as an experimental approach to a obtaining a comprehensive understanding of coherent structures in turbulent flows. A pseudo test domain is decided upon, with a varying number of camera objects created to image the region of interest. Rays are then modelled as cylindrical volumes to build the weight matrix. Projection images are generated with Gaussian concentration defined as a spatial function of the domain to build the projection matrix. Finally, concentration within the domain, evaluated via the Least Squares method, is compared against original concentration values. The reconstruction algorithm is validated and checked for accuracy with DNS data of a steady turbulent jet. Reconstruction accuracy and a statistical analysis of the reconstructions are also presented.

ACKNOWLEDGMENTS

I am deeply indebted to my faculty advisor, Professor Gokul Pathikonda, for offering me the opportunity to work on such an exciting (and sometimes frustrating) project that blends the search for experimental diagnostic techniques and their resultant applications in complex turbulence phenomenon. I would not have been able to complete this work without the graciousness shown to me during the entire process. The door to Prof. Pathikonda's office was always open whenever I faced challenges with Matlab or when I had questions about my research. He consistently encouraged new ideas, but gently steered me in the right direction when he thought I needed it.

Special thanks go to Professor Samuel Grauer who generously provided brilliant ideas, expertise and time towards this thesis. In the same breath, I would also like to thank him and his team at Pennsylvania State University for providing the Imaging Models and programming Tools to support my work.

I am also grateful to Professors Ronald Adrian, Mohamed Kasbaoui and Jeonglae Kim, for agreeing to be on my defense committee.

I am especially grateful to the administrative staff at ASU and SEMTE, particularly Erika Parra, for timely and patient assistance throughout the program.

I could not have successfully completed my degree without the friendship and help I received from my peers at ASU and the CMAT lab. I am especially thankful to Sushant for providing me with DNS data and lending his expertise with Matlab.

To my parents and siblings, thanks for all the encouragement and support throughout this phase of my life.

TABLE OF CONTENTS

CHAPTER Page

LIST OF TABLES

LIST OF FIGURES

Figure Page

Figure Page

Chapter 1

INTRODUCTION

Turbulence and associated phenomena are an integral part of life on earth. Turbulent flows, specifically, occur in our everyday surroundings, ranging from smoke from a chimney, water flowing down a waterfall, all across the physical scale, down to fuel injected in combustion chambers. Even though turbulent flows can be chaotic and difficult to predict, it is of practical interest to understand the flow physics involved in great detail. The flow fields exhibit nonlinear, multi-scale behavior that is inherently three dimensional in nature. For this reason, volumetric measurements that have significant spatio-temporal resolution are needed to study turbulent phenomena and develop algorithms to be used in the design and control of engineering devices [7].

To illustrate the chaotic nature of turbulent flows, figure 1.1 depicts planar images of a turbulent jet at two different Reynolds numbers. The image, representing the concentration distribution in a plane illuminated by a laser, highlights the variation and irregularity of the same. The full turbulent velocity and concentration field is in three dimensions, and the fluid's velocity and concentration fields vary significantly and irregularly in position and time [11]. An ability to capture such concentration field in three dimensions, with sufficient spatio-temporal resolution, significantly expands our capability to capture the complex turbulent mixing processes at play within the turbulent jet. We aim to develop and characterize the volumetric imaging approaches that use various tomographic reconstruction algorithms.

Volumetric Imaging is a non-invasive technique that measures a three-dimensional (3D) field using multiple, independent two-dimensional (2D) images acquired via an optical

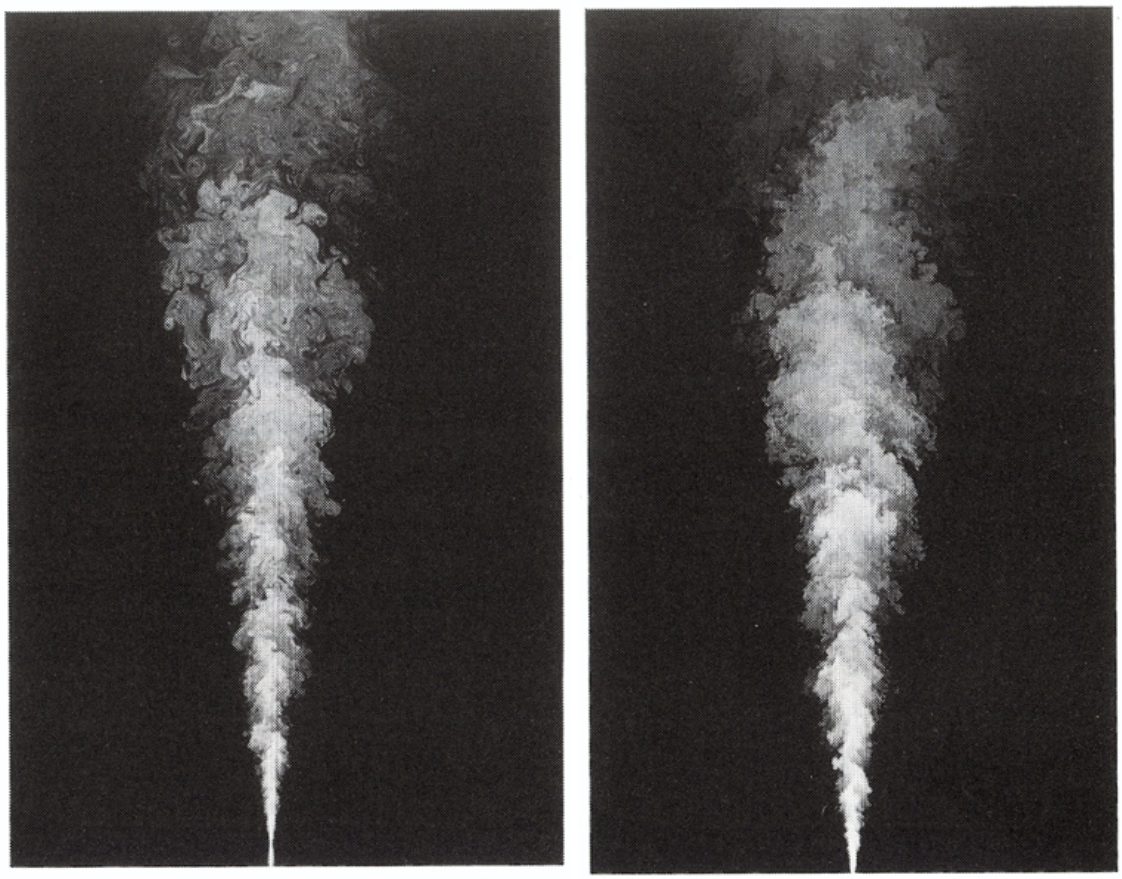

(a) Re = 5,000 (b) Re = 20,000

Figure 1.1: Planar Images of Concentration in a Turbulent Jet [11]

device, usually a camera. These 2D images, also called projections, are combined with a tomographic reconstruction algorithm, based on a mathematical inversion of a measurement model that approximates the 2D imaging process, and ultimately produces a 3D reconstruction of the measured volume.

Tomography has its origins in the medical industry as a diagnostic tool, arising from significant developments in the 1970s and 1980s [7, 15]. Since then, this approach has been refined and applied in a significant number of technological and engineering research pursuits. Specifically, we focus on using these tools for emission and absorption imaging.

1.1 Overview

Tomography is based on the inversion of a forward "measurement model" that converts a 3D domain into 2D projections of that domain. The project aims to develop, test and validate an imaging and inversion tool that supports the reconstruction of pseudo scalar (concentration) and velocity fields using emission and absorption based measurements. The approach is based on Emission Tomography (ET) and Absorption Tomography (AT), wherein light emission or attenuation measurements, respectively, recorded by multiple cameras, each facing either the target phenomenon that emits photons due to chemiluminescence, fluorescence or similar emissive phenomenon, or, in the case of absorption, a monochromatic backlight panel positioned behind the phenomemon of interest (i.e a turbulent jet), can be combined to reproduce a concentration field.

The projection (from emission and/or absorption) images acquired, from multiple camera perspectives, are Line-of-Sight (LoS) integrated. Whilst they provide qualitative information, it is difficult to determine local scalar structures. Ultimately aiming to evaluate the evolution of coherent 3D structures, this approach leverages optical signals from multiple camera perspectives combined with a tomography algorithm to reconstruct the Quantity (or Quantities) of Interest (QoI). Figure 1.2 presents an optical experimental layout used to acquire data in the case of absorption tomography. Multiple cameras are positioned around an optically accessible tank and are focused on their respective diffuser panel. From the array of Light Emitting Diodes (LEDs) placed behind the tank screens (outside the tank), an optical signal is recorded prior to the introduction of the flow (to acquire reference data). Once the flow enters the tank, light is absorbed by a tracer dye, and absorbance data is calculated from the reference and attenuated images.

Reconstruction is achieved by inverting an ill-posed system of equations built using projection data from multiple cameras, the weight of each projection and absorbance coefficients.

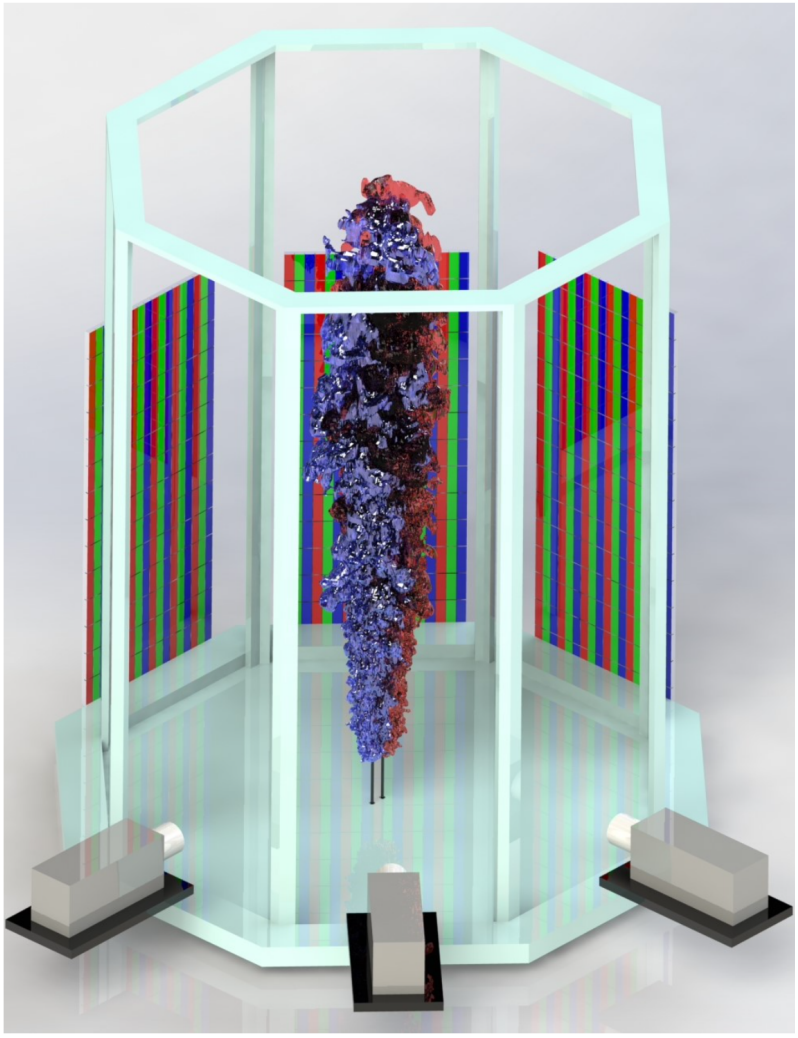

Figure 1.2: Layout of the 4DAT Apparatus

1.2 Goals

The current body of publicly available literature has Emission tomography covered in extensive detail, with numerous tool already developed to refine this approach. On the other hand, literature on absorption tomography is limited. We seek to apply these ideas and tools on absorption imaging and, eventually, absorption tomography.

The primary aim of the work presented in this thesis is to develop a tool that can reliably

reconstruct scalar concentration fields to an acceptable level of accuracy via the following objectives:

1. Setup a domain object and multiple camera objects that align with a suitable phantom experimental setup, similar to that presented in figure 1.2.
2. Test the domain and camera objects, imaging models and reconstruction algorithm with robust yet simple geometry.
3. Evaluate the quality of reconstructions using complex phantom geometry.
4. Validate the practicality and evaluate the limitations of the tool by testing with DNS turbulent flow data.

The primary goal is to reconstruct the spread of line-integrated emission/absorption coefficients from a set of projections / light intensity measurements from different camera perspectives.

In the current thesis, section 1 presents an introduction to the concept of Tomography, followed by the motivation and objectives for this thesis, along with some background on the physics of imaging models, imaging tools and reconstruction algorithms. This is followed by sections 2 and 3 which cover results obtained from a simple and complex 'toy' torus environment, respectively, followed by a validation study using DNS data of a steady turbulent jet presented in section 4. Finally, section 5 summarizes conclusions from, and future work pertaining to, this thesis.

1.3 Background, Imaging Tools and Setup

The origins of the word 'Tomography' lie in ancient Greek. It is derived from the ancient Greek word τόμος (tomos) meaning 'slice' or 'section', and γράφω (graphō) meaning 'to draw', or adapted to scientific applications, 'to describe'. Tomographic Imaging, with its

primary development and use in medical applications, has a large body of literature on medically-relevant imaging algorithms as well as guidelines for using tomography as a diagnostic tool [12]. Outside of the medical field, this method is also utilized in atmospheric sciences, oceanography and material sciences, as it is a powerful non-intrusive diagnostic approach to spatially resolve scalar fields in turbulent flows [14].

Turbulent flows, despite their chaotic nature and challenging predictability, still attract research interest to understand flow features in greater detail. Turbulence being an extremely effective transportation and mixing vehicle, renders its use in many engineering applications.

Consider the example of a supersonic inlet. If one wishes to study the mixing of the fuel and air mixture, one approach to evaluate the flow field is to insert physical probes in the center of the flow field. This technique introduces disturbances to the flow field, and results obtained from tests may not necessarily be representative. Tomographic imaging permits a non-invasive data acquisition approach that can visualize the inside of this phenomena of interest without intruding the flow field.

This non-invasive diagnostic approach works well with laser and light sources, as photons emitted or absorbed, have the potential to provide significantly greater spatial and temporal resolution than physical probing. An added benefit of volumetric imaging is the lack of disturbance to the flow field, and immunity to errors originating from physical and chemical reactions that may occur [3].

The fundamental equation for Tomographic Reconstructions is based on the linear equation $\boldsymbol{Ag} = \boldsymbol{p}$, matrices $\boldsymbol{A}$ and $\boldsymbol{p}$, and the unknown quantity, $\boldsymbol{g} = \boldsymbol{A}^{-1}\boldsymbol{p}$. Here $\boldsymbol{g}$ is the unknown field, $\boldsymbol{p}$ is a vector with the projections of the unknown field, measured as the emission or the absorption signals using an imaging device, and $\boldsymbol{A}$ is the weight matrix that linearly maps the field to the projections via the domain and imaging setups, that are elaborated on in the following sections.

One of the first steps in setting up the reconstruction environment is to select an appropriate Imaging Model, a domain representative of the field of interest, and a practical number of cameras. Section 1.3.1 covers some literature on Imaging Models, highlighting some detail about the models used, followed by section 1.3.4 on regularization concepts, specifically Tikhonov regularization. Finally, a brief overview on 3D masking and its advantages are presented.

1.3.1 Imaging Models

Both Emission and Absorption Tomography approaches require a forward model of the image formation process to develop projection data. This model is then inverted to present characteristics of the flow field (i.e. scalar concentration and velocity fields, in this case). The selection of Imaging Models is particularly important as it determines the shape of rays and their relative trajectory through the measurement domain.

For the current work, we use the 'Algebraic Reconstruction Algorithms' developed by Grauer et al. presented in [7], wherein the weight matrix, $\boldsymbol{A}$, can be constructed to accurately approximate a wide range of imaging devices. As presented earlier, the matrix product $\boldsymbol{Ag} = \boldsymbol{p}$ is used to represent emission, absorption, or even the refraction of light in the domain of the flow field, in terms of a basis used to represent the phenomenon being studied. This representation accounts for the path traversed by, and the shape of, each ray.

In this context, the two main approaches to building $\mathbf{A}$ are outlined below:

1. Directly modelling the ray (or bundle of rays) accepted by a pixel and calculating the interaction of said rays with the basis.
2. Tracing light emitted within the reconstruction volume to the cameras. [7]

Approach 1 is referred to as ray-(or pixel-)centric, whilst approach 2 is voxel-centric. All the

work presented in this thesis utilizes the ray-centric approach. Figure 1.3 presents a simple schematic of three ray-centric models wherein rays can be assumed to be either 1D lines (thus 'Thin rays'), or 3D cylindrical volumes ('Cylindrical rays') or 3D conical volumes ('Conical Rays').

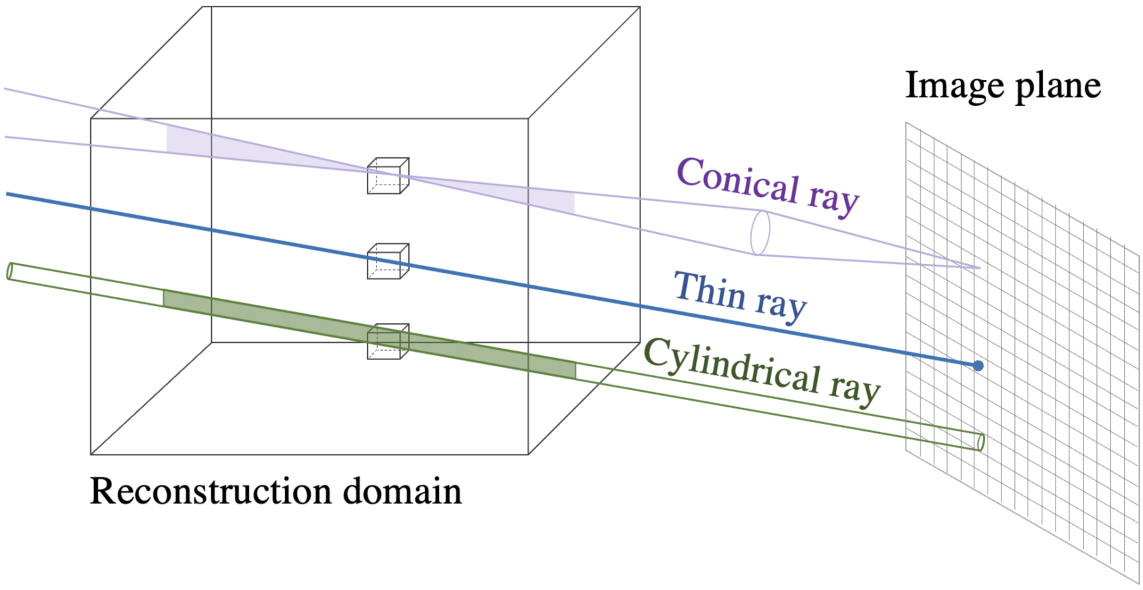

Figure 1.3: Illustration of Thin Ray, Cylindrical Ray and Conical Ray Models with a Voxel Basis (taken from [7])

1.3.1.1 Ray Centric Models

All work presented in this thesis is solely based on the use of cylindrical ray tracing as the imaging model, algorithms and tools for which have been developed and provided by the Grauer Lab at Pennsylvania State University and have been comprehensively covered in [7]. A brief discussion on cylindrical ray tracing is stated below.

$\boldsymbol{A}$ is the weight matrix that linearly maps the 3D field to the projections via a forward measurement model. Imaging models to build these projections consider rays of light as either 1D lines or 3D volumes. For both dimensional approaches, elements of the weight

matrix represent the intersection (or volume fraction) of a ray with one basis function, i.e. a voxel, in this case. Each element describes the contribution of the jth solution component to the ith projection, $\boldsymbol{p}_i$, or to be more specific, in this case, the contribution of the jth voxel to the ith pixel, $\boldsymbol{p}_i$. Essentially, the weight matrix describes the contribution of each voxel in the domain to each ray of light traversing through the domain.

As individual rays of light only traverse a small number of voxels (typically on the order of $n^{1/3}$ in a cubic domain [7]), the weight matrix is a sparse matrix. Non-zero elements are identified by establishing a minimum distance between each ray and voxel center via equation 1.1, where the camera position is $\boldsymbol{c}$ and voxel center is $\boldsymbol{v}$, with a ray traveling along a unit vector $\hat{\boldsymbol{r}}$ between the camera and voxel. With an appropriate threshold for cut-off distance selected, only ray-voxel pairs satisfying this condition are evaluated.

$$d_{min} = \sqrt{||\boldsymbol{v} - \boldsymbol{c}||_2^2 - [(\boldsymbol{v} - \boldsymbol{c})^T \hat{\boldsymbol{r}}]^2} \tag{1.1}$$

In thin ray tracing, the ray sum intensity signal received by a pixel is modeled using a ray simplified as a 1D line. As a result, $\boldsymbol{A}_{i,j}$ is essentially the chord length of the ith Line-of-Sight (LoS) or ray within the jth voxel. Ray-voxel intersections can be quickly computed using a ray-box algorithm presented in [17]. If d_{min} exceeds $3^{1/3} l_{vox}$, where l_{vox} is the length of a voxel, Grauer et al. state in [7] that respective elements in $\boldsymbol{A}_{i,j}$ can be estimated to be zero.

This model can be simplified further by considering voxels as spheres (instead of cubes) and calculating ray-sphere intersections for elements of $\boldsymbol{A}$, as spheres are one of the simplest objects to ray trace [9].

Thin rays work well when the voxels in the domain are large. This, however, introduces significant discretization errors in the solution, ultimately rendering poor reconstructions. Additionally, the thin ray approach fails with very small voxels, as this voxel can now lie

between two thin rays reaching adjacent pixels. In this case, a non-physical (artificial) signal is emitted, absorbed or scattered [7].

In reality, pixels on a camera sensor represent an area, not a point. Thus, light rays bundled as a volume rather than a line, are incident on pixels. To address this, light rays are modelled as cylindrical volumes with a finite cross section (thin rays also have a finite cross section, albeit very close to zero). Cylindrical rays are applicable in an environment when the region of interest is contained within the camera's depth of field, as this is where the assumption of a constant cross section is valid [7].

To address the problem associated with thin rays and large voxels, the radius of the cylindrical volume employed in this approach is sized to maintain the pixel area, thus, $r_{pix} = l_{pix}/\pi^{1/2}$, where l_{pix} is the side length of a square pixel. Similar to thin ray tracing, non-zero elements of the sensitivity matrix are evaluated with the following equation determining which voxels contribute to the ray-sum intensity measurement.

$$d_{min} \leq r_{pix} + 3^{1/2} l_{vox} \tag{1.2}$$

where, d_{min} is determined with equation 1.1 and $3^{1/2} l_{vox}$ represents the distance from the centroid to the corner of a voxel. This is equivalent to the thin ray collision test when $r_{pix} = 0$ [7], and the intersection volume determines the elements of the weight matrix.

This intersection volume is estimated by a Monte Carlo simulation. Using the Monte Carlo simulation, a set of random points that lie inside a voxel are generated. A subset of these points that lie within the cylinder is identified using a modified form of equation 1.1 wherein d_{min} is calculated using these random points, as opposed to the voxel center. Points that lie in the intersection volume, by definition, must satisfy $d_{min} \leq r_{pix}$. The resulting product of the subset of points that lie inside the cylinder and the voxel volume (l_{vox}^3) build elements of $\boldsymbol{A}_{i,j}$.

Whilst cylindrical rays have a constant cross section, in reality, a bundle of rays reaching a pixel will not have a uniform cross section. A thin lens focuses rays from an object plane (not rays from a volume) onto an image plane (camera sensor), with objects on either side of this plane being out of focus. Additionally, rays fall on a pixel of finite area through an aperture that permits light from multiple angles and distances, and consequentially, a singular lens cannot perfectly focus all these rays of light in one plane. This produces a region called the camera's Depth of Field, within which effects of blur are nominal.

The concepts of conical rays address the shortcomings mentioned above. Starving a camera of light by moving away from the target and closing the aperture by as much as possible to ensure light rays are in focus, is not ideal. Short exposure times are indispensable in rapidly changing flow fields to prevent blurry captured images. Conical rays account for these non-ideal effects associated with a large measurement domain, large aperture, small working distance to the target phenomenon, or any such combination [7].

1.3.2 Imaging Tools

Camera objects are built on the model of a pinhole camera using internal 'intrinsic' parameters such as the camera's focal length, f, the optical center and the skew coefficient (which accounts for tilt), and external 'extrinsic' parameters that describe the camera's pose (location and orientation). Matrix 1.3 presents the intrinsic matrix, where f_x and f_y describe the focal length, s is the skew coefficient (0 for square pixels and non-zero if image axes are not perpendicular), and, c_x and c_y describe the optical centers. The extrinsic parameters consist of a 3 X 3 rotation matrix, $\boldsymbol{R}$, and a translation vector, $\boldsymbol{t} = -\boldsymbol{Rc}$, where $\boldsymbol{c}$ is the position of the pinhole in global coordinates.

$$\boldsymbol{K} = \begin{bmatrix} f_x & s & c_x \\ 0 & f_y & c_y \\ 0 & 0 & 1 \end{bmatrix} \tag{1.3}$$

Camera objects are defined in MATLAB via imaging models discussed in section 1.3.1 [7] and imaging tools provided by the Grauer Lab at Pennsylvania State University.

1.3.3 Projections

Consider a 3D region of interest as presented in figure 1.4, which depicts the distribution of the scalar QoI, $\boldsymbol{g}$ (concentration). In the case of emission, each imaging device records a 2D image of the light generated and transmitted through the domain. Alternatively, for absorption, 2D images of absorbed and transmitted light are recorded. These images (projections) are stored as discrete sensor units (or pixels). With the imaging model prescribing the weight of each voxel with respect to each pixel, the reconstruction can be produced by inverting the product of the measured projections and inverted weight matrix.

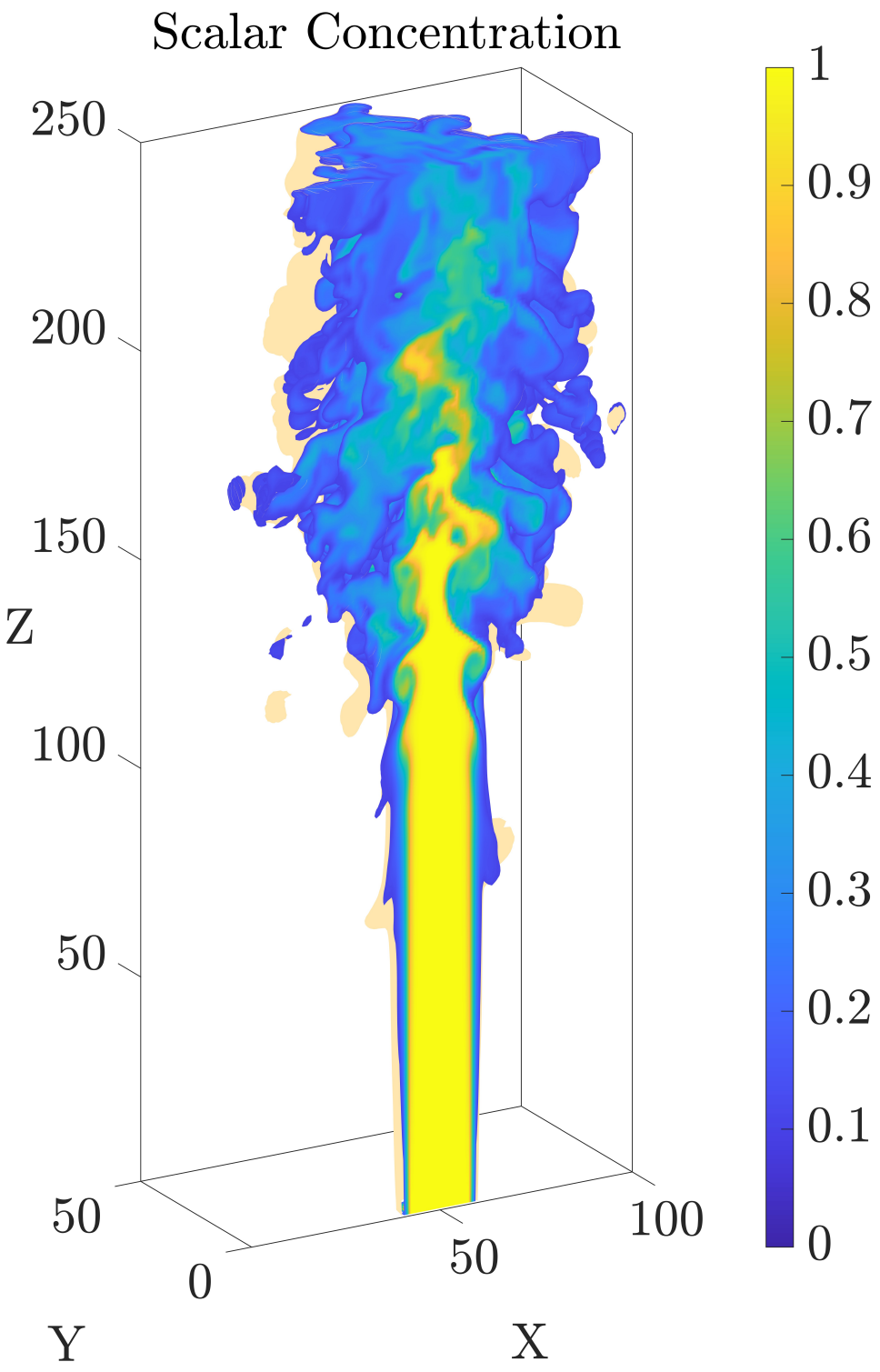

Figure 1.4: 3D Cutaway of a Steady Turbulent Jet

Projections for this thesis are built using the forward measurement model discussed in 1.3.1 and synthetic Gaussian concentration. Once the weight matrix is generated via cylindrical ray tracing, individual elements are multiplied with corresponding elements of spatially resolved Gaussian concentration described in the domain. These projection images serve as the base from which linear and regularized inversions are evaluated.

1.3.4 Regularization

The linear system of equations built using the weight matrix $\boldsymbol{A}$, unknown concentration $\boldsymbol{g}$ and projections $\boldsymbol{p}$, are solved using the Least Squares function built in to MATLAB.

Volumetric reconstruction, however, is an inherently ill-posed inverse problem due to the contributions of noise and errors in the model [7]. A problem is considered ill-posed, if it does not satisfy the requirements of a well-posed problem, namely:

1. **Existence**: there exists a solution
2. **Uniqueness**: the solution is unique, and
3. **Stability**: the solution depends continuously on perturbations to data.

Due to restricted projection angles, the weight matrix is rank-deficient (and inherently ill-posed). This is addressed with regularization wherein the rank-deficient matrix equation is augmented by another set of equations, $\lambda \boldsymbol{L}_{i,j} = 0$. The augmentation aims to promote desirable characteristics whilst simultaneously penalizing undesirable characteristics. $\boldsymbol{L}_{i,j}$ is the discrete gradient matrix used to enforce a smoothing condition:

$$L_{i,j} = \begin{cases} 1, & \text{if } i = j \\ -1/n_i, & \text{if voxel } i \text{ neighbors voxel } j \\ 0, & \text{otherwise} \end{cases} \tag{1.4}$$

where n_i is the number of neighboring voxels. In 3D regularization, n_i = 6, as each voxel is surrounded by 6 neighboring voxels (a neighboring voxel is considered a neighbor if it shares a face with the main voxel). λ is the regularization parameter that controls the influence of the penalty term compared to the residual norm.

1.3.4.1 Tikhonov Regularization

In regularization techniques, the measurement equations are augmented with a penalty function that is designed to promote desirable characteristics in the flow phenomenon, whilst simultaneously penalizing undesirable characteristics. This is achieved by introducing physically-motivated information in the system of equations. The most common form of classical regularization in Volumetric Imaging is Tikhonov regularization which prescribes smooth solutions. Total Variation (TV) is another form that similarly prefers smooth solutions but can also accommodate sharp discontinuities [7].

$$\boldsymbol{g}_{Tik} = \arg\min\left(\begin{bmatrix} \boldsymbol{A}_{i,j} \\ \lambda \boldsymbol{L}_{i,j} \end{bmatrix} \boldsymbol{g} - \begin{bmatrix} \boldsymbol{p} \\ \boldsymbol{0} \end{bmatrix}\right) \tag{1.5}$$

1.3.5 Masking

In Emission and Absorption tomography, the domain is often significantly larger than the volume occupied by the phenomenon of interest, causing an unnecessary demand on computational resources. Additionally, the greater volume contributes to the under-determined linear system of reconstruction equations. Thus, it is helpful to define a 'mask' that ignores unwanted voxels that do not significantly contribute to the flow field, thus producing a tighter reconstruction volume.

With a threshold value established to account for noise in the flow field or insignificant intensity signal, elements of the projection matrix that fall below this threshold, along with

corresponding voxels, are dropped from their respective matrices. The refreshed projection vector and weight matrix are then inverted to produce the concentration field associated with pixels and voxels that have not been dropped after masking. The remaining undetermined elements of the concentration field matrix are then populated with zeros.

Chapter 2

SIMPLE TORUS

This chapter presents the domain and camera setups, projection images and, linear and regularized inversions of concentration defined by simple torus geometry.

2.1 Domain Setup

Work on producing reconstructions started off with the creation of Gaussian concentration in a domain following the shape of an inclined torus as presented in figure 2.1.

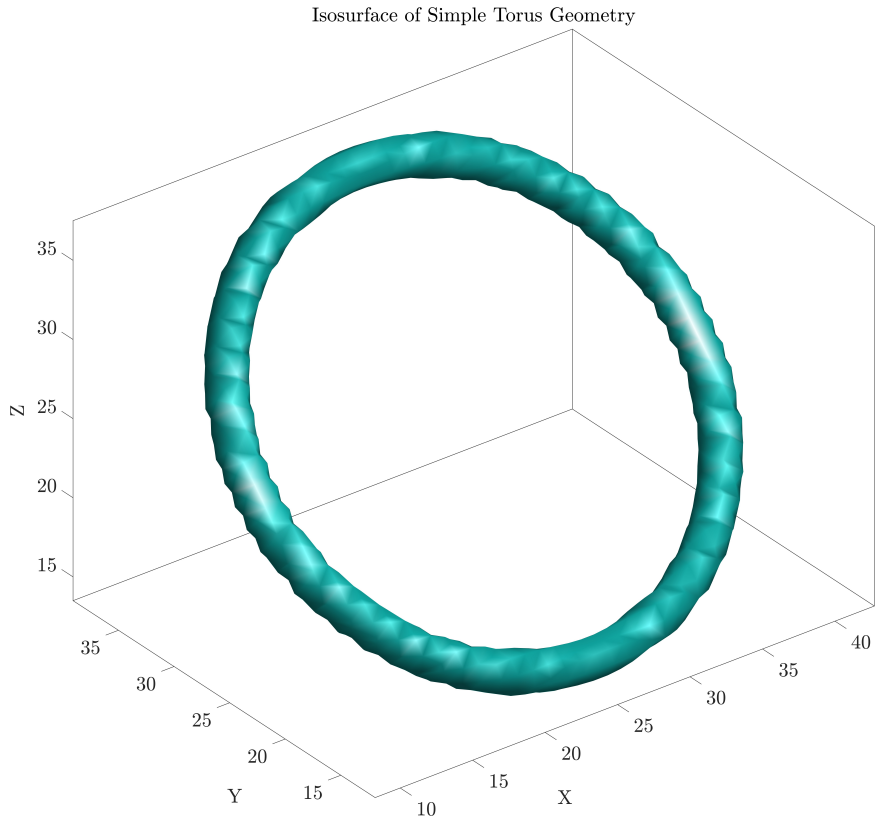

Figure 2.1: Isocontour of Gaussian Concentration along a Torus

The domain for the simple torus defined concentration is initialized as a cube of dimensions

1 unit x 1 unit x 1 unit. The domain is setup with 50 voxels per unit length, with the total voxel count equalling 125,000 voxels.

Gaussian concentration along the tube of the torus is modelled with equation 2.1, where x and y are coordinates along the circumference associated with the primary radius, and σ is the magnitude of the secondary (tube) radius.

$$g = \exp\left(\frac{-0.5 \times \left(x^2 + y^2\right)}{\sigma^2}\right) \tag{2.1}$$

2.2 Camera Setup

For the simple geometry torus, 3 cameras are used to image the concentration field. The cameras are radially placed in the $x - y$ plane of the domain with a camera arc radius of 2.5 times that of the biggest domain dimension, and placed halfway along the z axis (placement is similar to figure 1.2). The cameras all have a focal length of 40mm and sensor size of 500 x 500 pixels. All cameras have their sensors facing the center of the domain.

2.3 Projection Images

This section presents projection images used to build the equation matrices.

Projection images were built using equation 2.2, where $\boldsymbol{A}_{i,j}$ is the weight matrix constructed using the cylindrical ray tracing model, and $\boldsymbol{g}_j$ is scalar concentration of voxel j, defined by Gaussian concentration modelled with equation 2.1. The product of these (volume fraction of ray through each voxel (weight) multiplied with the concentration in this voxel), ultimately produces a ray-sum intensity signal corresponding to pixel i. Thus, the projection image matrix is assembled by combining the ray-sum intensity signals for all pixels on the camera sensor.

$$\boldsymbol{p}_i \approx \sum_{i=1}^{n} \boldsymbol{A}_{i,j} \boldsymbol{p}_j \tag{2.2}$$

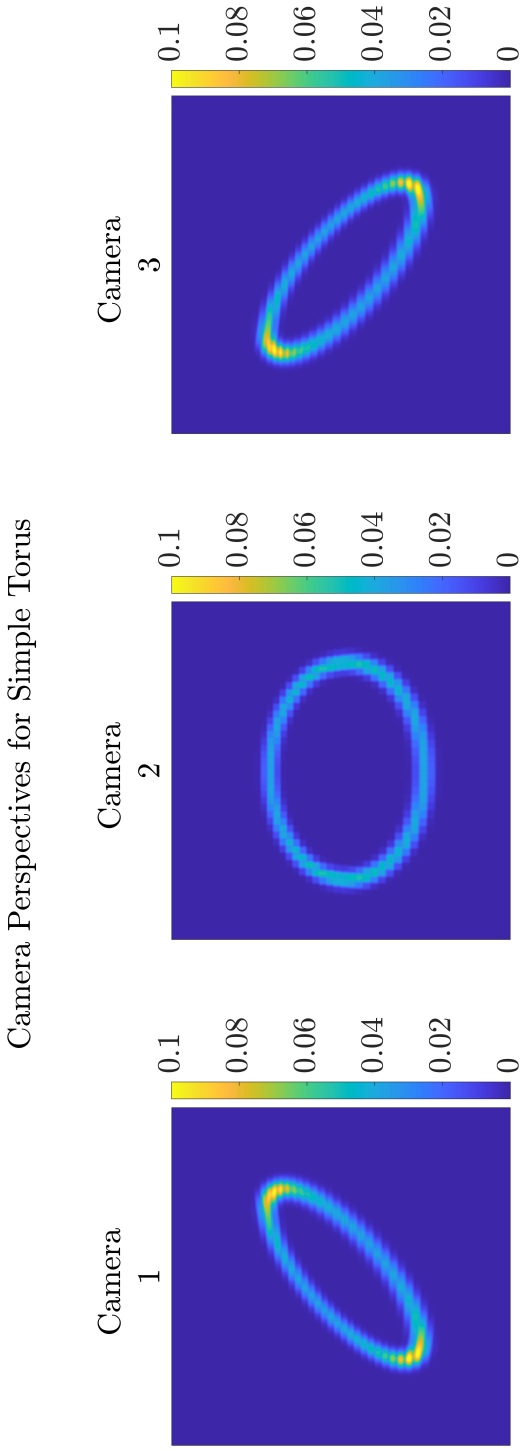

Figure 2.2: Camera Perspectives (500 X 500) for Gaussian Concentration Defined by a Simple Torus

2.4 Linear Inversion Results

The linear inversion approach utilizes the Least Squares method to evaluate unknown values of concentration, g.

Figure 2.3 presents XY slices of the 3D scalar field at 30% and 50% of the Z axis, and figure 2.4 presents XZ slices of the 3D scalar field at 50% and 80% of the Y axis. Visually, it is evident that linear inversions, in this case, produce excellent reconstructions of a simple concentration field. The XY slice at 30% Z_{max} in figure 2.3a and XZ slice at 80% Y_{max} in figure 2.4b depict clearly defined regions of concentration. Judging by the difference between ground truth and the linear reconstruction, the reconstructions are very accurate, and the inversion results in the unique field corresponding to the ground truth. This is because of relatively simple spatial information, and the number of projections and resolution are sufficient to accurately reconstruct the ground truth, as opposed to fields with larger spatial bandwidth. Additional regularization, in this case, is not required. Nonetheless, section 2.5 presents results from a regularized inversion.

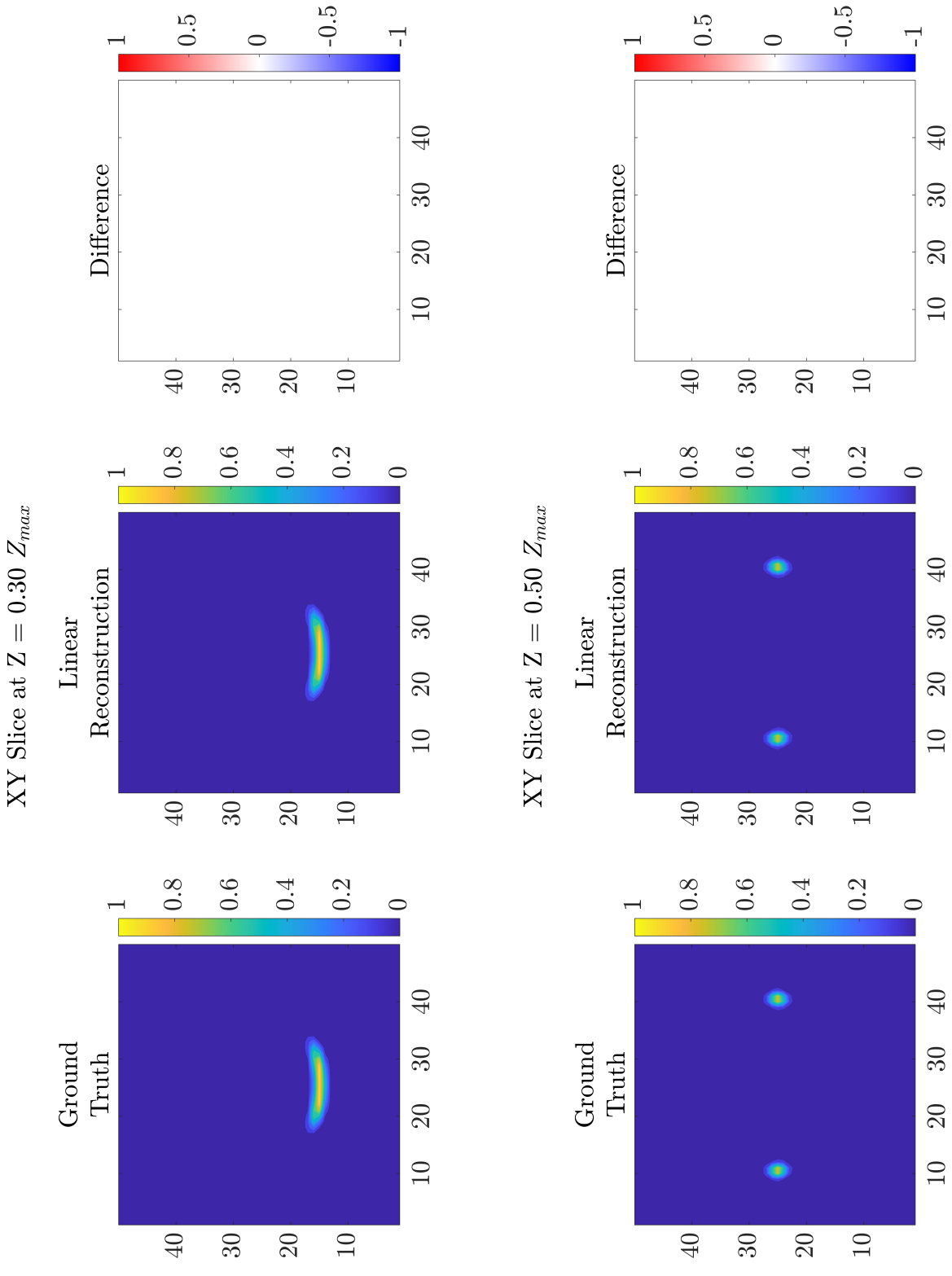

(a) XY Slice at Z = 0.3 × Z_{max}

(b) XY Slice at Z = 0.5 × Z_{max}

Figure 2.3: XY Slices of Linear Reconstructions

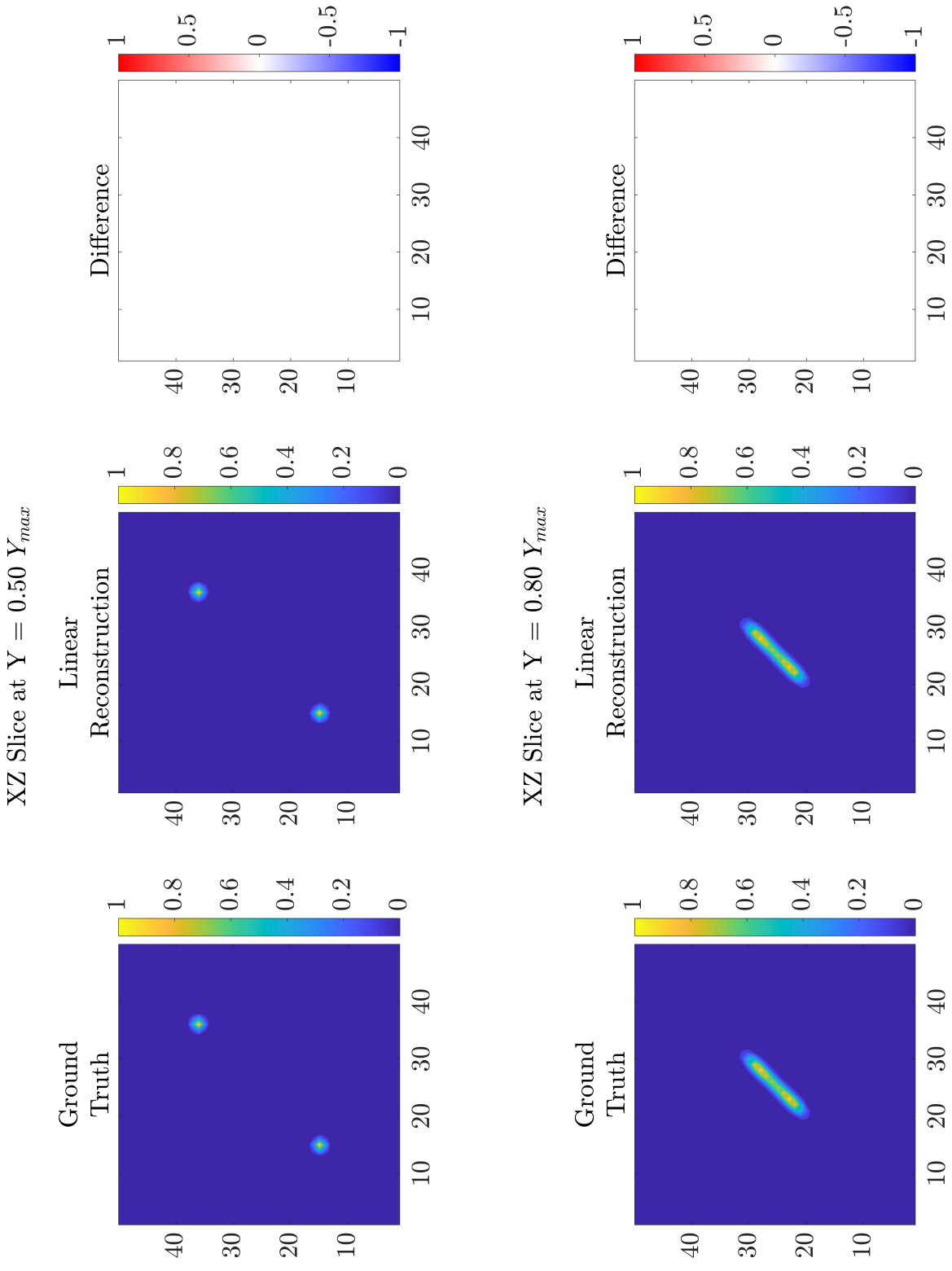

(a) XY Slice at Z = 0.5 × Z_{max}

(b) XY Slice at Z = 0.8 × Z_{max}

Figure 2.4: XZ Slices of Linear Reconstructions

2.5 Regularized Inversion Results

The slices through the regularized reconstructions presented in figures 2.5 and 2.6 highlight qualitatively excellent reconstructions. In the slice where $\lambda = 1e - 01$, the regularization parameter causes the reconstruction to be over-smoothed. Thus it is difficult to recognise the varying levels of concentration in the field.

A key benefit of regularization is achieving convergence of the solution much quicker than attempting to solve the set of equations via a linear inversion. For the simple torus, regularized inversion took around a fifth of the time as that of a linear inversion.

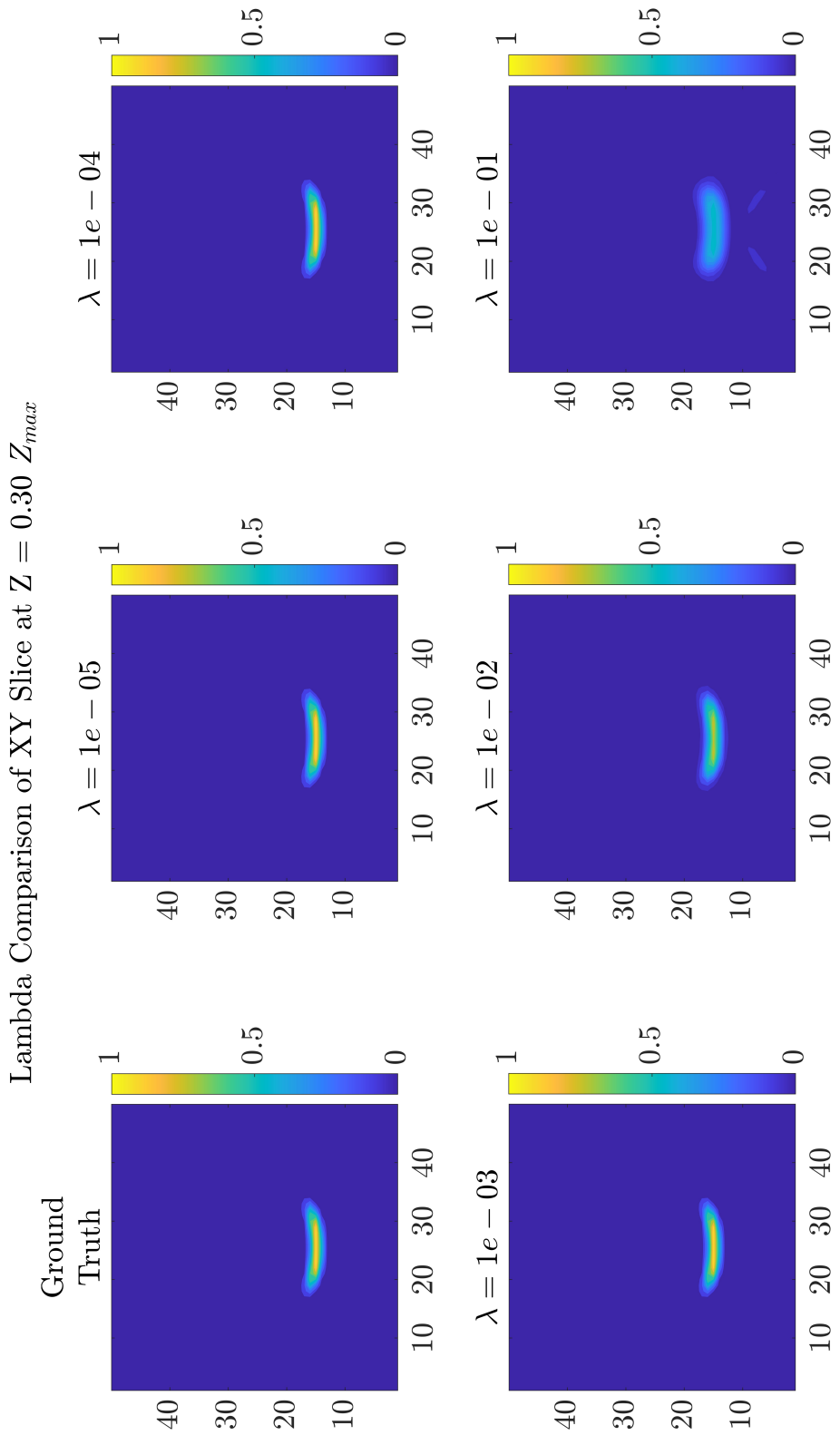

Figure 2.5: XY Slices of Regularized Reconstructions

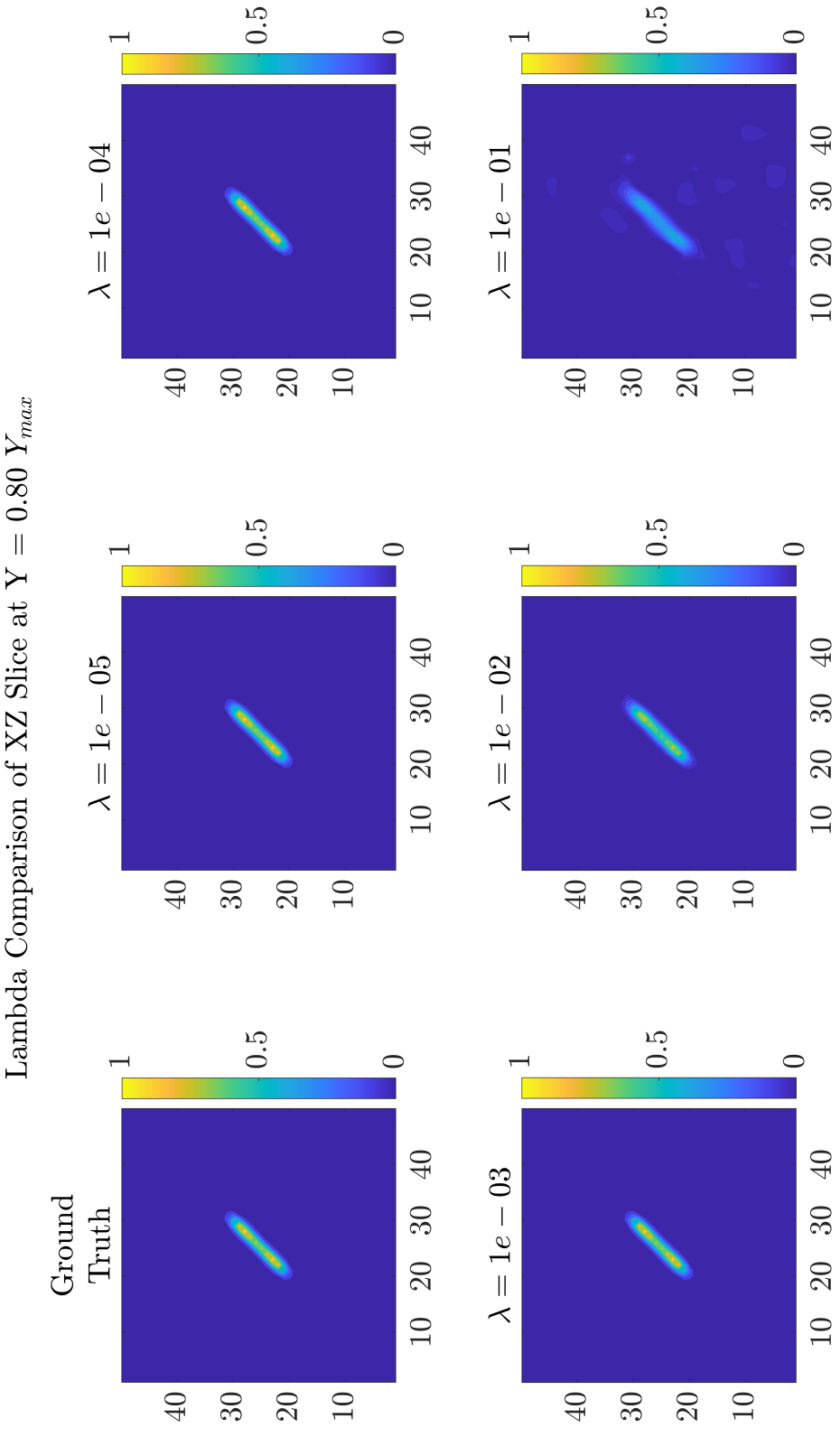

Figure 2.6: XZ Slices of Regularized Reconstructions

In summary, Gaussian concentration as a function of the secondary radius of a torus was mathematically introduced to a cubic domain. Three cameras placed in a circular arc in the XY plane outside the domain imaged the concentration field and produced projections. A weight matrix was constructed assuming cylindrical rays traversing through the domain to the three camera sensors. With this, concentration of the scalar field, p, was calculated using the Least Squares method to produce a linear inversion. Additionally, a Tikhonov regularized inversion was also performed using a regularization parameter sweep ranging from $\lambda = 10^{-6}$ to $\lambda = 10^{2}$.

The linear inversions appear to produce excellent reconstructions, with accuracy at 100% based on the qualitative slices presented, showcasing remarkably well defined concentration levels. Except for very high values of the regularization parameter, λ, the regularized results display excellent reconstructions similar to those of the linear inversion. An important advantage with regularization, in this case, is the significant reduction in the use of computational resources and the time required to obtain reconstructions of the 3D field.

Chapter 3

COMPLEX TORUS

With the target of understanding the resolution limitations of the reconstruction algorithms, concentration defined by complex torus geometry was decided upon, aiming to reproduce the dense spatial information typically described by a turbulent flow field. With this objective in mind, this chapter presents the domain and camera setups, projection images, and, linear and regularized inversions of concentration defined by complex torus geometry.

3.1 Domain Setup

Similar to the domain for a simple torus, the domain for the complex torus defined concentration is initialized as a cube of dimensions 1m x 1m x 1m. The domain for one instance of the complex torus is setup with 100 voxels per unit length with the total voxel count equaling 1,000,000 voxels. In these cases, the voxel density is chosen specifically to be atleast 1.33 times that of the total number of pixels to produce an under-determined system of equations via increased spatial information. Table 3.1 details the domain and camera parameters used for the complex torus geometry with varying camera sensor size and voxel density.

Table 3.1: Domain and Camera Parameters for the Complex Torus Geometry

	Voxel Density	Voxels	Cameras	Camera Sensor (pixels)	Total Pixels	$\frac{\text{Voxels}}{\text{Pixels}}$
Run 1	100	1,000,000	3	500 X 500	750,000	1.33
Run 2	55	166,375	3	200 X 200	120,000	1.38
Run 3	35	42,875	3	100 X 100	30,000	1.43

Gaussian concentration along the tube of the torus for all complex geometries (CG1, CG2 & CG3) is modeled via equation. 3.1 with respective geometries displayed in figure 3.1:

$$g = \exp\left(\frac{-0.5 \times (x-b)^2}{(offset + pc_{val} \times \sin(n \times \theta))^2}\right) \tag{3.1}$$

Where,

$offset$ ≡ offset used to account for the negative values of sine

pc_{val} ≡ percentage value used to limit sine values

n ≡ number of ridges/humps across the entire torus

θ ≡ azimuthal angle along the primary radius of the torus

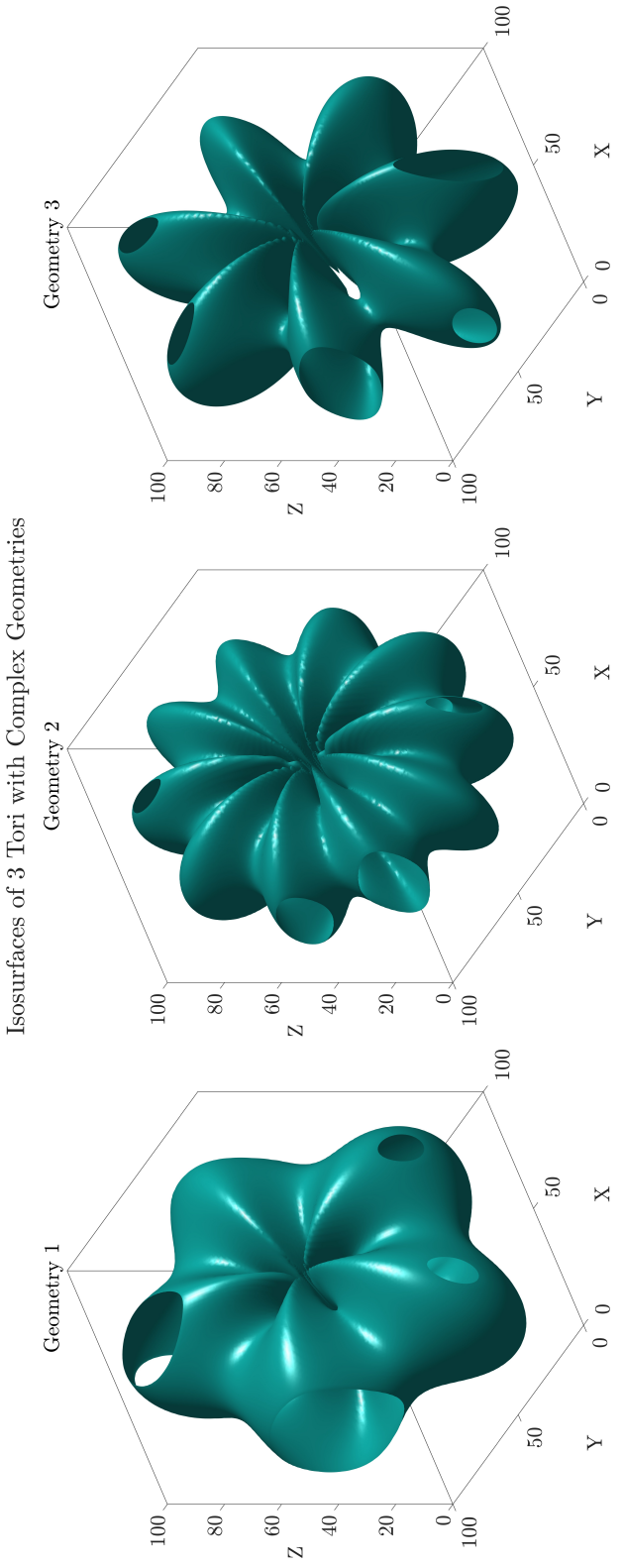

Figure 3.1: Geometry of the 3 Tori with Complex Geometries

3.2 Camera Setup

For the simple and complex geometry tori, 3 cameras are used to image the concentration field. Some of the contributing parameters are presented in Table 3.2.

Table 3.2: Camera Parameters for the Complex Torus Geometry

	Camera Sensor (pixels)	Focal Length (mm)	Pixels
Run 1	500 X 500	40	250,000
Run 2	200 X 200	18	40,000
Run 3	100 X 100	10	10,000

The cameras are placed in the $x-y$ plane of the domain with a camera arc radius of 2.5 times that of the biggest domain dimension, and placed halfway along the z axis (placement is similar to figure 1.2). All cameras have their sensors facing the center of the domain.

3.3 Projection Images

This section presents projection images used to build the equation matrices.

Similar to the construction of projections in section 2.3, projections for the domain with concentration defined by complex torus geometry were built using equation 2.2, where $\boldsymbol{A}_{i,j}$ is the weight matrix constructed using the cylindrical ray tracing model, and $\boldsymbol{g}_j$ is scalar concentration of voxel j, defined by Gaussian concentration modelled with equation 3.1. The product of these two components produces a ray-sum intensity measurement, $\boldsymbol{p}_i$, corresponding to pixel i. Thus, the projection image matrix is assembled by combining the ray-sum intensity signals for all pixels on the camera sensor. The projection images represent the sum of emissive intensity derived from each contributing voxel. Complex geometry 3, for example, appears to have a greater percentage of high levels of concentration

in its projection images, due to the dense distribution of concentration through the domain. These intensities add up along each individual ray reaching the camera sensor.

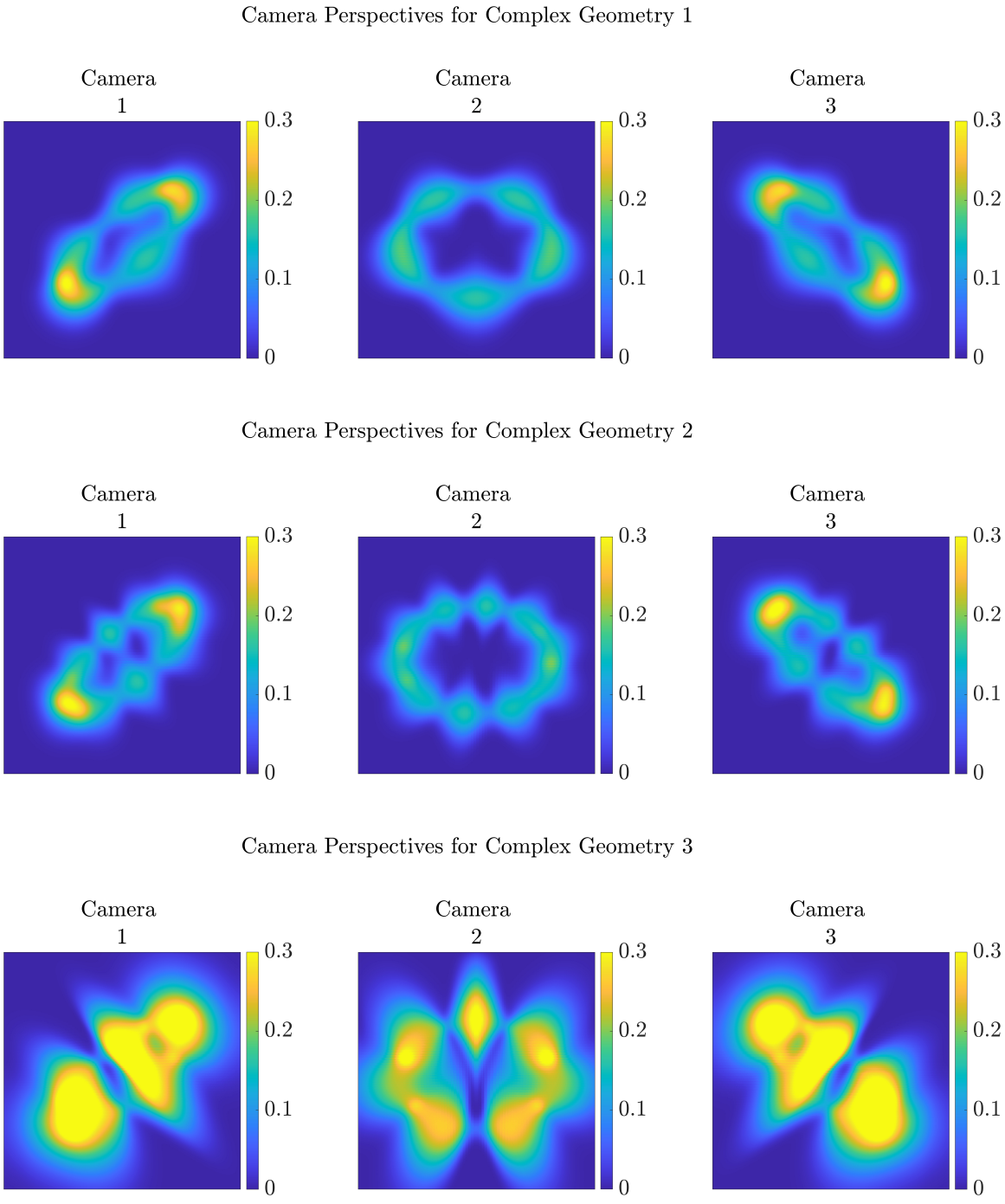

Figure 3.2: Camera Perspectives (500 X 500) for Concentration Defined by an Azimuthally Varying Torus

3.4 Linear Inversion Results

The following figures (3.3, 3.4, 3.5 and 3.6) present slices of the 3D scalar fields at 30%, 50%, and 80% of the specified domain dimension, respectively, for CG1 and CG3. Whilst the reconstructions reproduce a general metric and location of the concentration in the domain, the reconstructions fail to capture a sufficiently precise structure. Additionally, the linear reconstruction introduces noisy data around regions of distinct concentration. This can be attributed to limited perspective angles (in this case, 3), but more significantly, the ill-posed nature of the system of equations.

For relatively simple geometry (CG1), the reconstructions can be considered to be mildly acceptable as a rough initial estimate of concentration. However, for a more complex spread of concentration (CG3), the reconstructions are poor, particularly noticeable in figure 3.6, when observing the XZ slices. For the halfway slice, the reconstruction distributes concentration within roughly one quarter of the cross section, whereas the plot showcasing ground truth paints a different picture. This can be understood by, again, remembering the limited perspective angles and significantly more spatial information introduced to the domain.

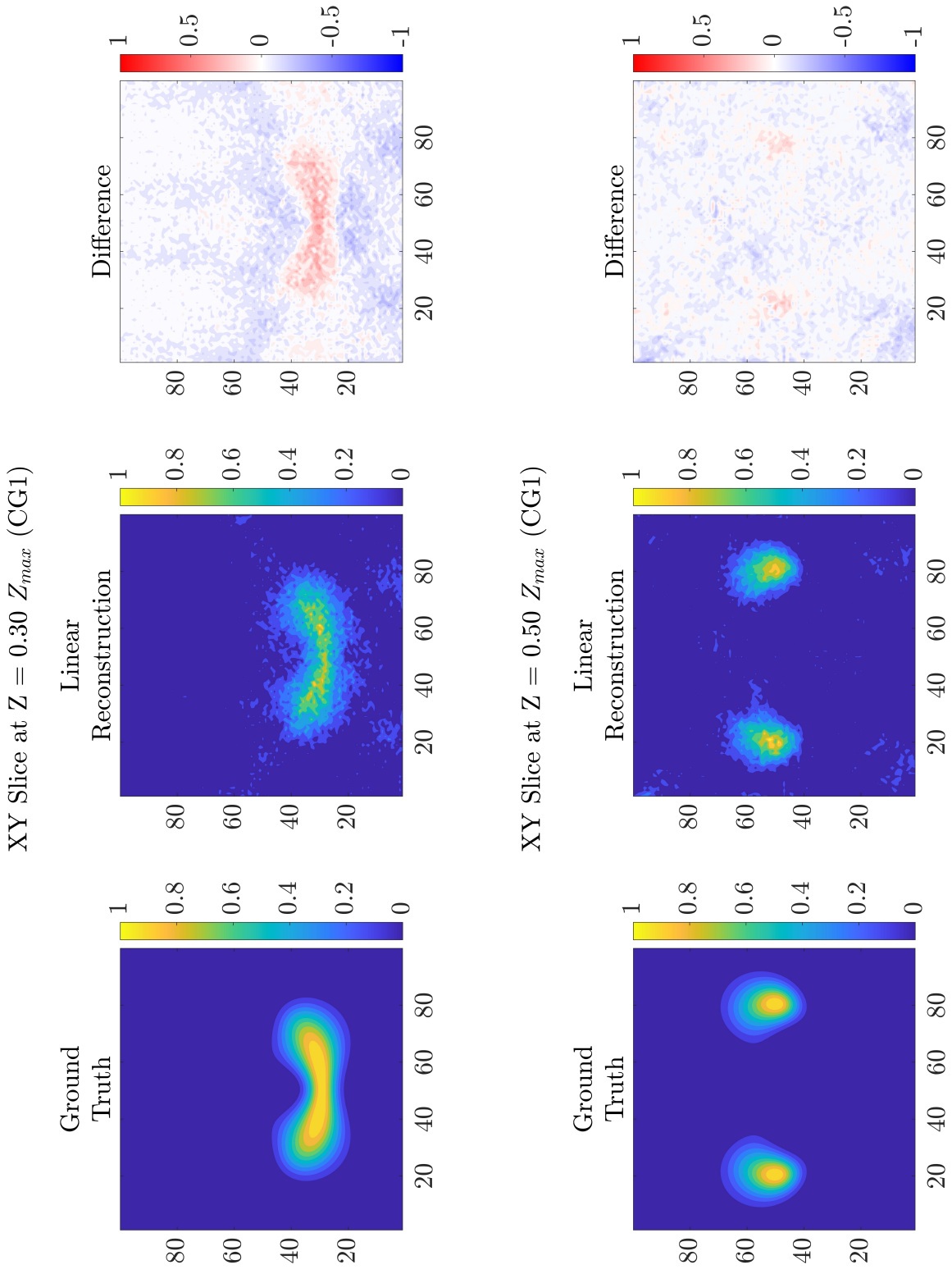

Figure 3.3: XY Slices of Linear Reconstructions for CG1

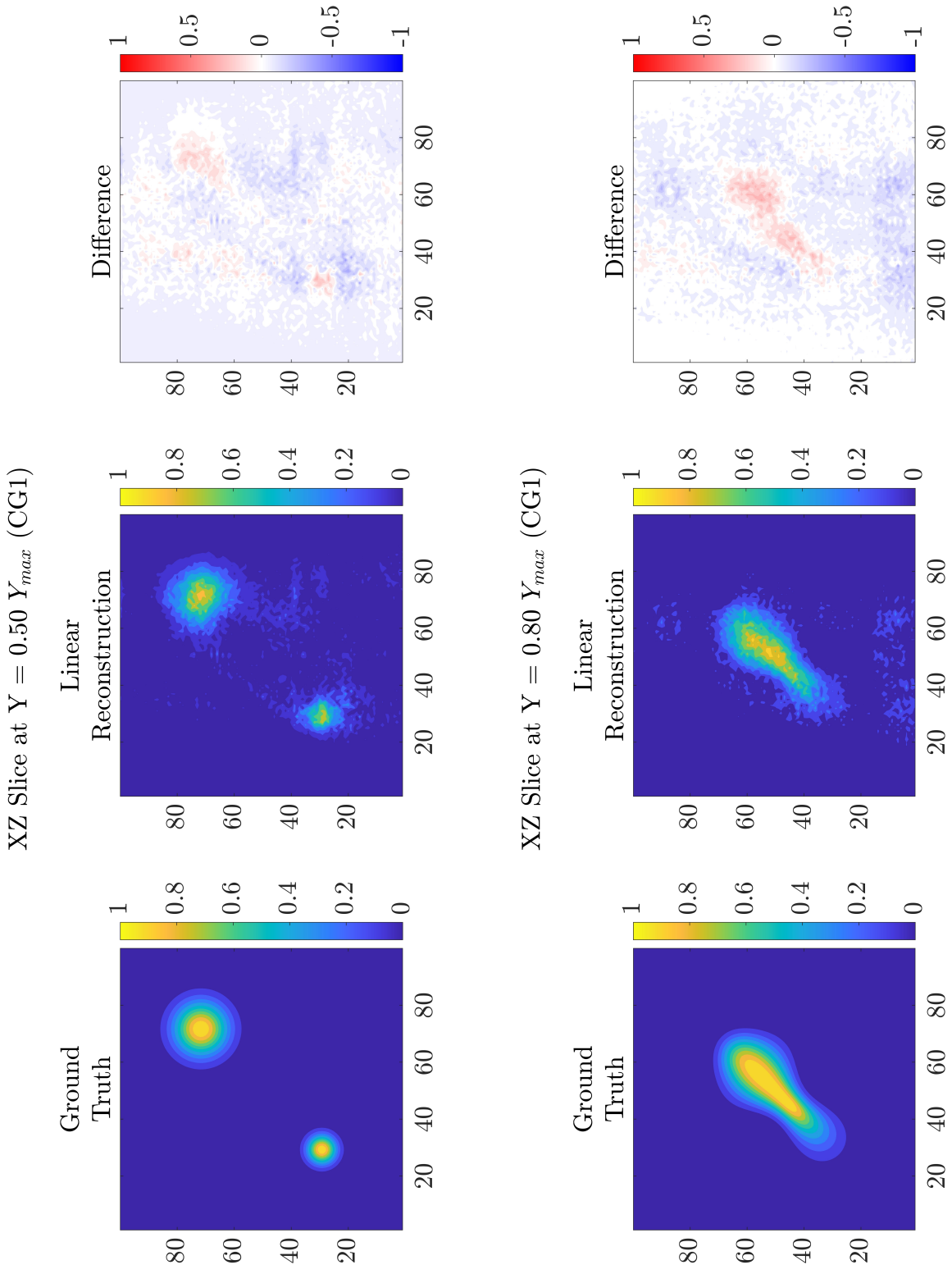

Figure 3.4: XZ Slices of Linear Reconstructions for CG1

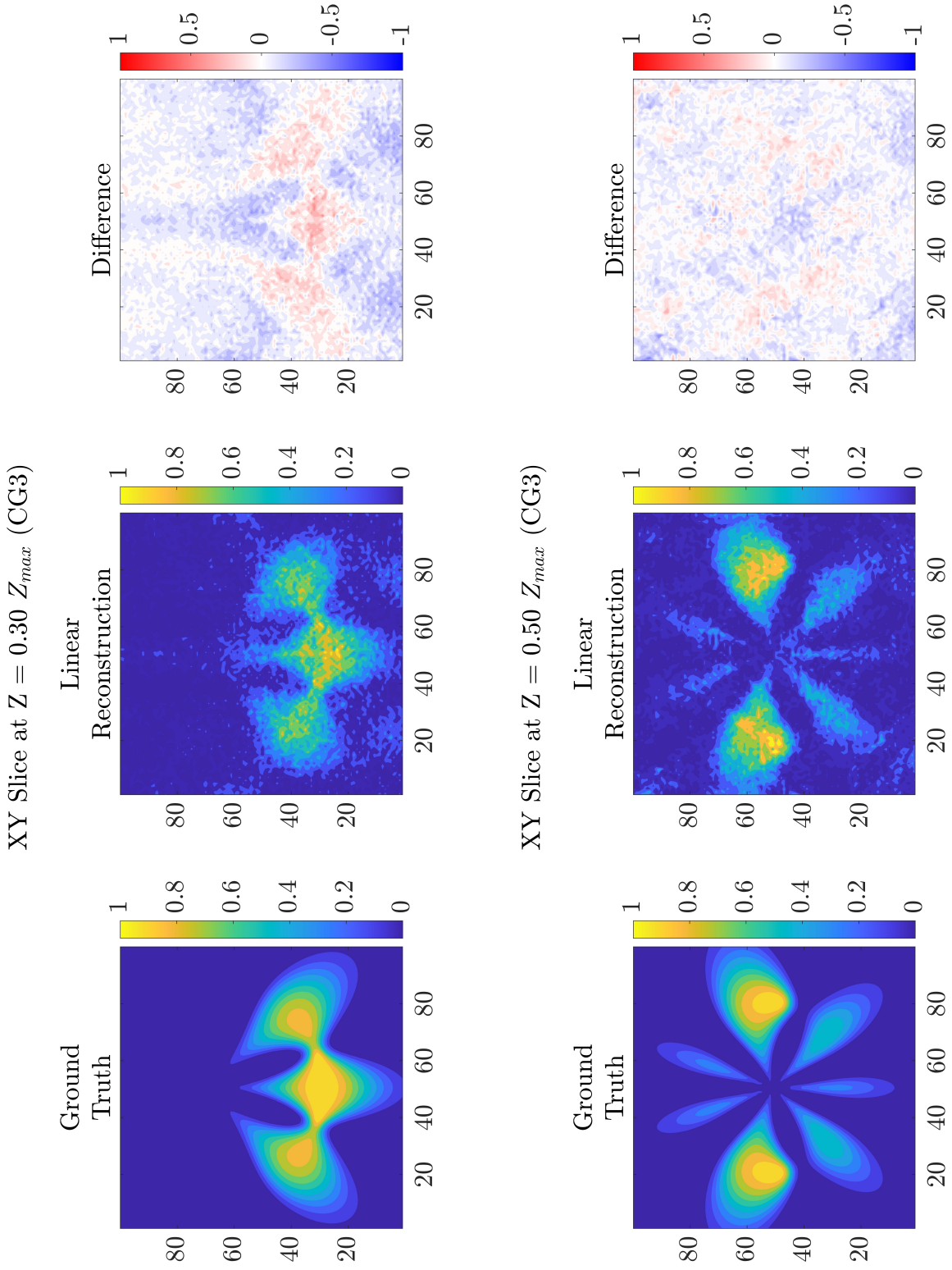

Figure 3.5: XY Slices of Linear Reconstructions for CG3

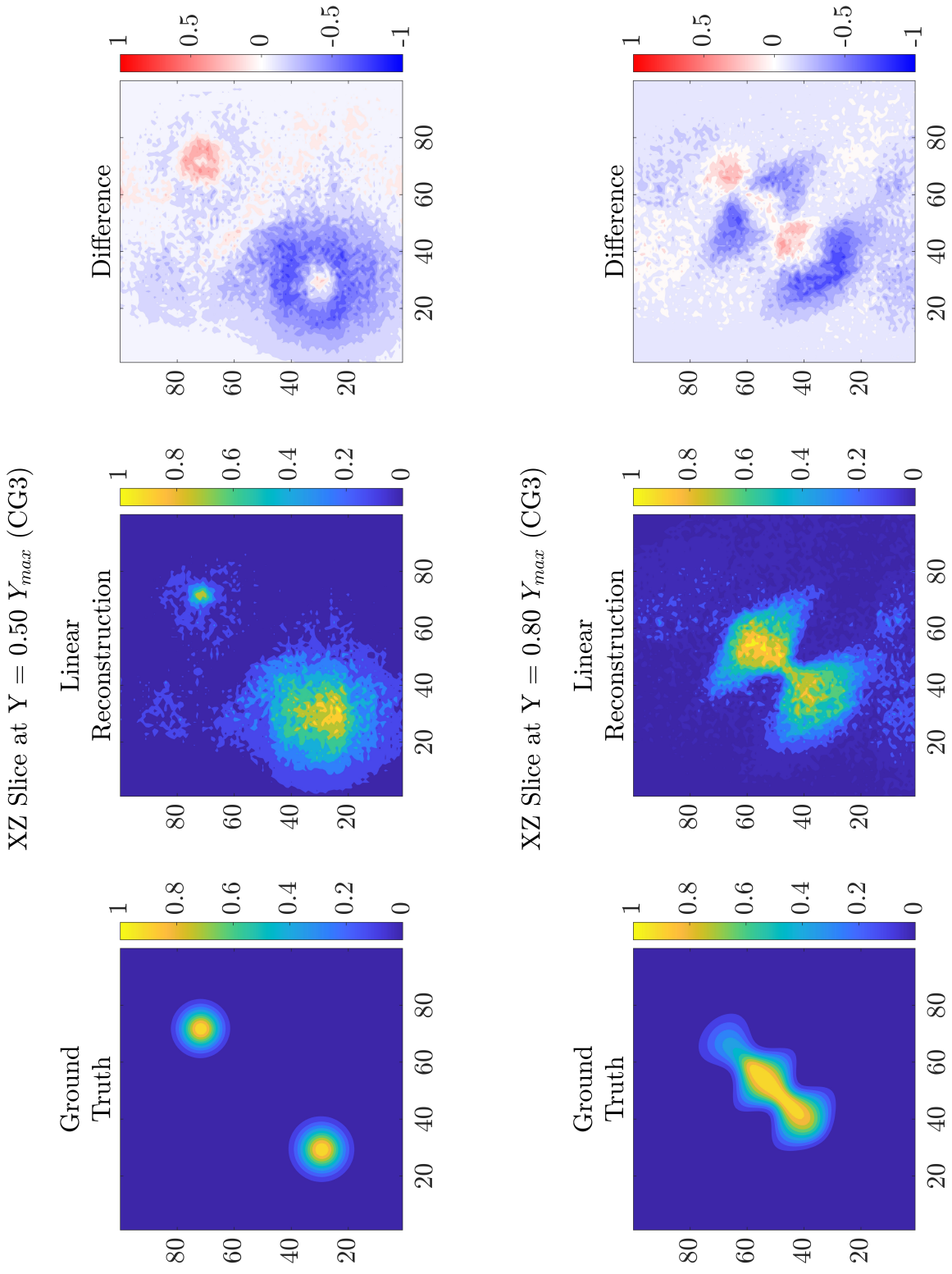

Figure 3.6: XZ Slices of Linear Reconstructions for CG3

3.5 Regularized Inversion Results

The slices presented below depict excellent regularized reconstructions with the regularization parameter, $\lambda = 1e-02$ and $\lambda = 1e-03$. With $\lambda = 1e-05$ and $\lambda = 1e-04$, the reconstructions appear to be closer to the linear inversion reconstructions, highlighting the weak influence of regularization or the lack of the penalty when sharp perturbations are prevalent. On the other had, when $\lambda = 1e-01$, the reconstruction is extremely smooth, thus the distinct variation in concentrations is poorly represented.

A similar conclusion is arrived at when observing the reconstructions of CG3. $\lambda = 1e-02$ and $\lambda = 1e-03$ produce excellent reconstructions, $\lambda = 1e-05$ and $\lambda = 1e-04$ produce reconstructions similar to those via a linear inversion, and $\lambda = 1e-01$ presents a reconstruction that, albeit models the concentration regions well, the reconstruction is very smooth.

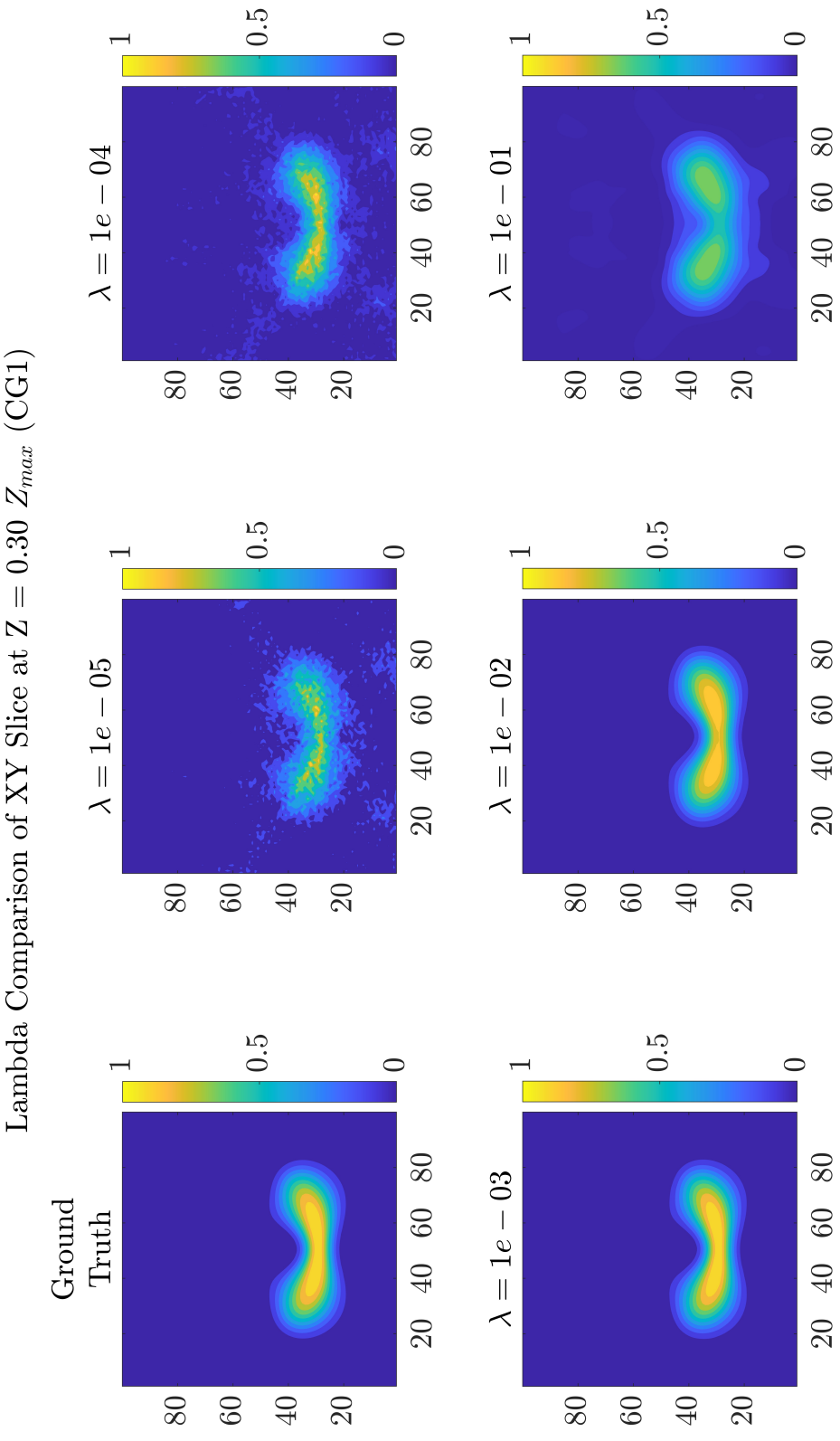

Figure 3.7: XY Slices of Regularized Reconstructions for CG1

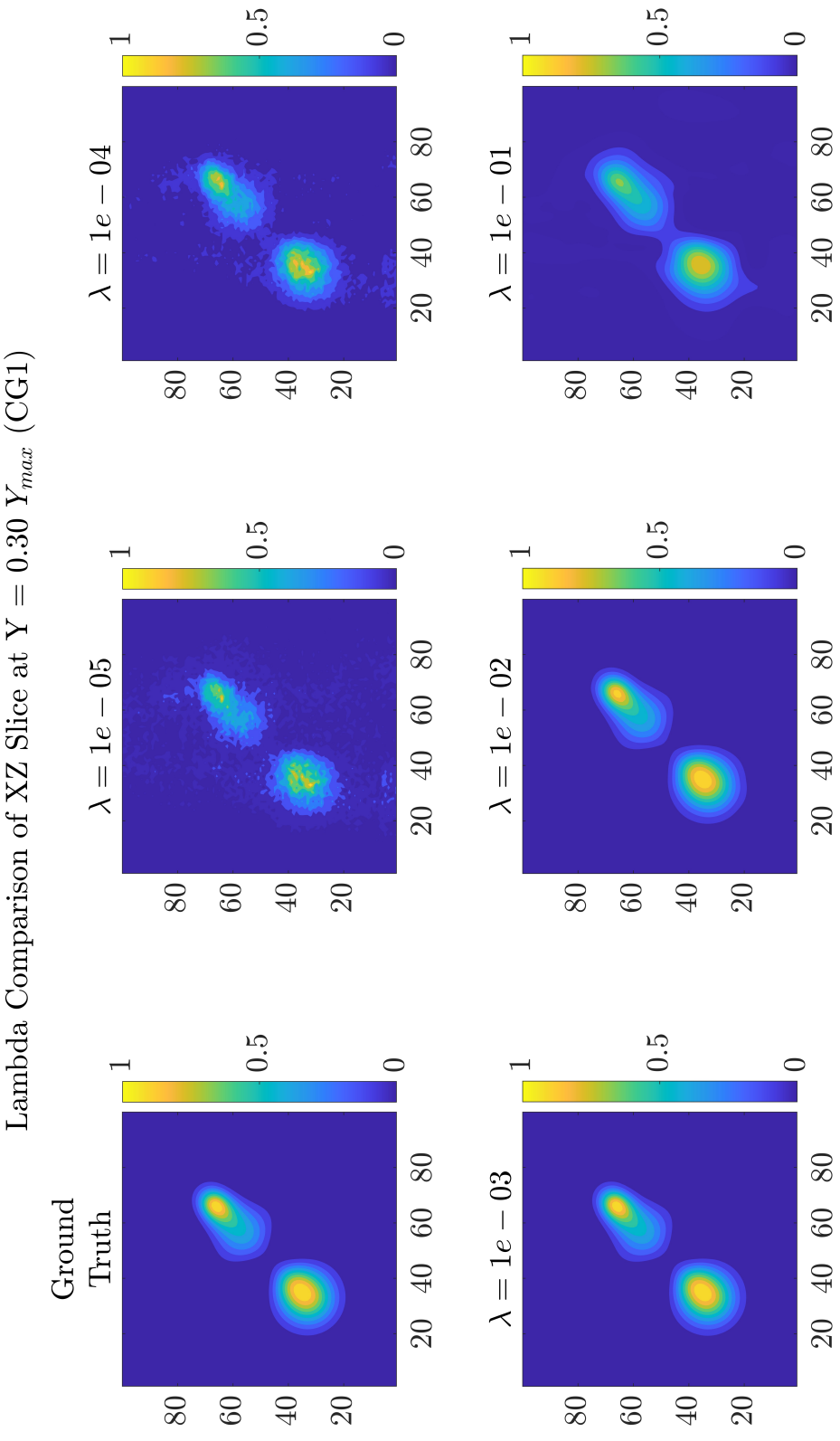

Figure 3.8: XZ Slices of Regularized Reconstructions for CG1

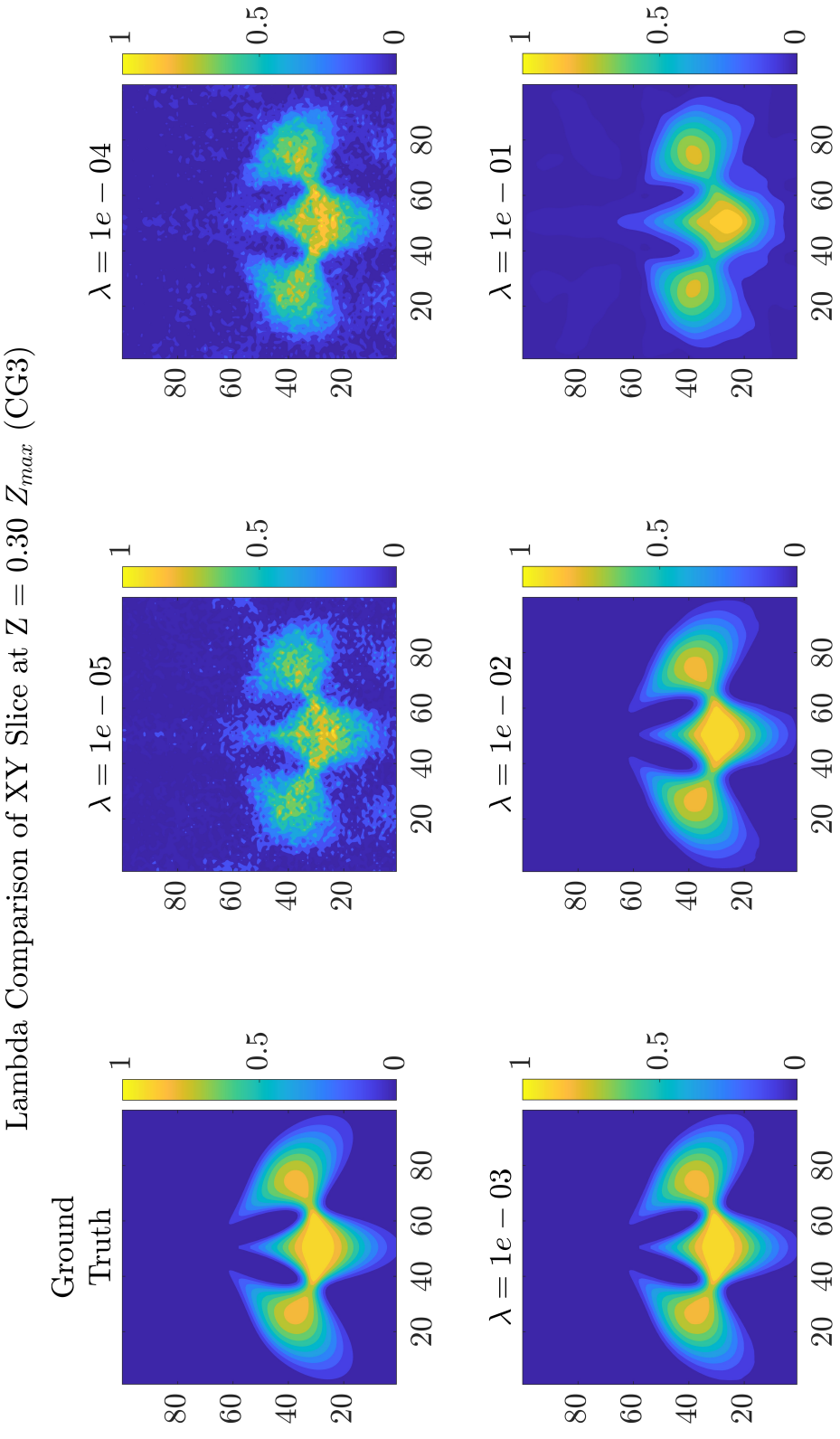

Figure 3.9: XY Slices of Regularized Reconstructions for CG3

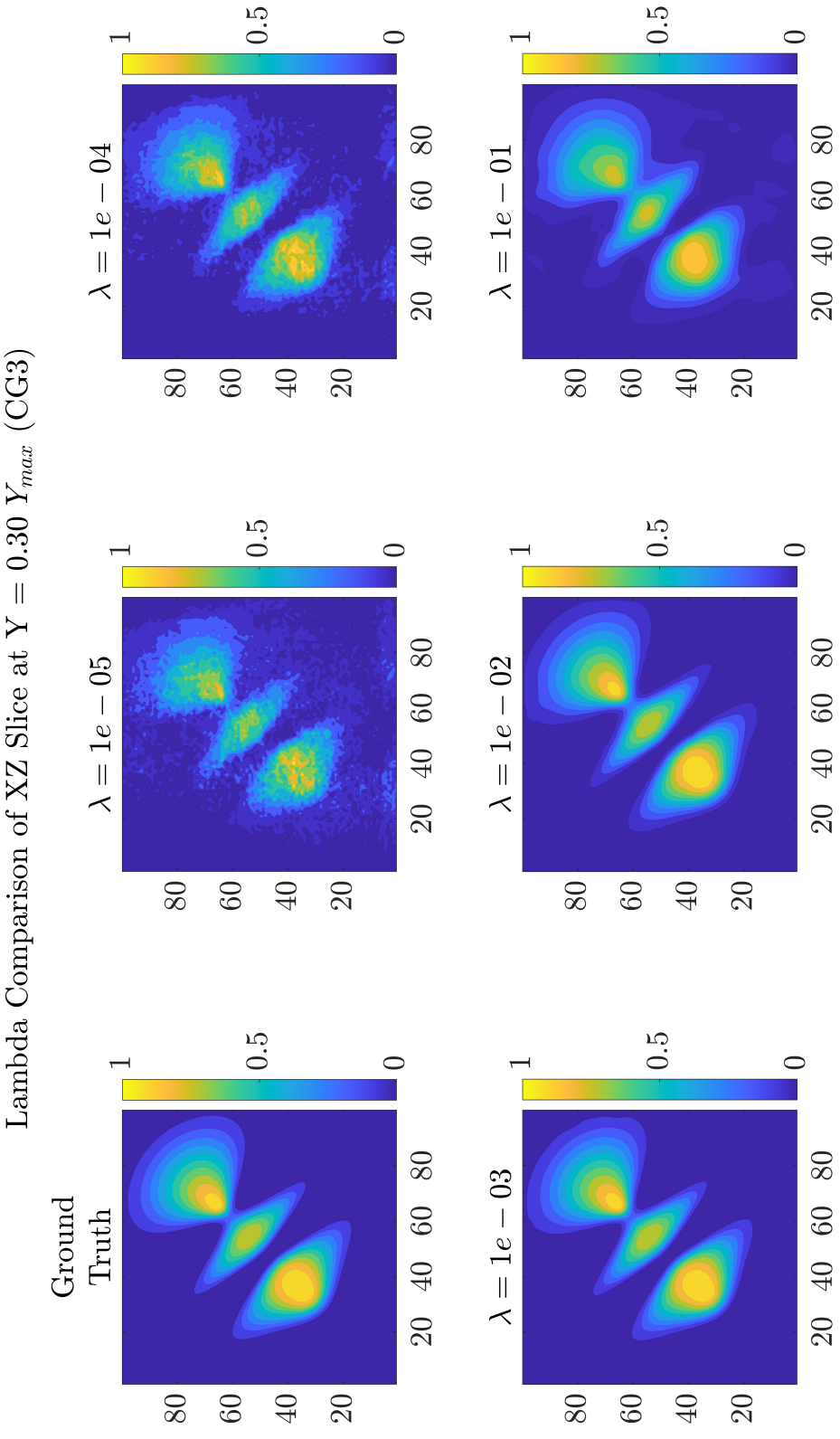

Figure 3.10: XZ Slices of Regularized Reconstructions for CG3

3.6 Reconstruction Accuracy

Error, ϵ, in reconstructions is evaluated using the absolute value based on the following expression:

$$Error, \epsilon = \left| \overline{X_{GT}} - \overline{X_{Tik}} \right| \tag{3.2}$$

where, $\overline{X_{GT}}$ is the ensemble average of original concentration (Ground Truth) and $\overline{X_{Tik}}$ is the ensemble average of concentration reconstructed via Tikhonov regularization.

Figure 3.11 depicts the reconstruction accuracy for each value of λ with a varying camera sensor size. Across all configurations tested, $\lambda = 10^{-3}$ presents the least error (down to 0 in some cases), on average. Anomalies occur when the camera sensors are smaller (have fewer pixels) and the concentration is defined via complex geometry (CG3). The range of error is much smaller when $\lambda = 10^{-2}$, however, and is much closer to 0. λ values on either end of the sweep either penalize the inversion too heavily and produce overly smooth concentration fields, or they do not make a good enough compromise, resulting in regularized inversions that are quite similar to linear inversions. For values of λ lesser than 10^{-3}, the regularization parameter yields results closer to a linear inversion. On the other hand, values of λ greater than 10^{0} gradually smooth the 3D field, producing reconstructions where the field is reproduced with an acceptable distribution of concentration, albeit too smooth.

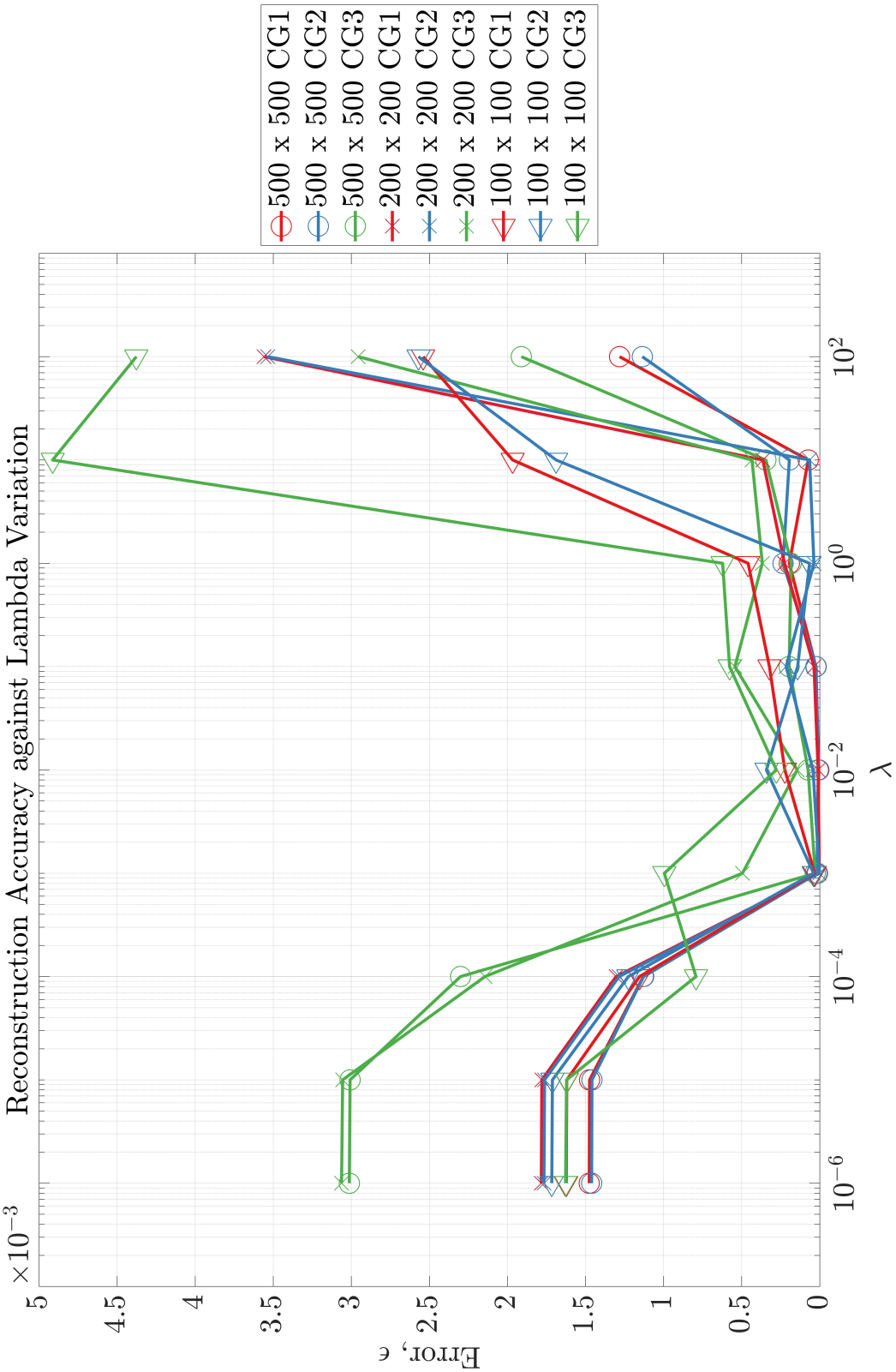

Figure 3.11: Reconstruction Accuracy Against Lambda Variation

To conclude this section, Gaussian concentration as a function of complex torus geometries was mathematically introduced to a cubic domain. Three cameras placed in a circular arc in the XY plane outside the domain imaged the relatively complex 3D field and produced projections. These projections combined with a weight matrix constructed assuming cylindrical rays traversing through the domain to the sensors of the cameras, were linearly inverted using the Least Squares method. Further, a Tikhonov regularization was also performed using a regularization parameter sweep from $\lambda = 10^{-6}$ to $\lambda = 10^{2}$, to evaluate the accuracy of reconstructions.

The linear inversions for CG1 reproduced a general metric and location of concentration in the domain, albeit with noise. As concentration fields became dense, however, the reconstructions failed to capture the intricate structures of the flow field precisely. A halfway slice shows a clear discrepancy between ground truth and the reconstruction; reconstructed concentration is distributed within almost one quarter of the cross section whilst the ground truth slice depicts almost evenly distributed concentration.

The regularized results were more impressive for all complex geometries, with excellent accuracy observed for two values of the regularization parameter, $\lambda = 10^{-3}$ and $\lambda = 10^{-2}$. Due to a significantly lower influence on regularization, reconstructions with $\lambda = 10^{-5}$ and $\lambda = 10^{-4}$ were closer to the results obtained via a linear inversion than ground truth. On the other hand, with $\lambda = 10^{-1}$ and greater, the reconstructions were overly smooth, with a poor representation of the concentration field. Despite the relatively complex and dense concentration fields, the regularized inversions were able to reproduce the 3D fields well.

Finally, the reconstruction accuracy via errors in numerical reproductions was evaluated. Across the λ sweep, setting the regularization parameter to $\lambda = 10^{-3}$ presented the least error, on average, although, certain anomalies were detected with smaller camera sensors and complex geometry (CG3). With $\lambda = 10^{-2}$, the range of error was much smaller, compared to

$\lambda = 10^{-3}$. As expected, λ values on either end of the sweep either penalized the inversion heavily and produced extremely smooth concentration fields, or did not effectively influence regularization, producing results that were particularly similar to linear inversions.

Chapter 4

TURBULENT JET

This chapter presents the domain and camera setups, projection images, and, linear and regularized inversions of concentration provided by DNS Turbulent Jet data. The DNS data used in this section is derived from an 'NGA' simulation of a turbulent jet with a Reynolds number, $Re \approx 5000$. The details of this DNS study are not discussed in this thesis, as the data obtained is only used to produce phantom concentration fields to evaluate the reconstruction accuracy of the imaging models and algorithms. All units in the DNS study are non-dimensional and further information can be found in [10].

4.1 Domain Setup

The domain is initialized as a cuboid of 5 X 2 X 2 non-dimensional units (NDUs) with respect to the jet nozzle diameter of 1 NDU. Each unit length has 50 voxels, thus producing a total voxel count of 2,500,000 voxels. As with the torus setup, the voxel density is chosen to always have more voxels than pixels to produce an under-determined system of equations. 3D concentration in the domain is described by DNS Turbulent Jet data.

4.2 Camera Setup

With a setup similar to that presented in the previous sections, five cameras, each with a sensor size of 500 X 500 pixels, are setup in the xy-plane, halfway along the z axis above the base of the domain. The cameras are placed along a circle arc with a radius of two and half times the length (or width/depth) of the domain (2 NDU). Figure 1.2 is a representative setup, but with five cameras and not three. Cameras are initialized with a focal length of 40mm and all cameras have their sensor facing the center of the domain.

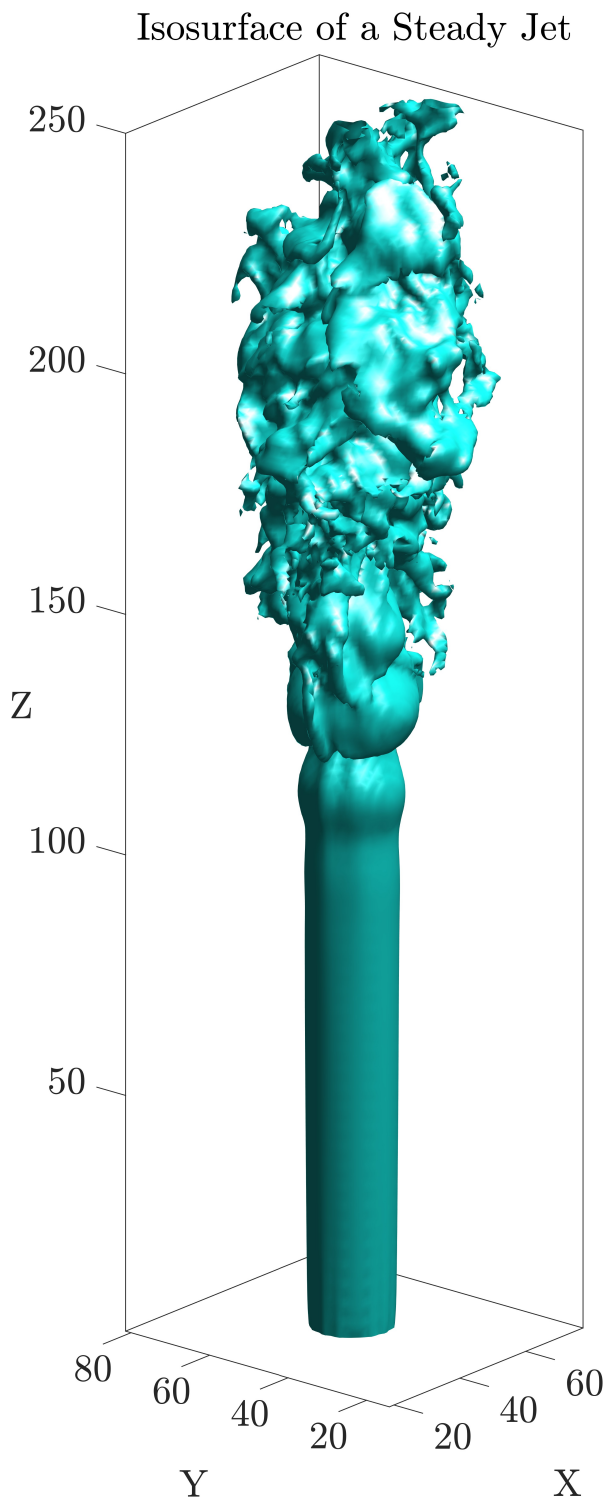

Figure 4.1: Isosurface of a Steady Turbulent Jet

4.3 Projection Images

Projections that the camera sees for Dataset 1 are presented below in figure 4.2.

With concentration in the domain determined by the turbulent jet, projection images were built using equation 2.2, where $\boldsymbol{A}_{i,j}$ is the weight matrix constructed using the cylindrical ray tracing model, and $\boldsymbol{g}_j$ is scalar concentration of voxel j. The product of these two components produces a path-integrated intensity measurement, $\boldsymbol{p}_i$, corresponding to pixel i. Thus, the projection image matrix is assembled by combining the ray-sum intensity signals for all pixels on the camera sensor.

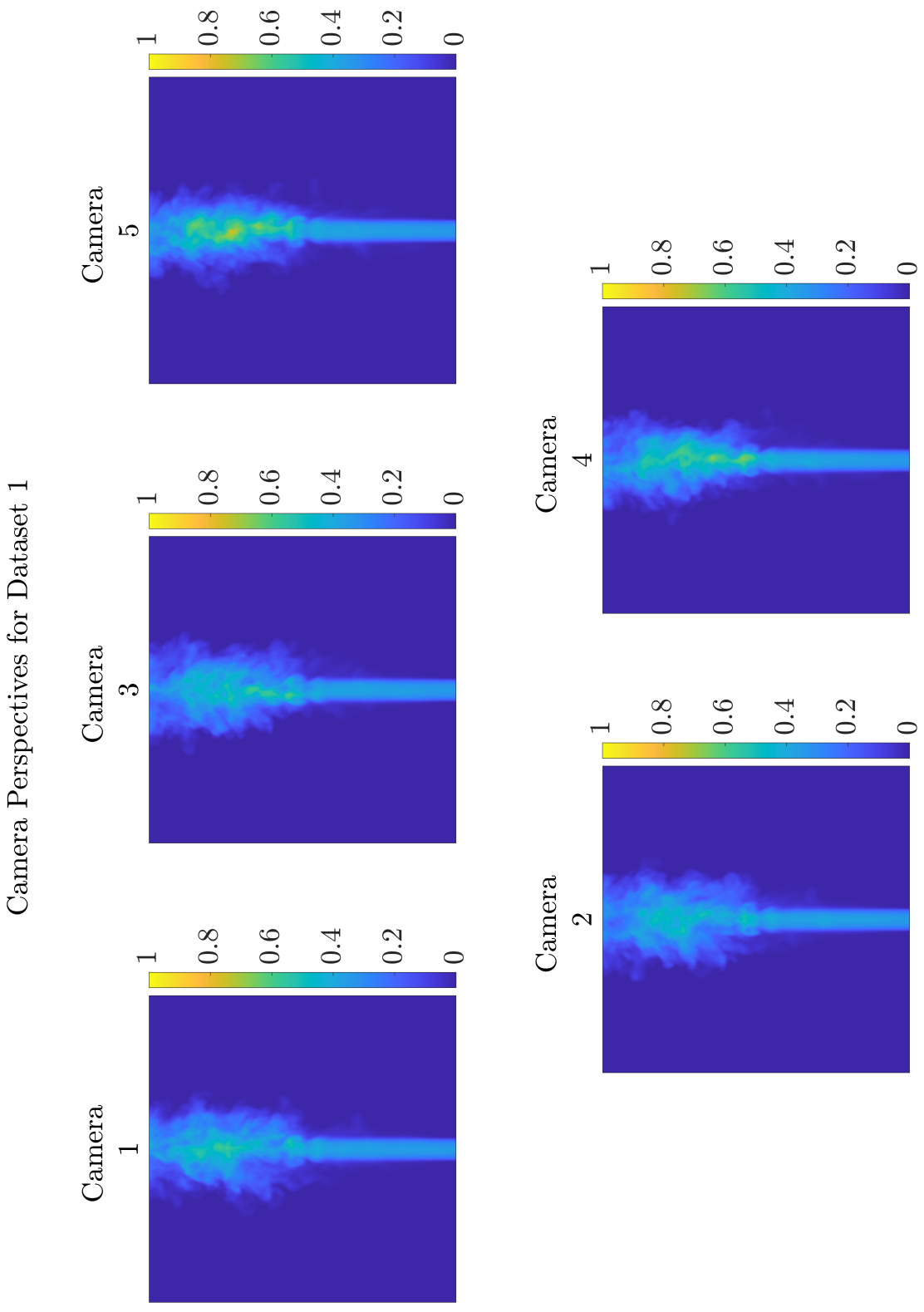

Figure 4.2: Camera Perspectives (500 X 500) for Concentration Defined by a DNS Turbulent Jet (Dataset 1).

4.4 Linear Inversion Results

The following figures (4.3 and 4.4) present XY and XZ slices of the 3D scalar fields at 40%, 50%, and 70% of the specified domain dimension, respectively.

As expected, the general shape and location of concentration fields are captured, however, similar to the case of linear inversion of complex geometries, the reconstructions are noisy. Evident in 4.4, the inversion struggles to accurately reconstruct the core laminar tube of the jet. Further, as the jet transitions into turbulent flow, the inversion is challenged and fails to appropriately reconstruct the fluid structures in this region. In this case, spatial information is particularly dense for a linear inversion to be successful.

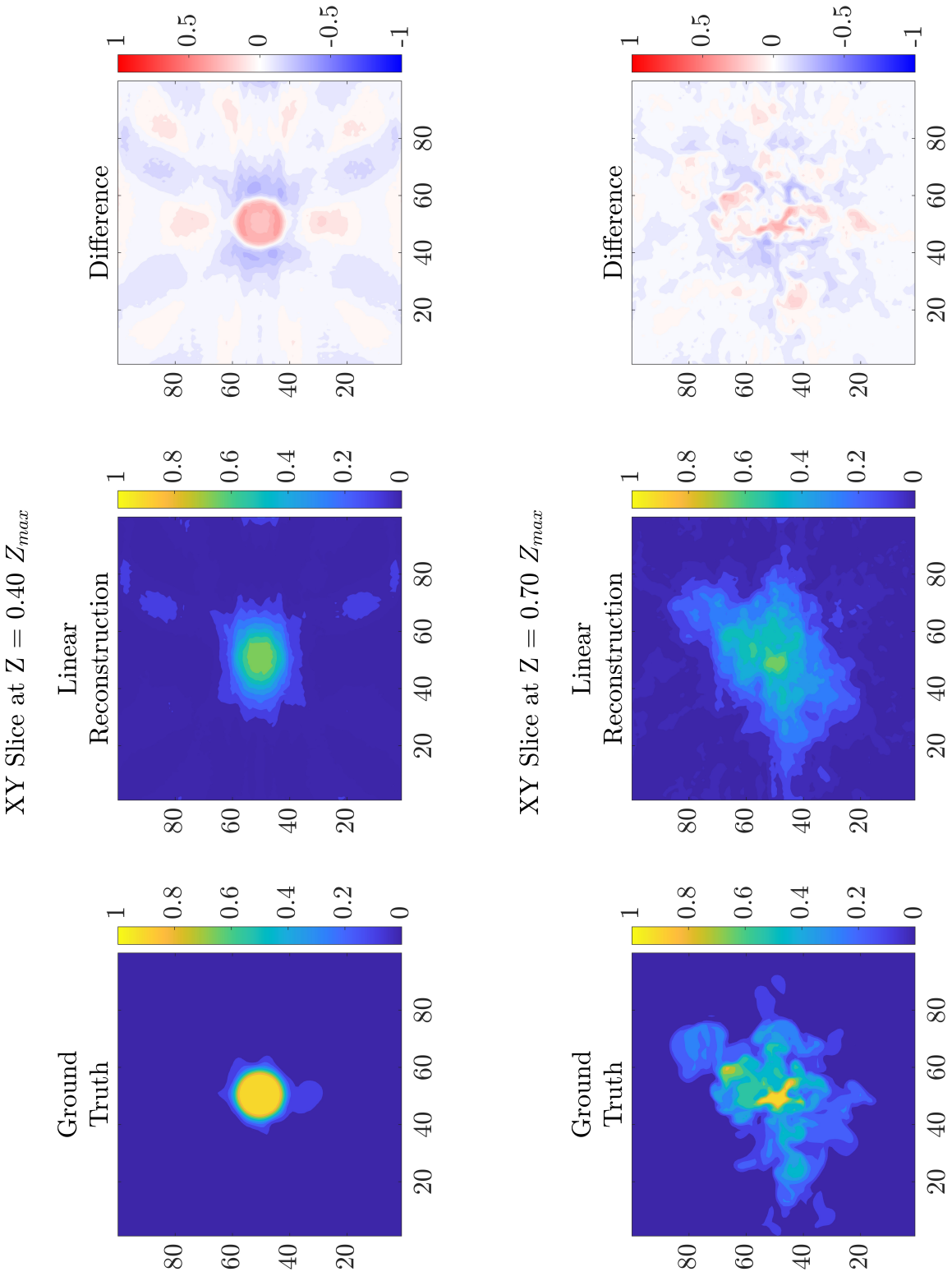

Figure 4.3: XY Slices of Linear Reconstructions of a Turbulent Jet

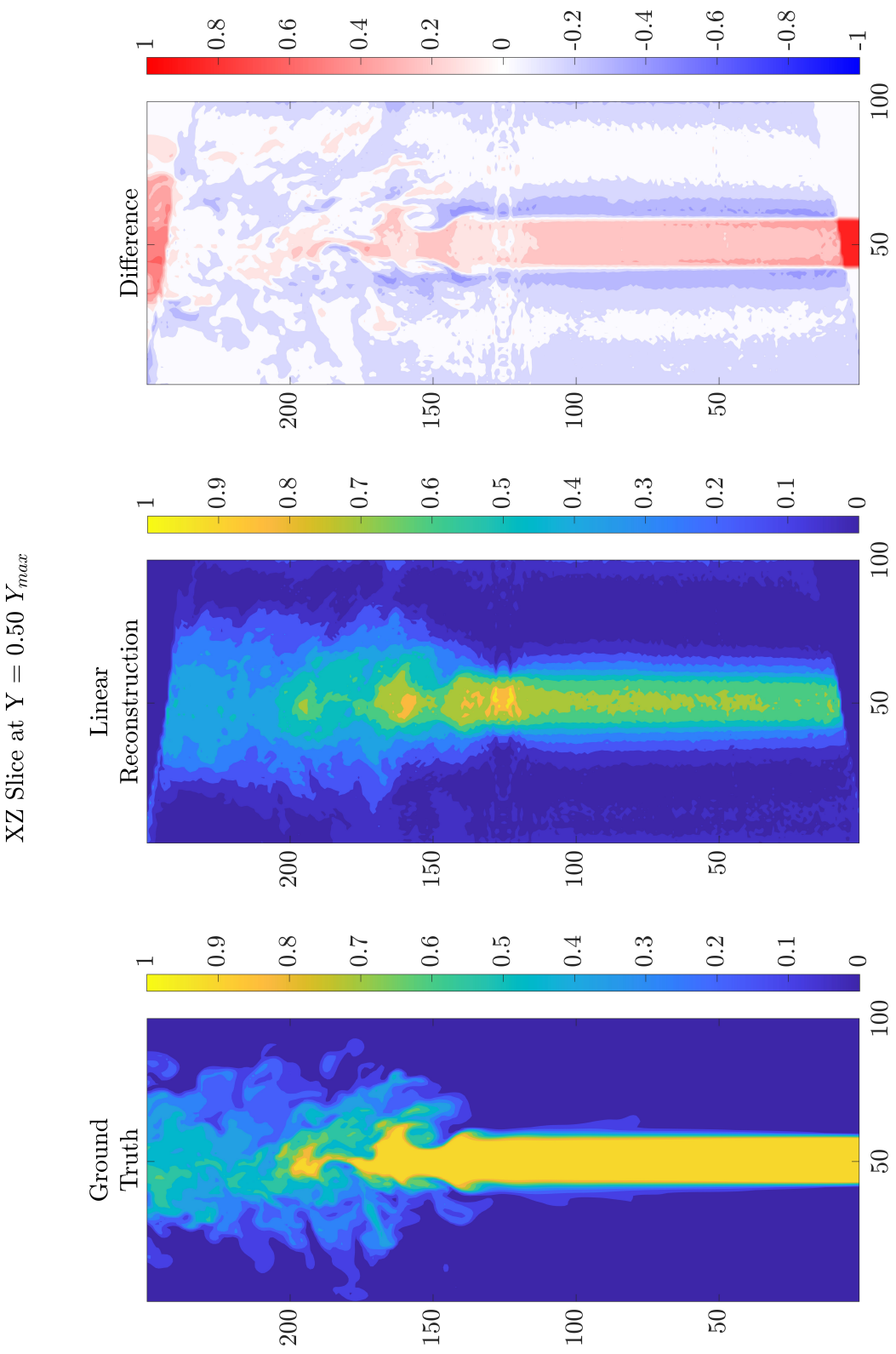

Figure 4.4: XZ Slices of Linear Reconstructions of a Turbulent Jet

4.5 Regularized Inversion Results

The slices presented below display regularized reconstructions of the turbulent jet. The concentration fields evaluated using $\lambda = 10^{-3}$ and $\lambda = 10^{-2}$ appear to be the best reconstructions. As expected, with $\lambda = 10^{-5}$ and $\lambda = 10^{-4}$ the results appear to be closer to the linear inversion reconstructions, and with $\lambda = 10^{-1}$ the concentration field is overly smooth.

Looking at the XZ slices, halfway through the domain, the reconstructions with $\lambda = 10^{-2}$ and $\lambda = 10^{-3}$ present the limitations of the current algorithm to accurately construct the 3D field. This is particularly noticeable in the turbulent region of the jet. When regularized with $\lambda = 10^{-3}$, the reconstructions present discernible structures within the turbulent region of the jet, however, the laminar section has consistent inaccuracies. When $\lambda = 10^{-2}$, however, the laminar portion of the jet is modeled better, but the reconstructions fail to accurately model the structures in the turbulent regime of the jet.

This can be attributed to the smoothing contribution of regularization; regions with almost uniformly distributed concentration can be accurately reconstructed due to the lack of significant spatial variation. When $\lambda = 10^{-3}$, the effects of smoothing are diminished, and the inversion seeks to produce a solution that factors in the minor perturbations in the 3D field.

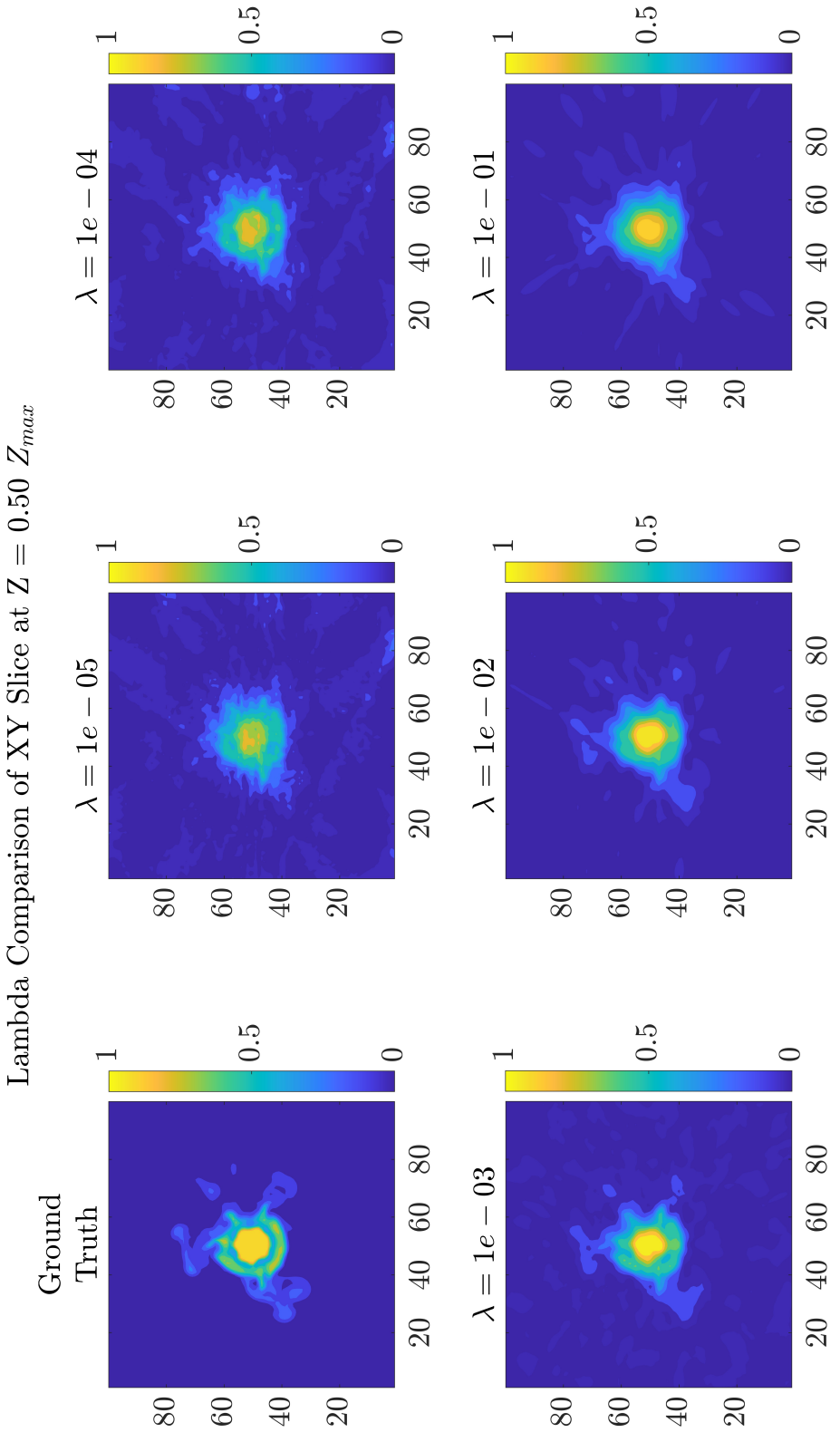

Figure 4.5: XY Slices of Regularized Reconstructions for Dataset 1

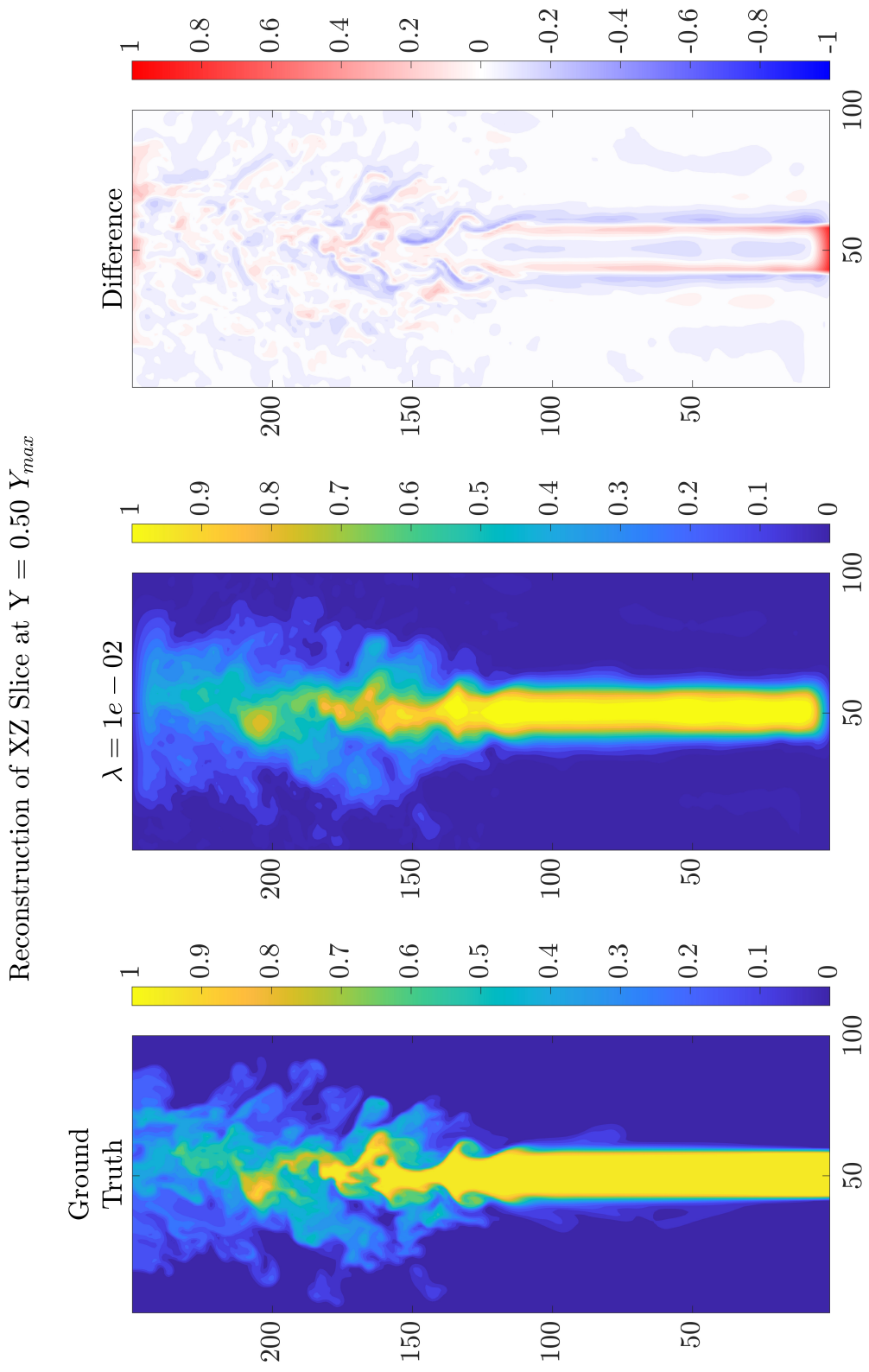

Figure 4.6: XZ Slices of Regularized Reconstructions for Dataset 1

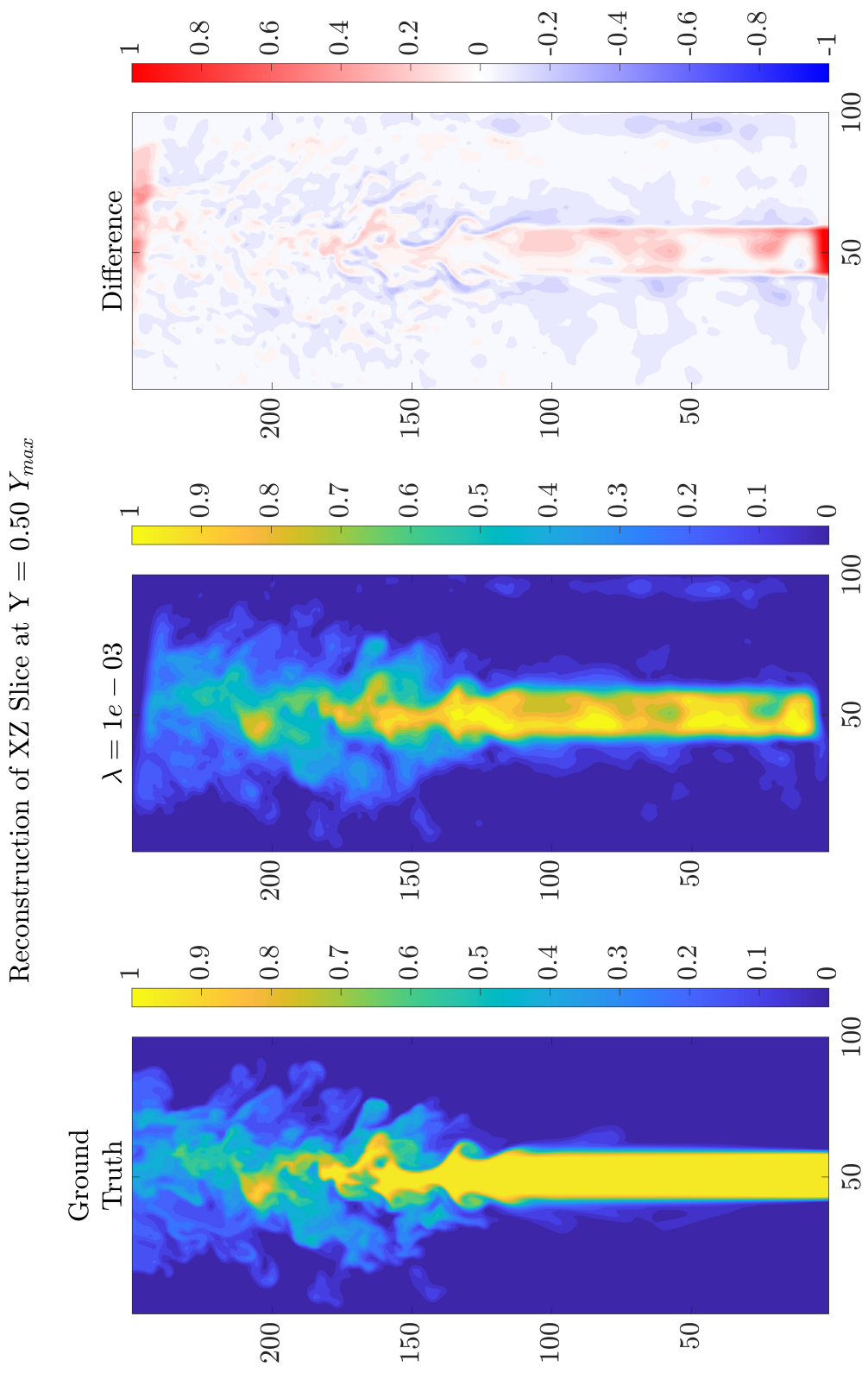

Figure 4.7: XZ Slices of Regularized Reconstructions for Dataset 1

4.6 Reconstruction Accuracy

Figure 4.8 presents reconstruction accuracy for 6 datasets of turbulent jet data and the mean. It is observed that with each successive dataset, reconstruction accuracy improves, especially noticeable when $\lambda = 10^{-3}$. This can be explained by realising that with successive datasets, the turbulent proportion of the jet occupies a greater volume of the domain. Thus, the algorithm reconstructs the minor perturbations of turbulent flow more accurately.

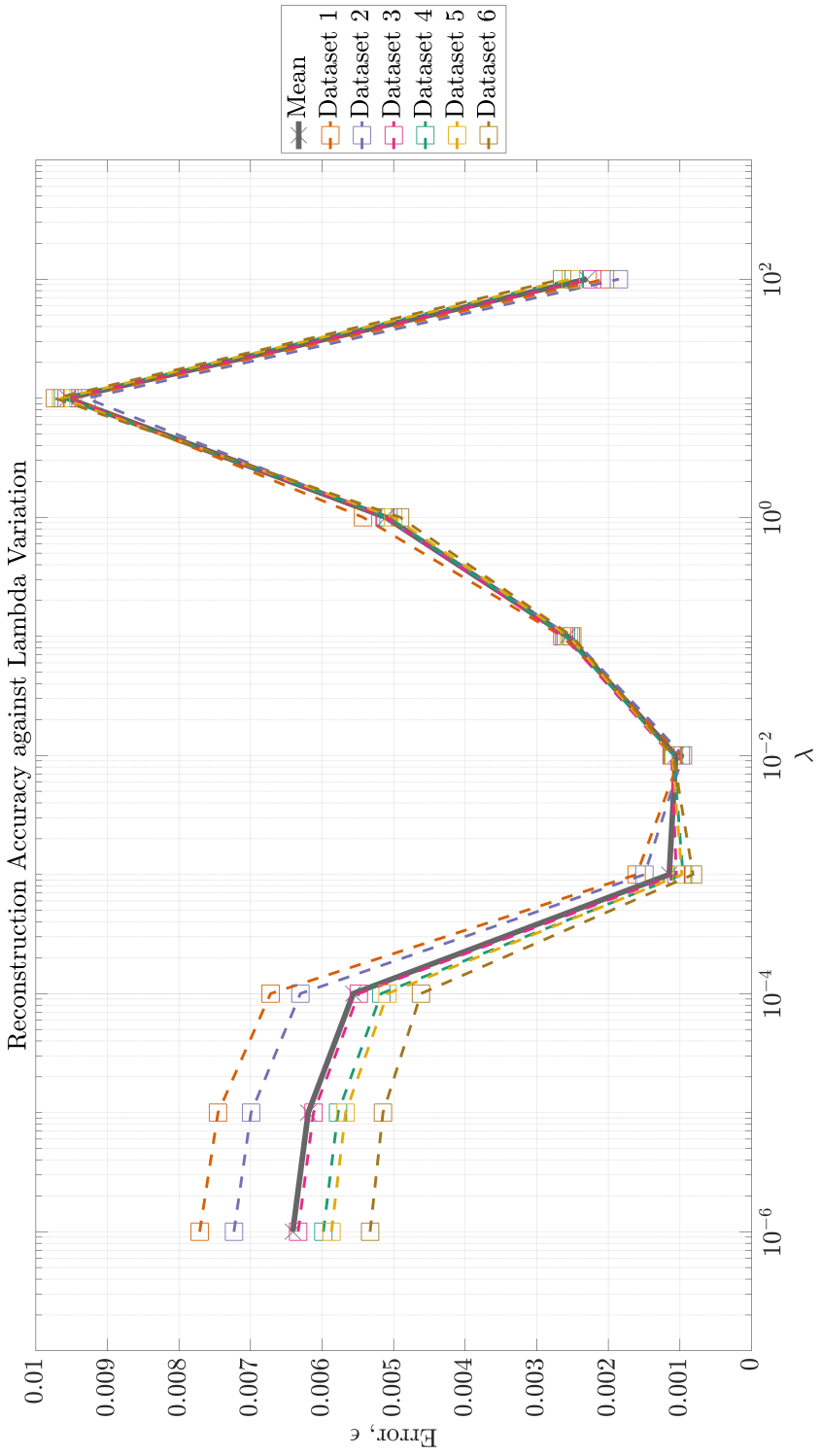

Figure 4.8: Reconstruction Accuracy for Turbulent Jet Data

Chapter 5

CONCLUSIONS AND FUTURE WORK

In conclusion, the limitations of volumetric reconstructions via tomography were evaluated by defining 3D concentration fields using simple and complex torus geometry, and data from a DNS study of a turbulent jet. Assuming a cylindrical ray tracing model, a weight matrix was constructed for each domain, followed by the creation of projection images from multiple perspectives. These were then inverted linearly and using Tikhonov regularization to produce reconstructions of the concentration field. The subsequent results were then analysed, whose results are summarized below.

The reconstructions produced via a linear inversion of concentration modelled by a simple torus depicted excellent accuracy, thereby making the case for an inversion via Tikhonov regularization redundant. When evaluated with complex geometry, the resulting linear reconstructions were inaccurate and noisy, thus necessitating an inversion approach using Tikhonov regularization which produced reconstructions of remarkable accuracy. Lastly, linear inversions of the turbulent jet field were unsurprisingly poor and noisy, and regularized results were also disappointing. For this reason, advanced regularizations are required to reduce reconstruction errors.

5.1 Conclusions from Synthetically Generated Concentration

In the case of concentration defined as a simple torus, the linear and regularized inversions produced excellent reconstructions of the 3D field. However, when $\lambda = 10^{-1}$, the reconstructed field is over-smoothed. Thus, the 3D field does not accurately express the distribution of concentration across the field for this value of λ. Moreover, the regularized

reconstructions present an advantage around computational resources; regularized inversions took about a fifth of the time as compared to linear inversions.

When concentration is defined via complex geometry, it was observed that the reproductions displayed a generalized location of concentration in the domain, whilst failing to present a sufficiently precise structure. The linear inversions also introduced a lot of noise around regions of concentration. This can be put down to limited perspective angles, but more importantly, the ill-posed nature of the system of equations.

When inverting the system of equations via regularization, the 3D fields are excellently reconstructed with the regularization parameter $\lambda = 10^{-2}$ and $\lambda = 10^{-3}$. With $\lambda = 10^{-5}$ and to an extent $\lambda = 10^{-4}$, the reconstructions appear to be closer to those produced via linear inversions, due to the mild influence of the Tikhonov smoothing criteria. On the other end, when $\lambda = 10^{-1}$, the reconstructions produced are very smooth, failing to accurately present the variation in concentration across the field.

Looking at reconstruction accuracy as a function of camera sensor size (in pixels), it was concluded that $\lambda = 10^{-3}$ and $\lambda = 10^{-2}$ presented the least error across all configurations tested. Results from smaller sensors proved that they did not perform as well due to the increased spatial information of the domain. As expected, with values of λ on either end of the range tested, reconstructions were either penalized too heavily and thus produced overly smooth concentration fields, or produced results that were similar to those obtained via linear inversions. λ values less than 10^{-3} yielded results closer to a linear inversion, and vice versa.

5.2 Conclusions from DNS Turbulent Jet Data

Similar to the linear inversion results with complex geometries, the general shape and location of concentration fields are replicated for a turbulent jet. However, the reconstructions

are very noisy. The inversion struggles to accurately reproduce the core tube of the laminar section of the jet. The weakness of a linear inversion is further amplified as the jet transitions to turbulent flow, wherein fluid structures are incorrectly modeled.

On studying the results of the regularized inversion, 3D fields produced with $\lambda = 10^{-3}$ and $\lambda = 10^{-2}$ present the best reconstructions, whilst when $\lambda = 10^{-5}$ and $\lambda = 10^{-4}$, results are closer to those of a linear inversion. When $\lambda = 10^{-1}$, the reconstructed concentration field is too smooth.

The limitations of the algorithm are made clearer when observing XZ slices halfway through the domain. When $\lambda = 10^{-3}$, the laminar section of the jet has consistent inaccuracies, whilst the turbulent region of the jet has discernible structures closely matching with ground truth. Conversely, with $\lambda = 10^{-2}$, the opposite effect is observed; the laminar portion of the jet is modeled well, however, structures in the turbulent regime are not accurately reconstructed. This can be explained with the choice of the regularization parameter. Regions with predominantly homogenous concentration benefit from the smoothing factor due to the lack of minor perturbations in data, whilst in the turbulent region, with the solution less opposed to minor perturbations in the field, the effects of smoothing are reduced.

When comparing the reconstruction accuracy of multiple datasets of the steady turbulent jet, it was observed that with successive dataset, the accuracy improved with $\lambda = 10^{-3}$. This was explained to be due to the turbulent section of the jet occupying an increased volume in the domain, and, as a result, minor perturbations in concentration were reconstructed more accuaretly.

5.3 Future Work

With the conclusion of this thesis, there is still a lot of potential to fully understand the limitations of the approach and refine the technique further:

1. For example, the variation of reconstruction accuracy with increasing voxel density can be studied. This thesis looked at the variation of camera sensor pixels against voxels in the domain. However, the ratio of voxels to pixels was restricted to a small range to solely determine the effect of varying sensor size. Future work can settle on one sensor size, and present the results of reconstruction accuracy as a function of voxel density in the domain.

2. Another suggestion would be to study the effects of varying the masking threshold, to analyse its impact on reconstructions. For this work, all regularized results also included a 3D mask applied to the projection images, albeit with a very low threshold. This was done in this manner as the data used to populate the domain with concentration was purely synthetic, and would not have made a significant difference to the reconstructions.

3. Finally, this imaging and reconstruction technique can be adapted to Absorption Tomography.

The scope for future work lies in applying the lessons learned towards experimental data and images acquired. Work with experimental data would require a camera calibration to be performed, followed by a domain sizing operation, with suitable ray tracing imaging models. Finally, spectral processing conducted with information about the camera sensors would be the penultimate step to running the tool to produce reconstructions of the chosen flow phenomenon.

BIBLIOGRAPHY

[1] Bauer, F. J., Braeuer, P. A., Wilke, M. W., Will, S. and Grauer, S. J. [2023], '2D in situ determination of soot optical band gaps in flames using hyperspectral absorption tomography', Combustion and Flame p. 112730.
URL: *https://www.sciencedirect.com/science/article/pii/S0010218023001153*

[2] Bianchi, D., Buccini, A., Donatelli, M. and Serra-Capizzano, S. [2015], 'Iterated fractional Tikhonov regularization', Inverse Problems **31**(5), 055005.
URL: *https://iopscience.iop.org/article/10.1088/0266-5611/31/5/055005*

[3] Daun, K. [2010a], 'Infrared species limited data tomography through tikhonov reconstruction', Journal of Quantitative Spectroscopy and Radiative Transfer **111**(1), 105–115.
URL: *https://www.sciencedirect.com/science/article/pii/S002240730900260X*

[4] Daun, K. [2010b], 'Infrared species limited data tomography through Tikhonov reconstruction', Journal of Quantitative Spectroscopy and Radiative Transfer **111**(1), 105–115.
URL: *https://linkinghub.elsevier.com/retrieve/pii/S002240730900260X*

[5] GC, A. [2023], 'Formatting your thesis or dissertation', ASU GC .

[6] Grauer, S. [2018], Bayesian Methods for Gas-Phase Tomography, PhD Thesis, University of Waterloo.

[7] Grauer, S. J., Mohri, K., Yu, T., Liu, H. and Cai, W. [2023], 'Volumetric emission tomography for combustion processes', Progress in Energy and Combustion Science **94**, 101024.
URL: *https://linkinghub.elsevier.com/retrieve/pii/S0360128522000338*

[8] Haines, E. and Akenine-Möller, T., eds [2019], Ray Tracing Gems: High-Quality and Real-Time Rendering with DXR and Other APIs, Apress, Berkeley, CA.
URL: *http://link.springer.com/10.1007/978-1-4842-4427-2*

[9] Haines, E., Günther, J. and Akenine-Möller, T. [2019], Precision Improvements for Ray/Sphere Intersection, Apress, Berkeley, CA, pp. 87–94.
URL: *https://doi.org/10.1007/978-1-4842-4427-2*$_7$

[10] Paturu, V. S. S. [2023], Preliminary Studies of Scalar Transport in Turbulent Jets Using Point-Particle DNS Simulations, Masters Thesis, Arizona State University.

[11] Pope, S. B. [2011], Turbulent flows, Cambridge Univ. Press, Cambridge.
URL: *https://cds.cern.ch/record/1346971*

[12] Samei, E. and Pelc, N. J. [2020], 'Computed tomography: Approaches, applications, and operations', Computed Tomography .

[13] Webb, S. [1990], From the watching of shadows: the origins of radiological tomography, A. Hilger, Bristol ; New York.

[14] Wei, C. and Schwarm, K. K. [2020], 'Volumetric laser absorption imaging of temperature, CO and CO_2 in laminar flames using 3D masked Tikhonov regularization', Combustion and Flame .

[15] Wei, C., Schwarm, K. K., Pineda, D. I. and Spearrin, R. M. [2021], 'Volumetric laser absorption imaging of temperature, CO and CO 2 in laminar flames using 3D masked Tikhonov regularization', Combustion and Flame **224**, 239–247.
URL: *https://linkinghub.elsevier.com/retrieve/pii/S001021802030451X*

[16] Wernick, M. N. and Aarsvold, J. N. [2004], Emission tomography the fundamentals of pet and spect, Elsevier Academic Press.

[17] Williams, A., Barrus, S., Morley, R. and Shirley, P. [2005], 'An efficient and robust ray-box intersection algorithm', J. Graphics Tools **10**, 49–54.

[18] Yang, X.-J. and Wang, L. [2015], 'A modified Tikhonov regularization method', Journal of Computational and Applied Mathematics **288**, 180–192.
URL: *https://linkinghub.elsevier.com/retrieve/pii/S0377042715002290*

[19] Zhou, H.-C., Han, S.-D., Sheng, F. and Zheng, C.-G. [2002], 'Visualization of three-dimensional temperature distributions in a large-scale furnace via regularized reconstruction from radiative energy images: numerical studies', Journal of Quantitative Spectroscopy and Radiative Transfer **72**(4), 361–383.
URL: *https://linkinghub.elsevier.com/retrieve/pii/S0022407301001303*

APPENDIX A

ADDITIONAL TORUS RESULTS AND IMAGES

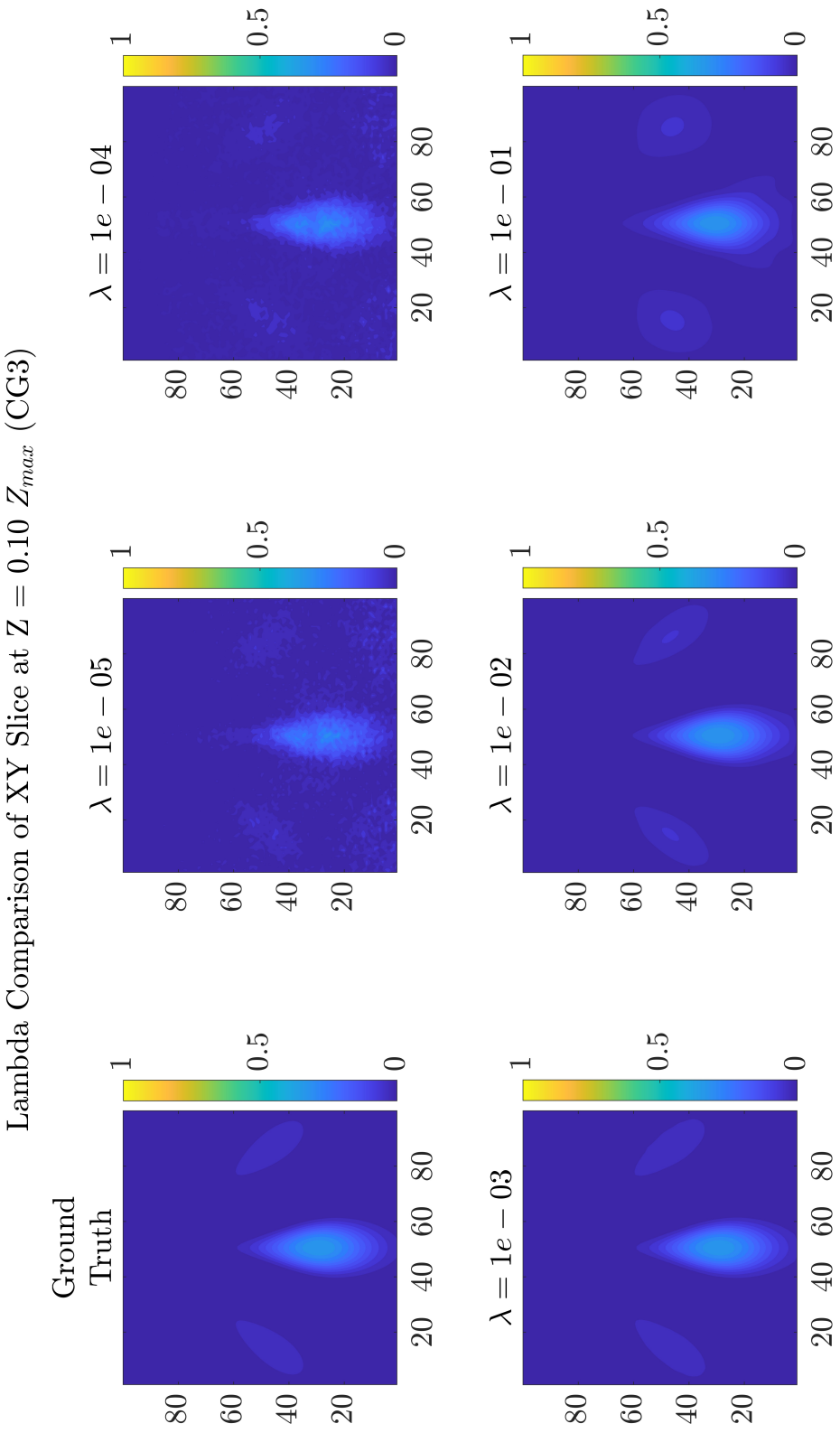

Figure A.1: XZ Slices of Regularized Reconstructions for CG3

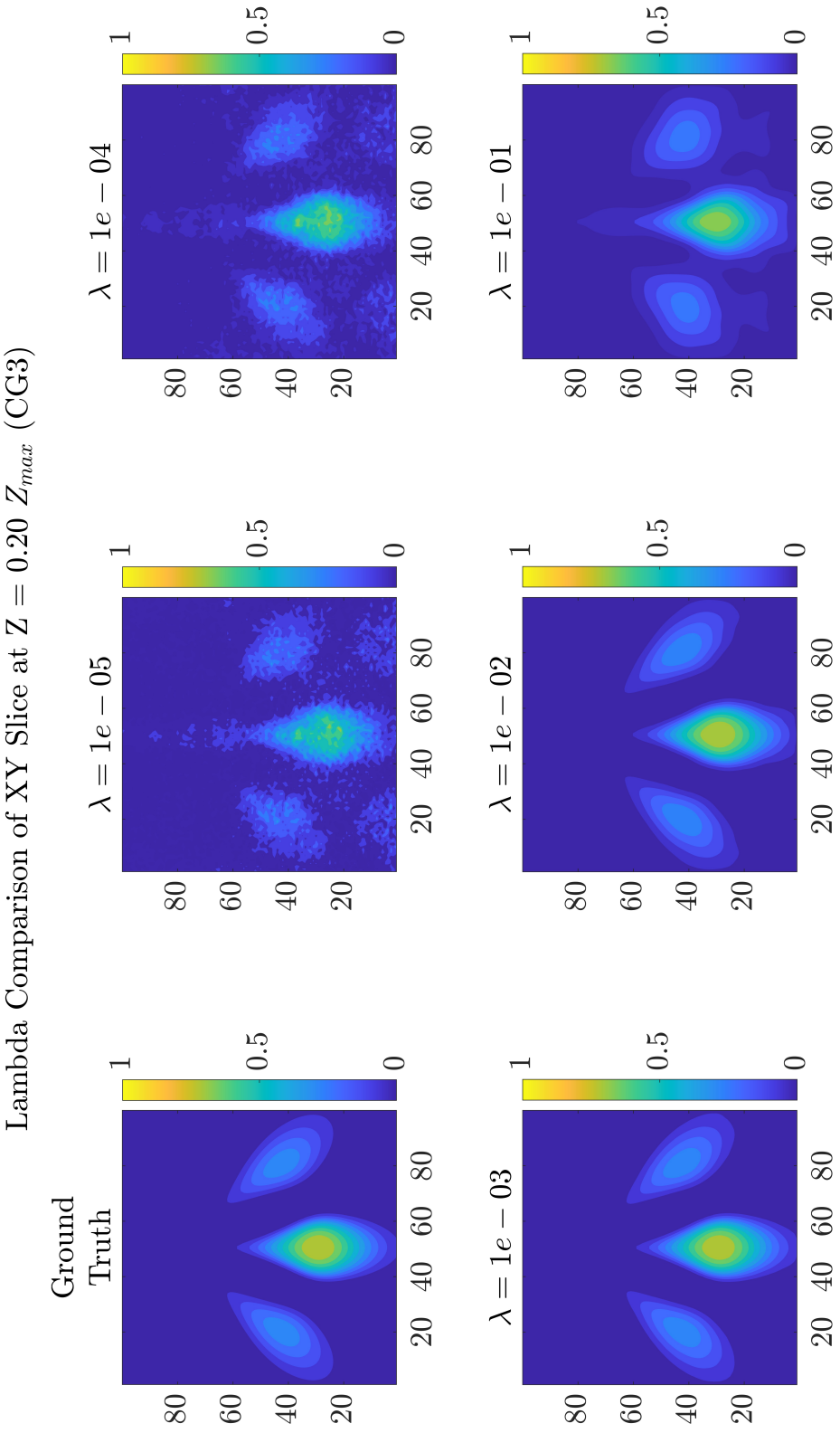

Figure A.2: XZ Slices of Regularized Reconstructions for CG3

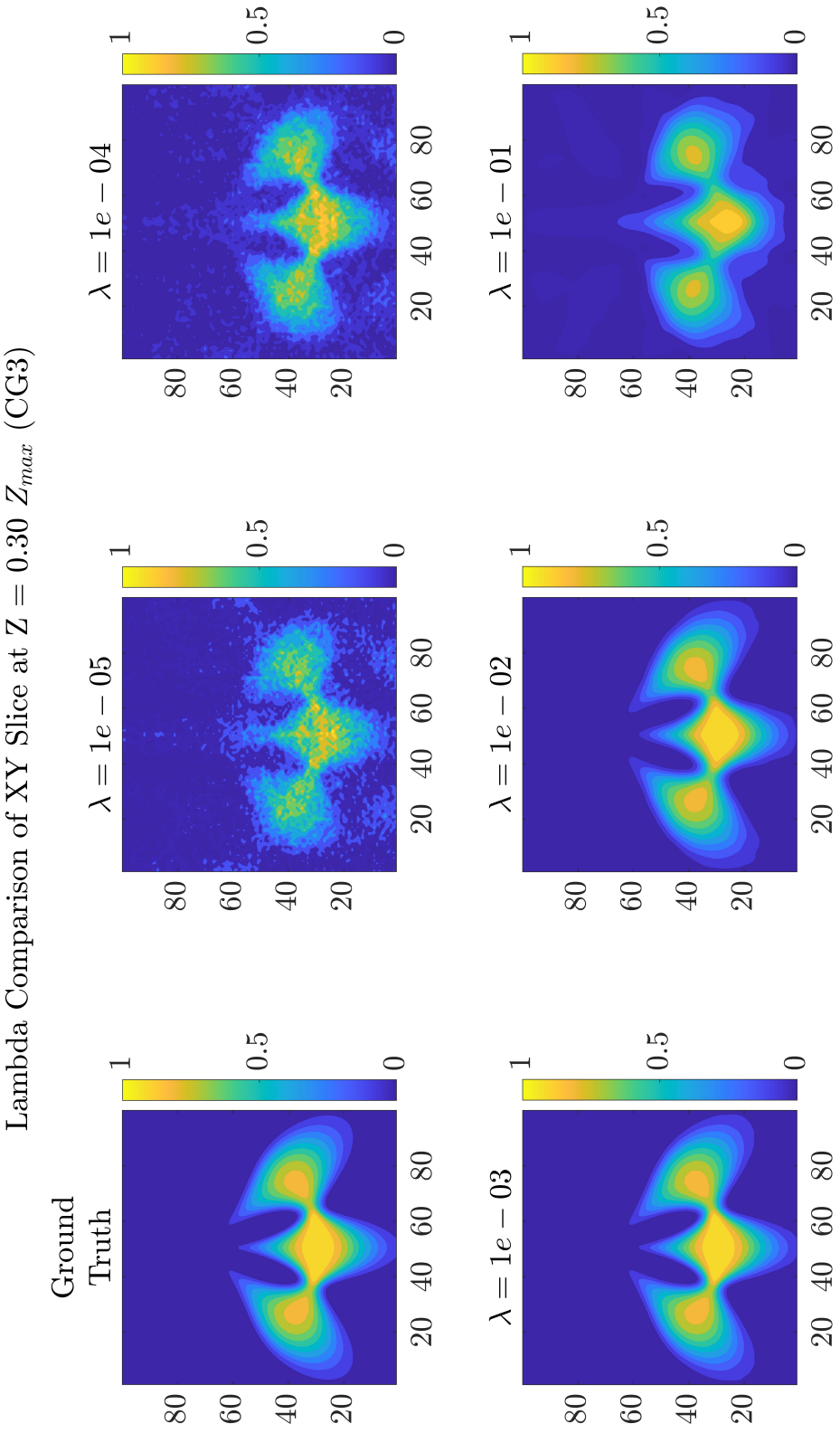

Figure A.3: XZ Slices of Regularized Reconstructions for CG3

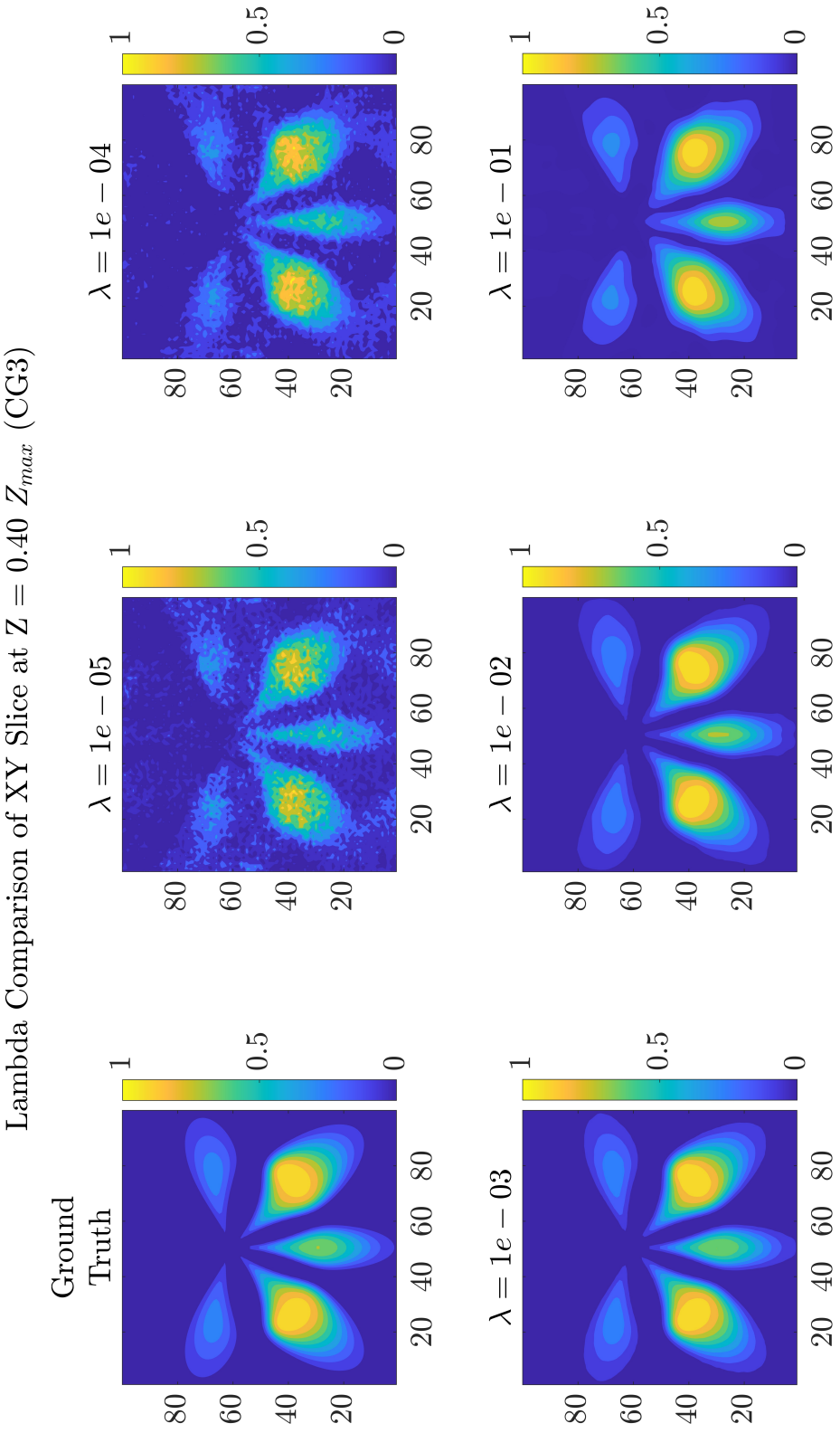

Figure A.4: XZ Slices of Regularized Reconstructions for CG3

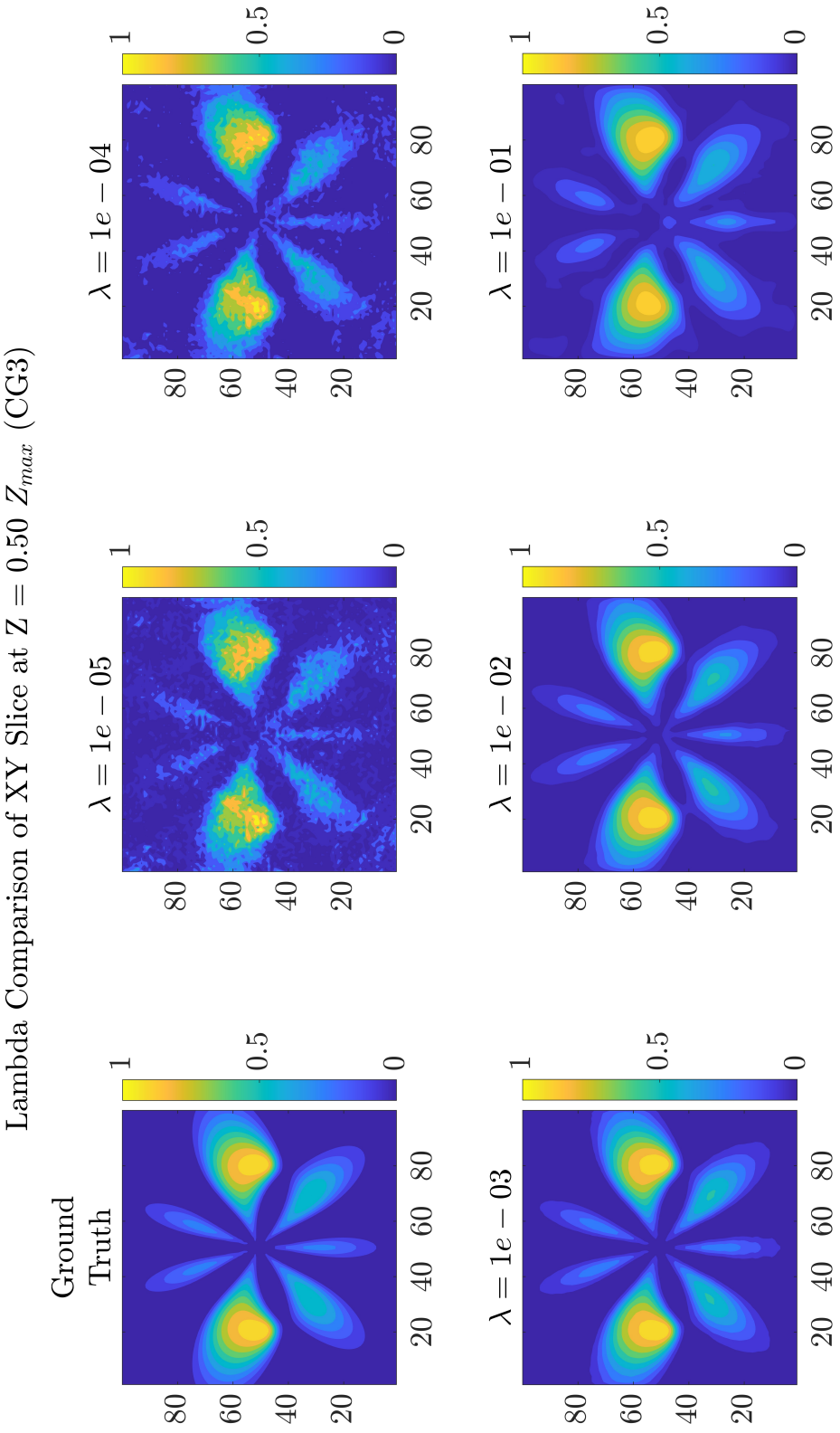

Figure A.5: XZ Slices of Regularized Reconstructions for CG3

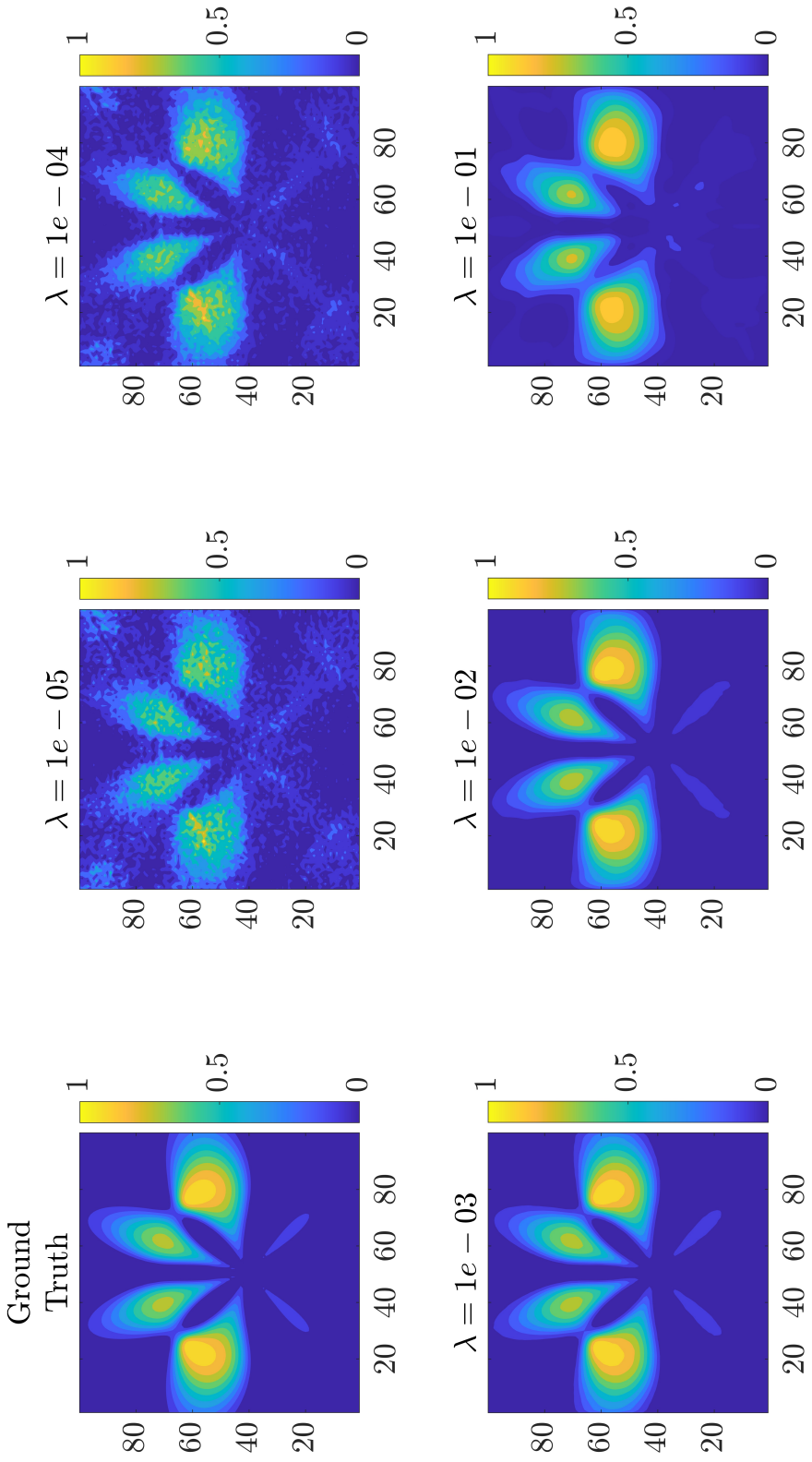

Figure A.6: XZ Slices of Regularized Reconstructions for CG3

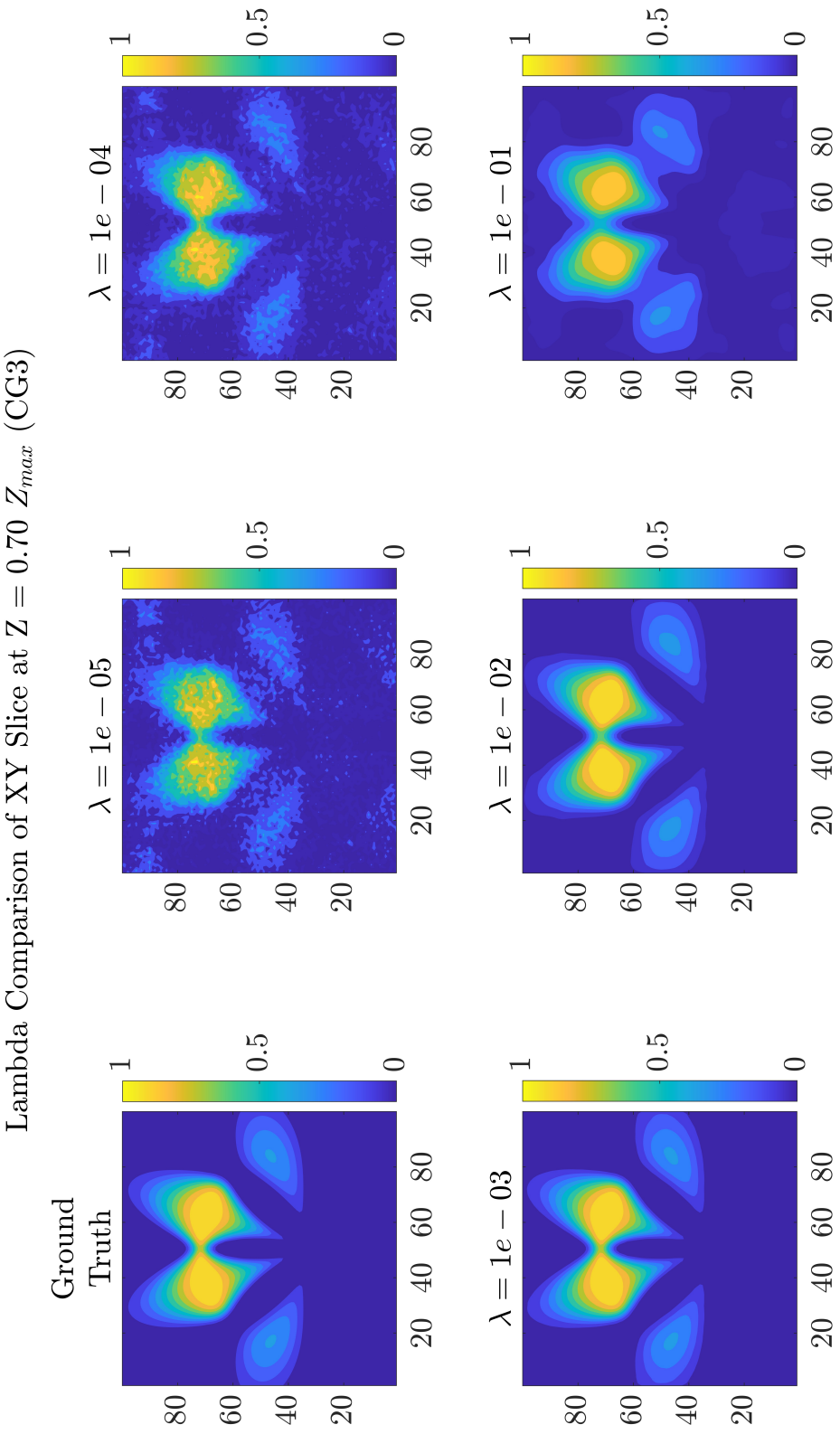

Figure A.7: XZ Slices of Regularized Reconstructions for CG3

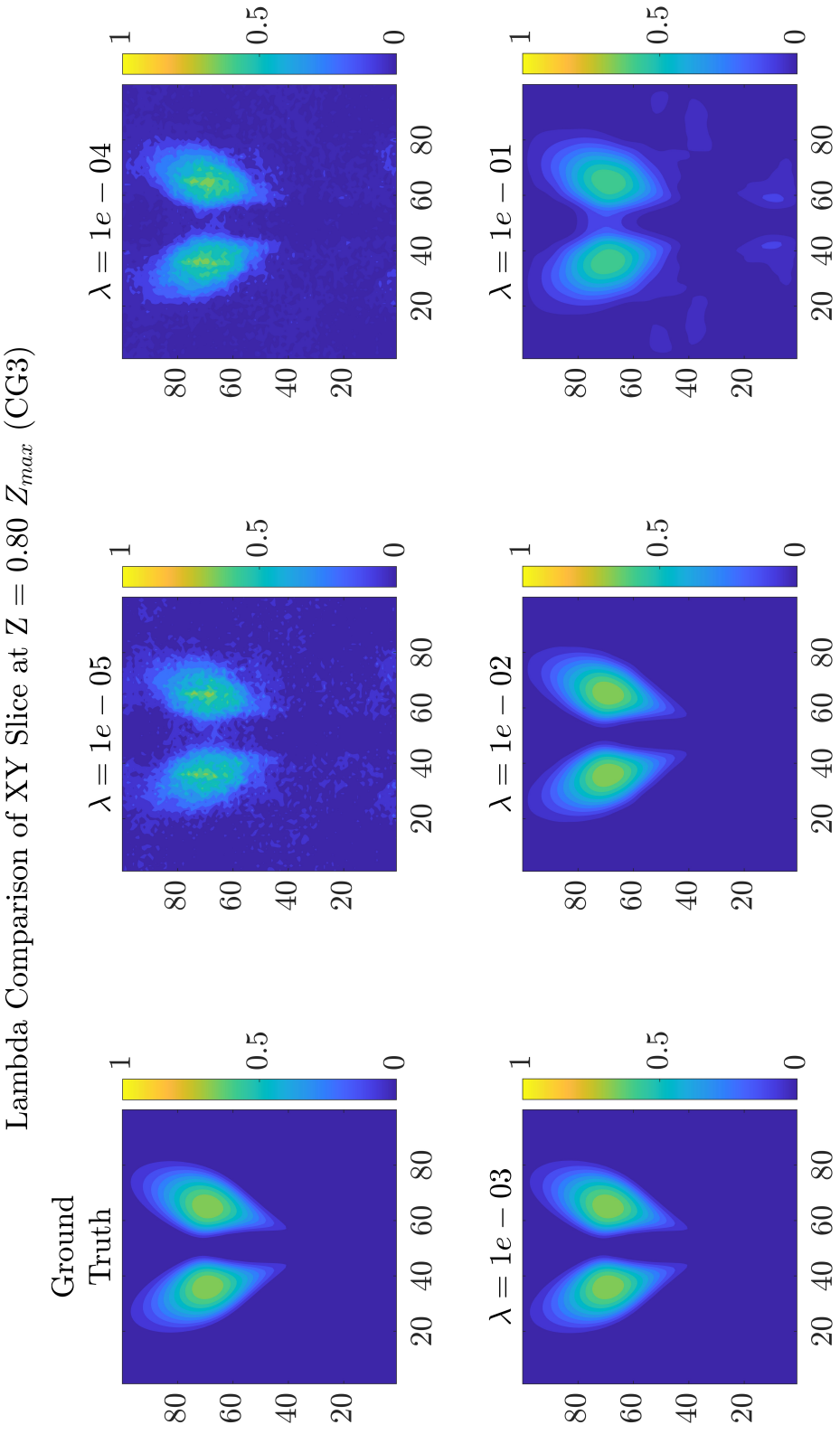

Figure A.8: XZ Slices of Regularized Reconstructions for CG3

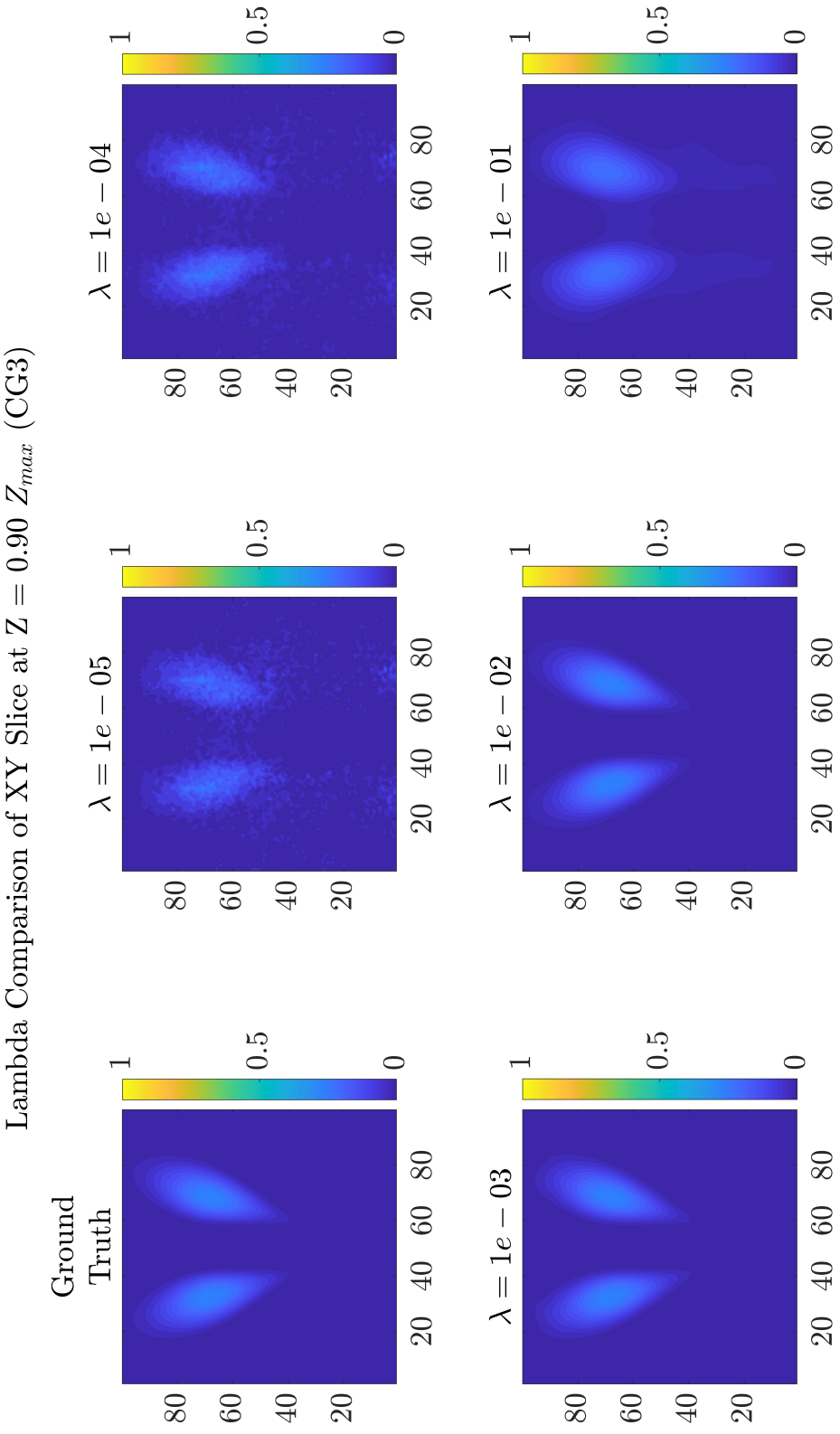

Figure A.9: XZ Slices of Regularized Reconstructions for CG3

APPENDIX B

ADDITIONAL DNS TURBULENT JET RESULTS AND IMAGES

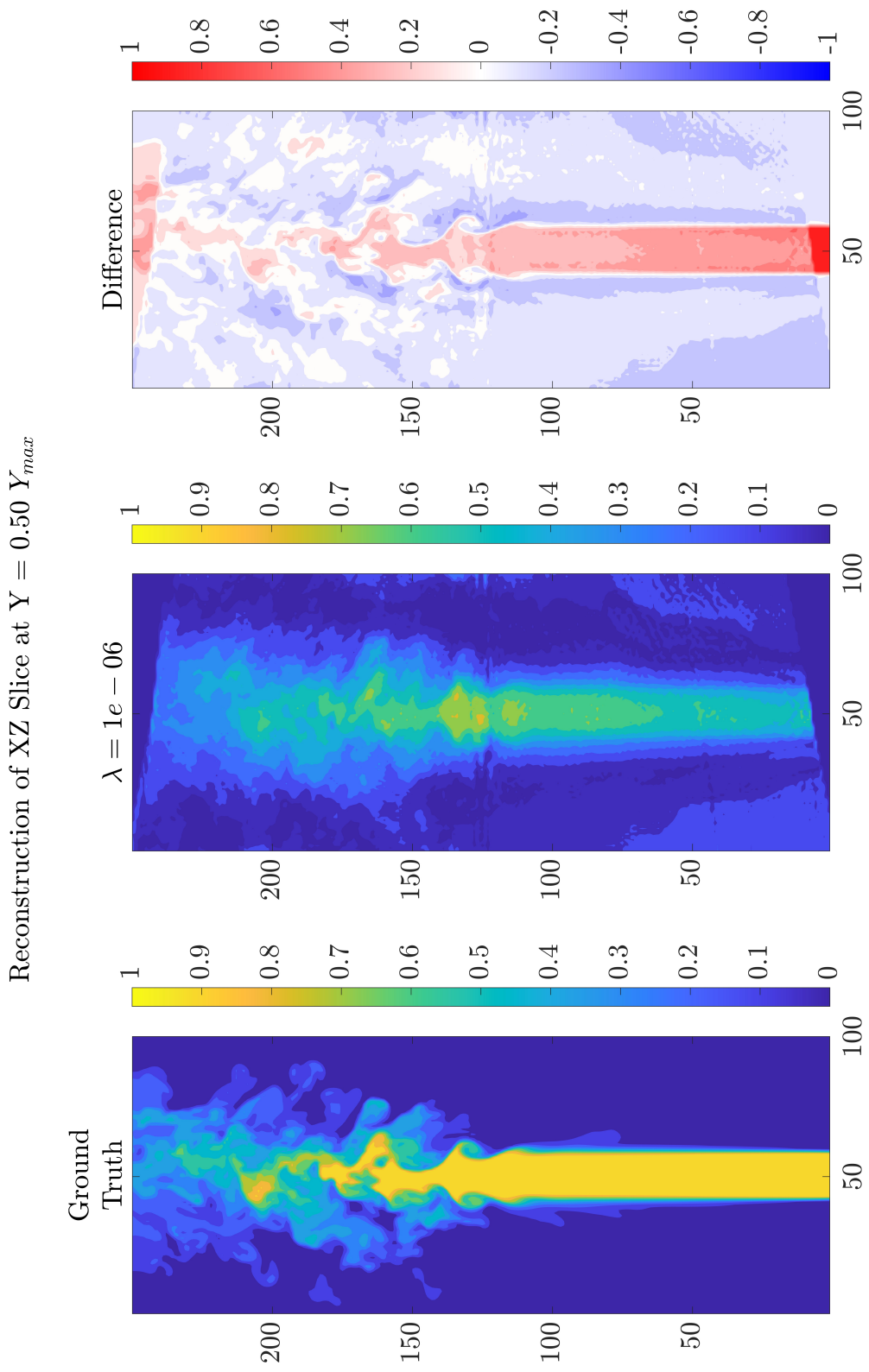

Figure B.1: XZ Slices of Regularized Reconstructions for Dataset 1

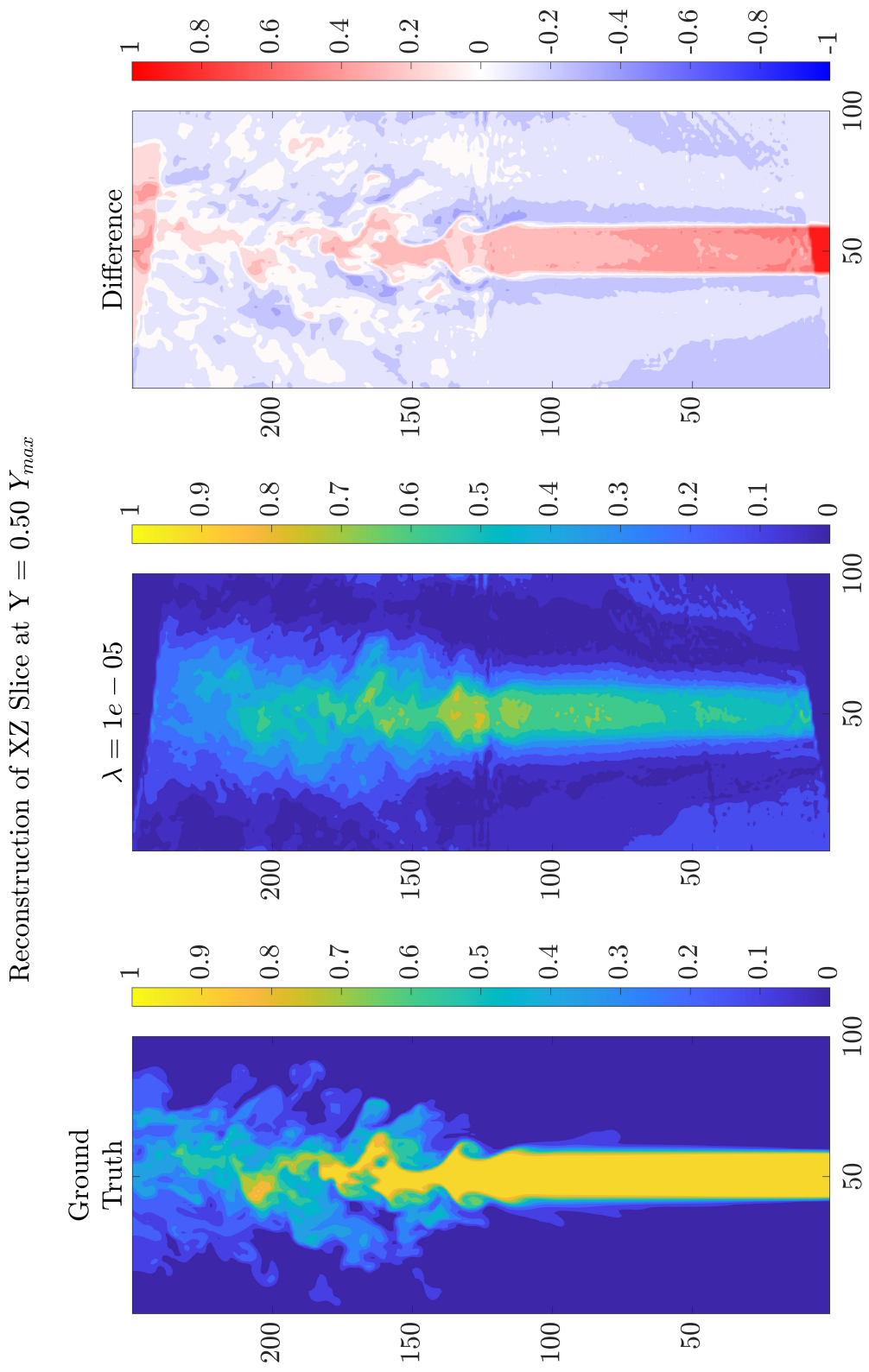

Figure B.2: XZ Slices of Regularized Reconstructions for Dataset 1

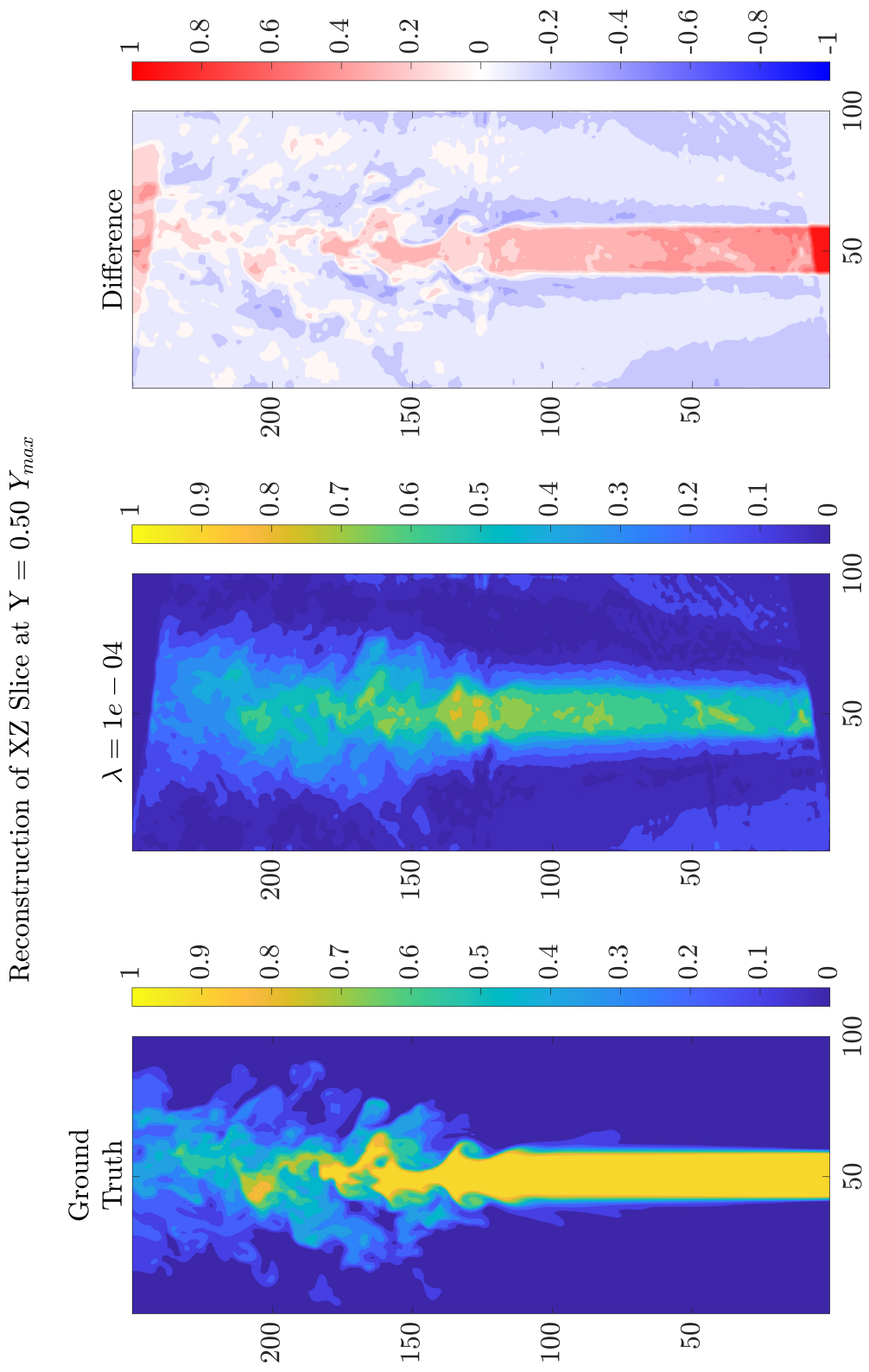

Figure B.3: XZ Slices of Regularized Reconstructions for Dataset 1

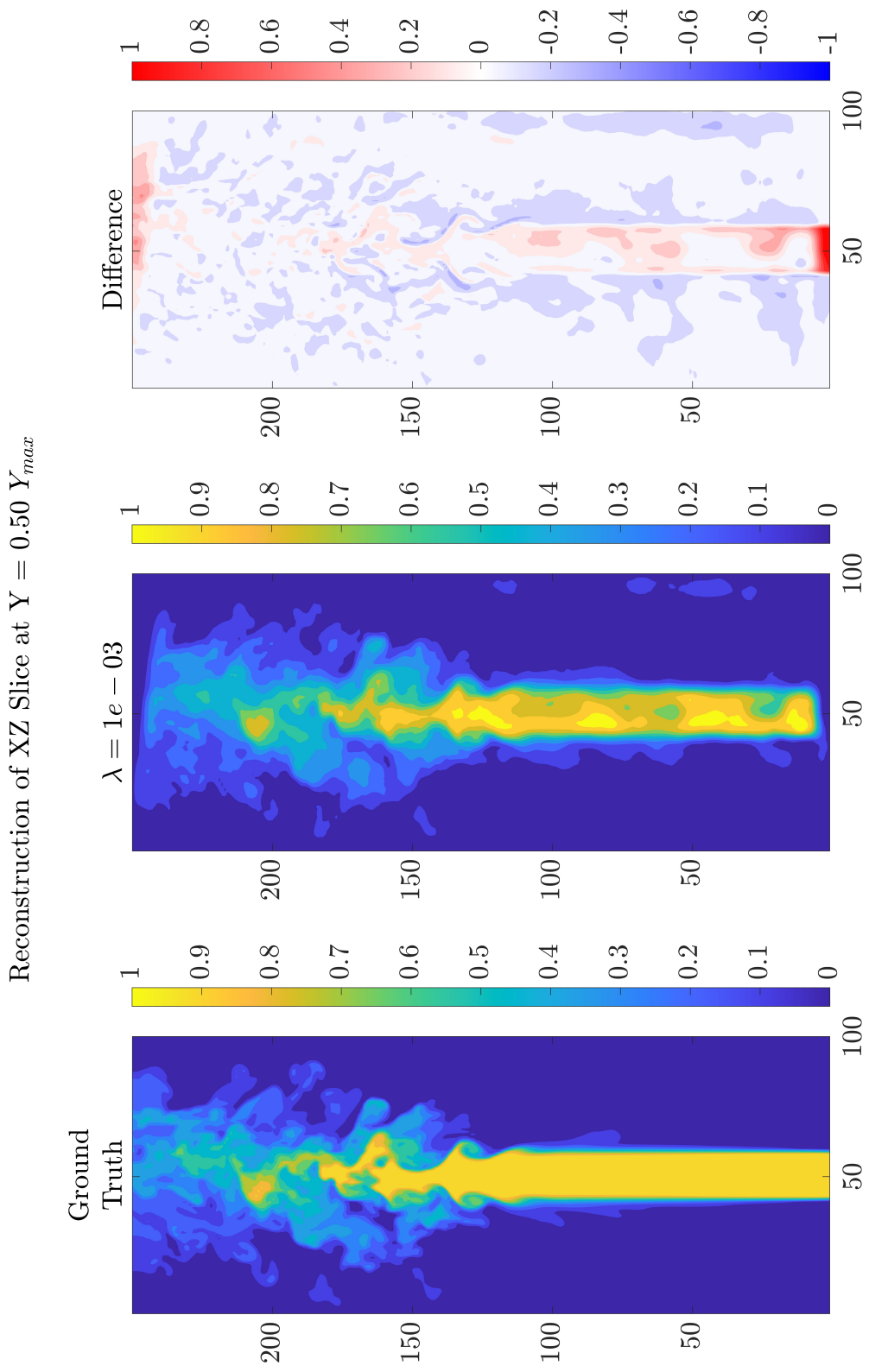

Figure B.4: XZ Slices of Regularized Reconstructions for Dataset 1

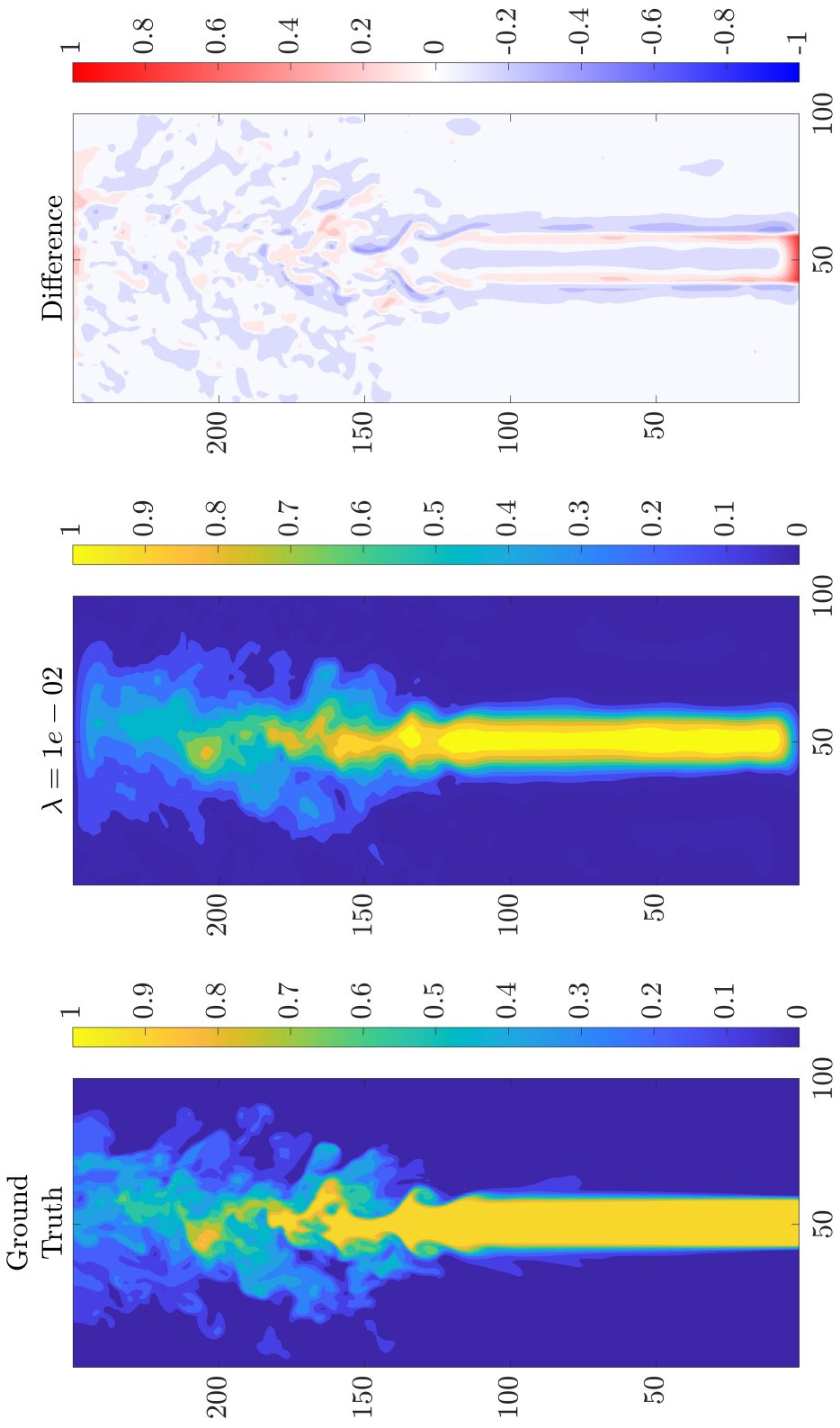

Figure B.5: XZ Slices of Regularized Reconstructions for Dataset 1

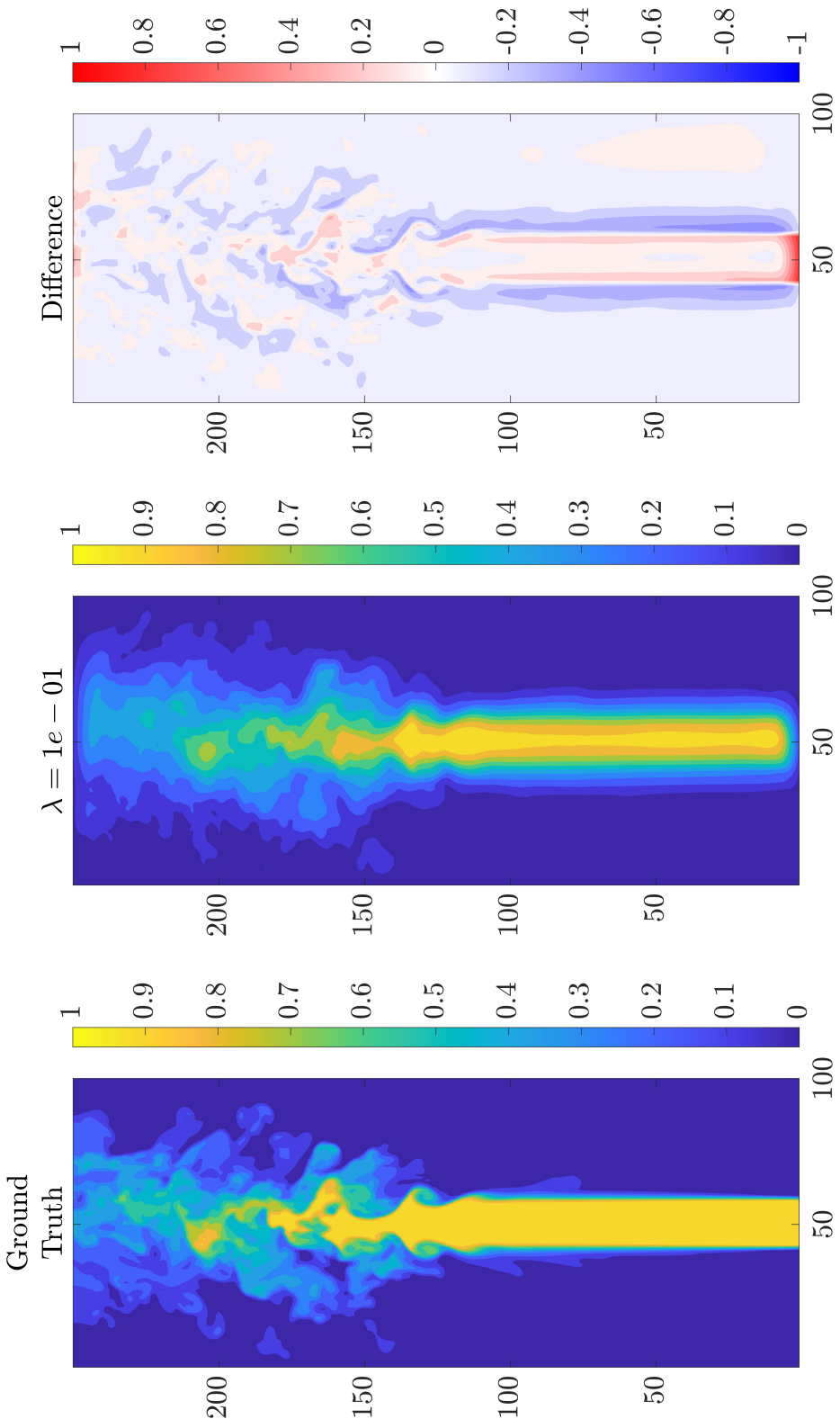

Figure B.6: XZ Slices of Regularized Reconstructions for Dataset 1

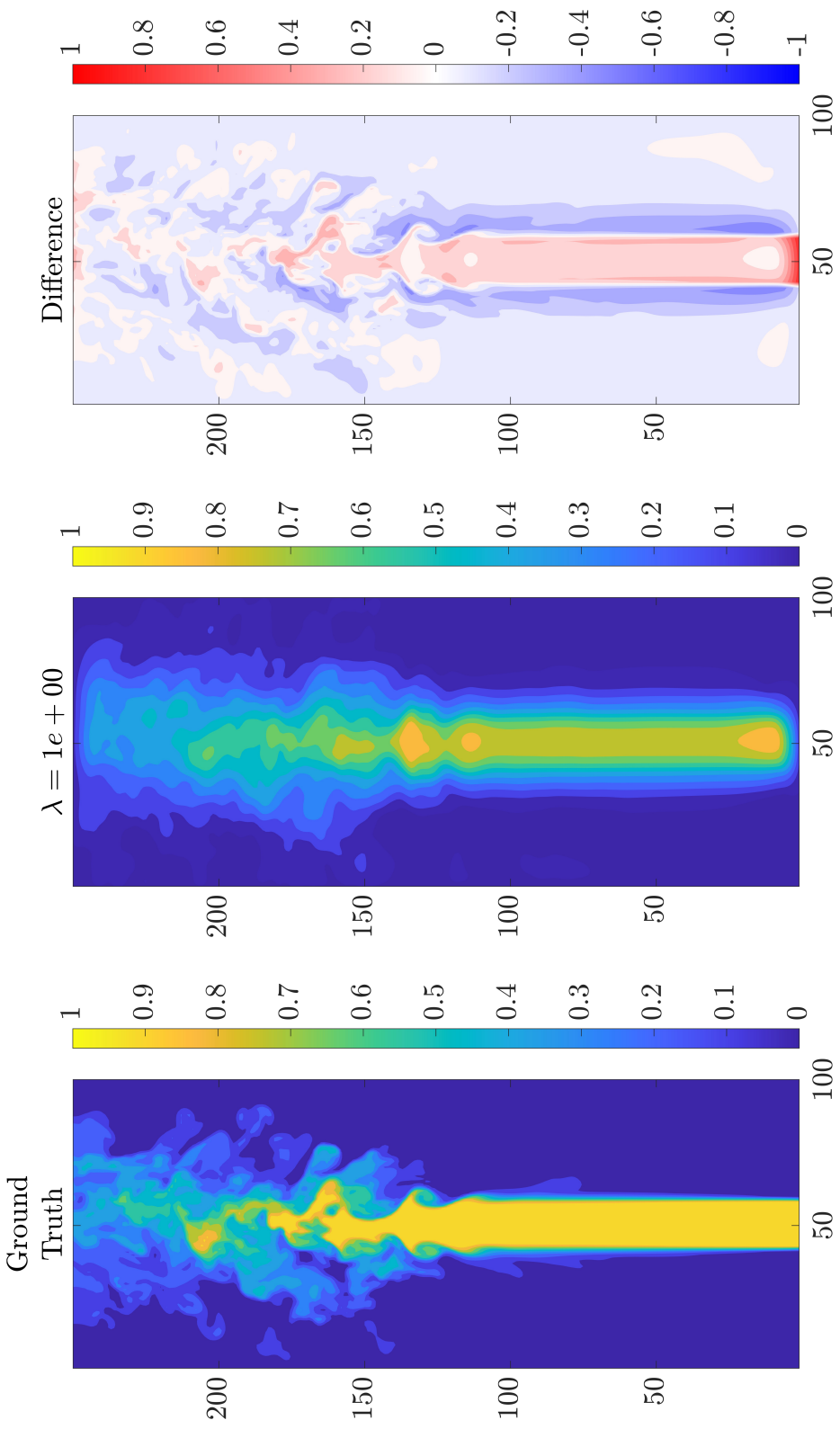

Figure B.7: XZ Slices of Regularized Reconstructions for Dataset 1

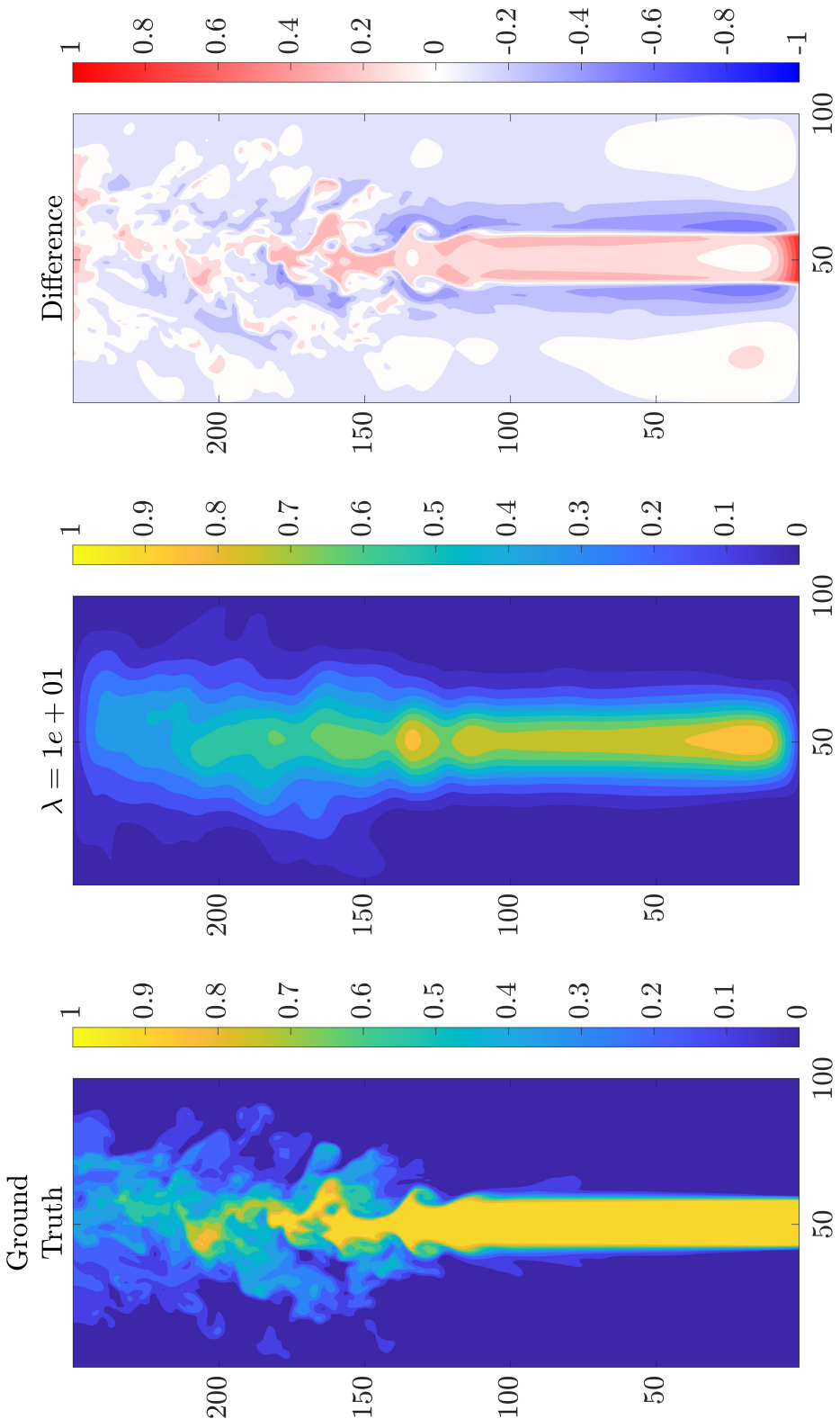

Figure B.8: XZ Slices of Regularized Reconstructions for Dataset 1

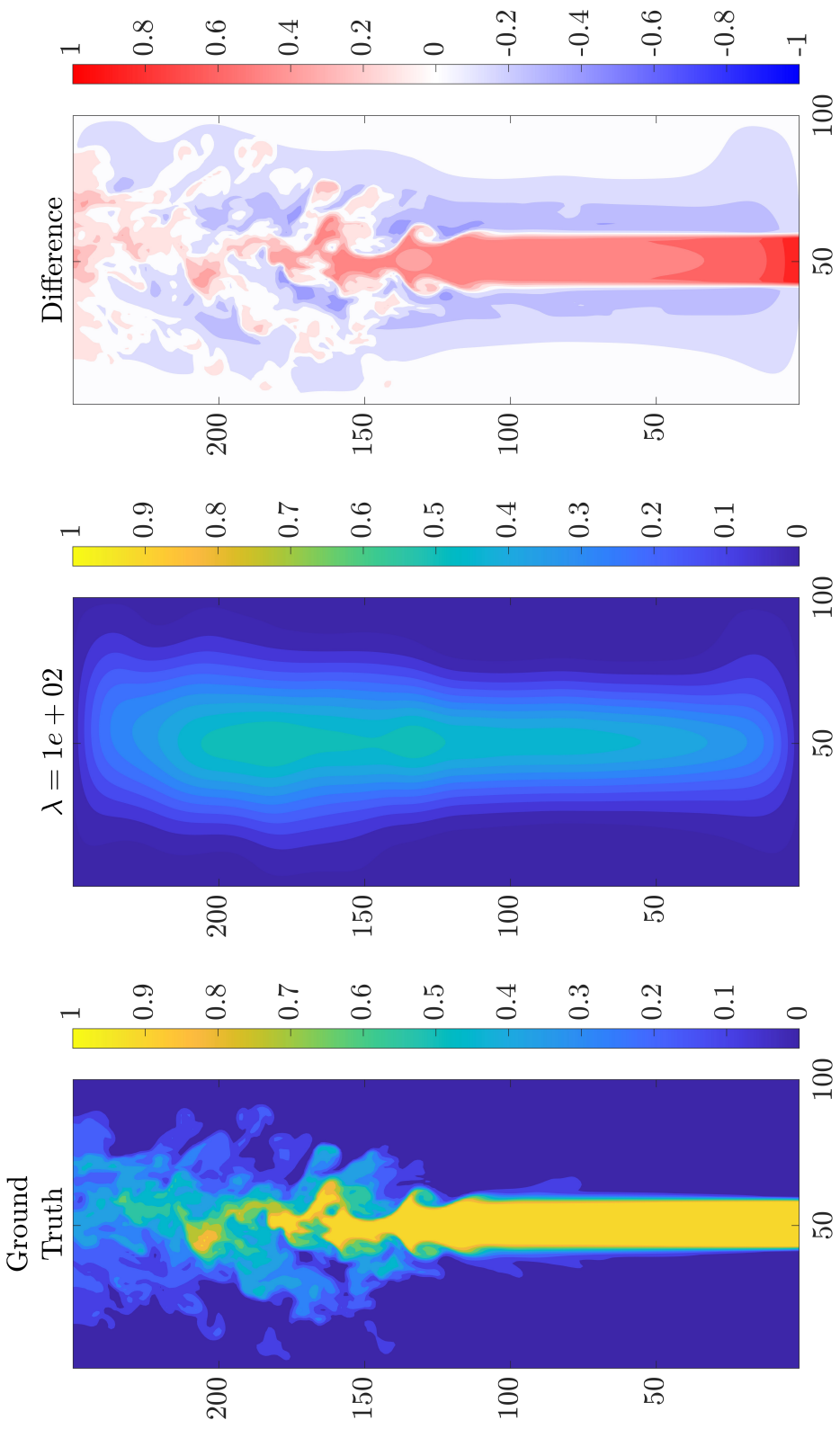

Figure B.9: XZ Slices of Regularized Reconstructions for Dataset 1